To the Graduate Council:

I am submitting herewith a dissertation written by David H. Plemmons entitled "Laser-Spark Ignition and the NH Radical." I have examined the final copy of this thesis for form and content and recommend that it be accepted in partial fulfillment of the requirements for the degree of Doctor of Philosophy, with a major in Physics.

Christian Parigger

Christian Parigger, Major Professor

We have read this thesis
and recommend its acceptance:

Dennis Keefer

Horace Crater

Lloyd M Davis

Accepted for the Council:

CW Minkel

Associate Vice Chancellor
and Dean of The Graduate School

Laser-Spark Ignition and the NH Radical

A Dissertation

Presented for the

Doctor of Philosophy

Degree

The University of Tennessee, Knoxville

David H. Plemmons

May 1996

Dedication

Dedicated to Sharon and Joshua.

Acknowledgements

I would like to thank Dr. Christian Parigger, who has been my mentor since I first arrived at the University, for his many hours of instruction, advice and assistance. I am also deeply grateful to Dr. J. W. L. Lewis who has been fundamental to my academic and experimental success. A special thanks is also due to the research staff in the Center for Laser Applications: Jim Few, Fred Schwartz, and Newton Wright. Their assistance and advice has saved me countless hours in the laboratory.

Abstract

Laser-induced breakdown is studied in ammonia and ammonia-oxygen gaseous mixtures. We investigate the emission spectra of the NH and N_2 diatomic molecules in pure ammonia optical plasmas using multispecies spontaneous emission spectroscopy. Gas temperatures are inferred in the decaying optical plasma by theoretical reproductions of the experimental spectra. Laser-induced breakdown microplasmas (laser sparks) are used to ignite combustible ammonia-oxygen gaseous mixtures. We determine the minimum ignition energy requirements and laminar flame speeds over much of the flammability limits of these gas mixtures. The experimentally determined flame speeds are compared to theoretical laminar flame speeds. High-speed shadowgraph photography and planar laser-induced fluorescence imaging of the NH free radical is used to study the temporal and spatial development of the optical plasma in combustible and noncombustible ammonia-oxygen mixtures.

Knowledge of the spatial and temporal evolution of gas temperature and species concentrations as well as spatial symmetries in the laser-induced breakdown plasma is essential for numerical modeling of laser-spark ignition. Experimentally determined quantities such as temperature, free-radical relative number densities, minimum ignition energies, and flame speeds can be used to validate such models.

In all laser-induced breakdown studies, the optical discharge was created by focusing Q-switched Nd:YAG laser 1.064 micrometer wavelength pulses into the gas sample. Focused laser-pulse intensities range from 10's to 100's of GW/cm^2.

Contents

List of Figures

Chapter 1

Introduction

The primary objectives of this research are to investigate 1.064 μm pulsed-laser-induced plasmas in pure ammonia gas and ammonia-oxygen gaseous mixtures and to investigate 1.064 μm pulsed-laser-spark ignition of combustible ammonia-oxygen gaseous mixtures. The focus of the research is directed toward four major areas: local gas temperatures, optical breakdown thresholds, minimum ignition energies, and the spatial and temporal development of laser sparks and ignition kernels.

The goals of the experimental investigations are to characterize the Nd:YAG laser requirements for initiation of laser-induced breakdown and laser-spark ignition of ammonia-oxygen flammable mixtures, to establish a data base for comparison with other modes of ignition, and to investigate shockwave effects on the ignition process. It is important to measure these parameters in a relatively simple system to establish a method of model verification. When developed, such a model could then be extended to more complex ignition/combustion phenomena that occur in liquid-vapor-oxidizer combustion systems, for example, in a gas-turbine engine.

Laser-induced breakdown (or optical breakdown) in a gas is initiated when a laser beam (or pulse) is focused to sufficient intensity to ionize molecules in the focal volume of the lens. For nonresonant breakdown, the initial ionization occurs through high-order multiphoton absorption. Optical breakdown in atmospheric pressure gases using infrared laser pulses ($\lambda > 1\mu$ m) is dominated by cascade ionization [1]. That is, once the initial electrons are stripped from the molecules, they are accelerated by inverse bremsstrahlung in the presence of the strong optical field. These accelerated electrons collide with other gas molecules causing further ionization. This cascading process continues in the presence of the laser pulse, resulting a hot dense plasma in the region around the focal volume of the lens.

For a high intensity laser pulse, a strong shockwave is produced by the optical breakdown. This expanding shockwave heats the gas surrounding the breakdown region and rapidly decays to an acoustic wave. For a tightly focused laser pulse, the initial stages of the shockwave propagation can be approximated as a point-source explosion or Taylor blastwave [2].

As the optical breakdown plasma (or laser spark) expands and cools, it heats the adjacent gas and induces chemical reactions. If the laser spark occurs in a noncombustible gas, the heated region will relax to the ambient temperature, although the chemical constituents of the gas may be altered by the laser spark. In a combustible gas, the laser spark evolves into an ignition kernel. Whether the ignition kernel develops into a propagating flame depends on the size of the kernel and on the temperature gradient across the kernel. Consider a spherical ignition kernel where the temperature in the center of the kernel has relaxed to the order of a normal flame. If the kernel diameter has grown to a size such that the temperature gradient between the burned gas in the center of the kernel and the unburned gas on the periphery of the kernel has approximately the same slope as the temperature gradient in a steady-state combustion wave, then a propagating flame will be established. If the kernel diameter is to small, the heat loss from the kernel to the ambient gas will exceed the heat gain from the exothermic chemical reactions and the combustion wave will become extinct after only a small amount of gas around the original spark is burned.

The complexity of the optical plasma formation and subsequent relaxation into a flame kernel means that a computationally realizable model of laser-spark ignition will have to include numerous approximations. Knowledge of local gas temperatures as a function of space and time will be essential for model verification. Comparison of theoretical predictions to experimentally determined temporal and spatial temperatures would be a good method of checking the models accountability of real gas and radiation transport effects. It may also be possible to formulate an approximate model based on experimentally determined temperatures, species number densities, and spatial dimensions of the ignition kernel – thereby bypassing the difficulties of modeling laser-induced breakdown and blastwave dynamics.

This dissertation focuses on the experimental study of laser-spark ignition in ammonia-oxygen mixtures using a Q-switched Nd:YAG laser ($\lambda = 1.064$ μm). Therefore, the pulsed laser interaction with the gaseous medium needs to be characterized. Since laser-spark ignition cannot be achieved without optical breakdown, knowledge of the breakdown threshold is required for these gases at the given laser wavelength, laser pulse width, and focal conditions.

Once optical breakdown is achieved, the energy deposited into the laser spark is the primary factor in establishing a combustion wave. Therefore, minimum ignition energy is a very good parameter to compare to theoretical predictions. It is also a convenient parameter for comparison with other ignition modes (i.e., electrical sparks).

Shadowgraph and laser-induced fluorescence imaging of the NH free radical is used to visualize shockwave effects outside of the spatial region where spontaneous emission is observed. Ignition delay times are investigated using these data. The acquired images are used to investigate spatial symmetries in the kernel development. It is know from previous shadowgraph studies [3] with other gases that the laser spark induces turbulence in the ignition kernel. LIF imaging is used to probe this effect as well. Shadowgraph imaging is also used to measure flame propagation speeds as a function of the fuel/air ratio. Spatial dependencies and laser-induced symmetry effects on the flame propagation are investigated. Comparison of the experimental results are made with theory using the CHEMKIN laminar flame computer code [4].

Chapter 2 summarizes the initial efforts of characterizing the laser spark in pure ammonia. The spontaneous emission spectra that is produced in a laser spark is investigated and a method of inferring temperature from theoretical fits to experimental spectra of the $A^3\Pi_i$ - $X^3\Sigma^-$ system of NH and the $C^3\Pi_u$ - $B^3\Pi_g$ second positive system of N_2 is presented. Thermodynamic equilibrium within the plasma is also discussed and nonequilibrium experimental and theoretical spectra are presented. In Chapter 3, the minimum energy thresholds for nonresonant laser-spark ignition of atmospheric pressure ammonia-oxygen (NH_3-O_2) gaseous mixtures are studied as a function of the fuel-air ratio; and the optical breakdown thresholds in pure ammonia, pure oxygen, and room air are determined. A method of calculating the focused intensity of a measured laser beam spatial profile is presented. Flame speeds in various ammonia-oxygen laser-spark ignited mixtures are measured in Chapter 4. The results are presented as laminar flame speeds and the experimental values are compared to theoretical laminar flame speeds. In Chapter 5, spatially and temporally resolved images of the laser spark are presented. Shadowgraph and planar laser-induced fluorescence images are used to track the optical plasma as it either relaxes in pure ammonia gas or evolves into an ignition kernel and subsequently into a propagating flame in combustible ammonia-oxygen mixtures. These images are also used to study ignition delay times and to study shockwave and gas dynamic effects on the ignition kernel and the propagating flame front.

Chapter 2

Analysis of Combined Spectra of NH and N_2

2.1 Overview

Laser-induced breakdown plasmas characteristically have rich emission spectra. Diatomic spectra, which result from atomic recombination and thermal excitation in the optical plasma, are often observed as a superposition of multiple species. These spectra can be used to probe the optical plasma. Common diagnostic goals are the determination of the degree of thermodynamic and chemical equilibrium, the determination of temperature, and the determination of the population densities of the observed species. This chapter is concerned with the use of spectroscopic methods to infer temperatures and possibly population densities from the combined spectra of well known systems of NH and N_2: the $A^3\Pi_i$ - $X^3\Sigma^-$ system of NH and the $C^3\Pi_u$ - $B^3\Pi_g$ second positive system of N_2.

The basic tools used here are tables of electric dipole line strengths and a computer code that uses the line strengths to compute an emission spectrum for the given temperature of an assumed Boltzmann distribution of states and a given line width of an assumed Gaussian line shape [5, 6]. A second code augments the emission spectrum routine with the Nelder-Mead algorithm [7], thereby permitting one to find the rotational temperature, vibrational temperature, and relative excited state population densities that give best agreement, in a least squares sense, between experimental and synthetic spectra [8, 9, 10].

The Einstein coefficients, oscillator strengths, etc., can each be defined in terms of the line strength, as shown, for example, in Thorne's table [11]. Thus, the line strength is a very convenient quantity for the computation of synthetic spectra. Figures 2.1 and 2.2(a) are examples of synthetic spectra one can easily compute using a line strength file. Figure 2.1 is a low resolution synthetic spectrum, which shows the content of our line strength file for the N_2 second positive system. Figure 2.2(a) gives a much higher resolution synthetic spectrum, computed using the same program and line strength file used to compute the spectrum of Fig. 2.1, and should be compared with the experimental spectrum of Roux *et al.* [12] reproduced in Fig. 2.2(b).

In this chapter, the results of several experiments that use the technique of a multispecies theoretical reproduction of combined NH-N_2 experimental spectra are presented. The primary objective is to infer the vibrational-rotational temperature of diatomic molecules under various experimental conditions. First, results obtained from pulsed laser-induced breakdown (LIB) in ammonia gas are discussed. A plasma emission spectrum is used to determine which band systems to include in the multispecies model. Second, the multispecies fitting technique is applied to experiments in which variations in the spontaneous emission signal levels and vibrational-rotational temperatures are investigated as a function of laser pulse energy. Third, temperature

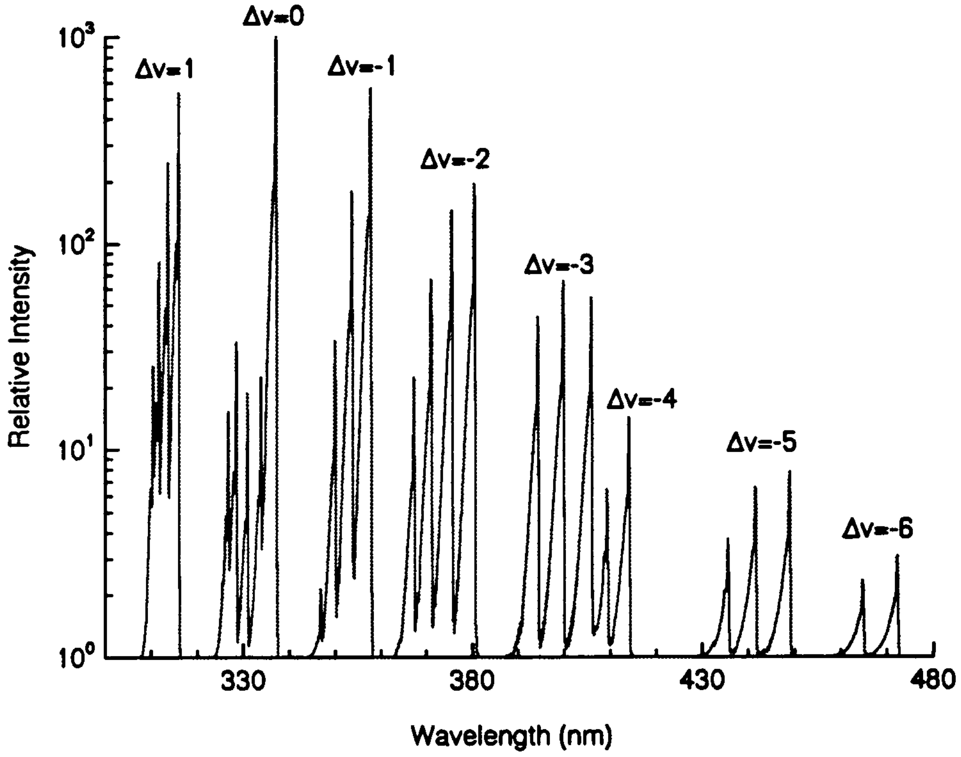

Figure 2.1: A Low resolution theoretical spectrum which shows the content of our N_2 second positive system line strength file. The calculation was done for a rotational temperature of 450 K and a vibrational temperature of 4500 K in order to enhance the vibrational band structure. The Gaussian line width of this spectrum is 10 cm^{-1} FWHM.

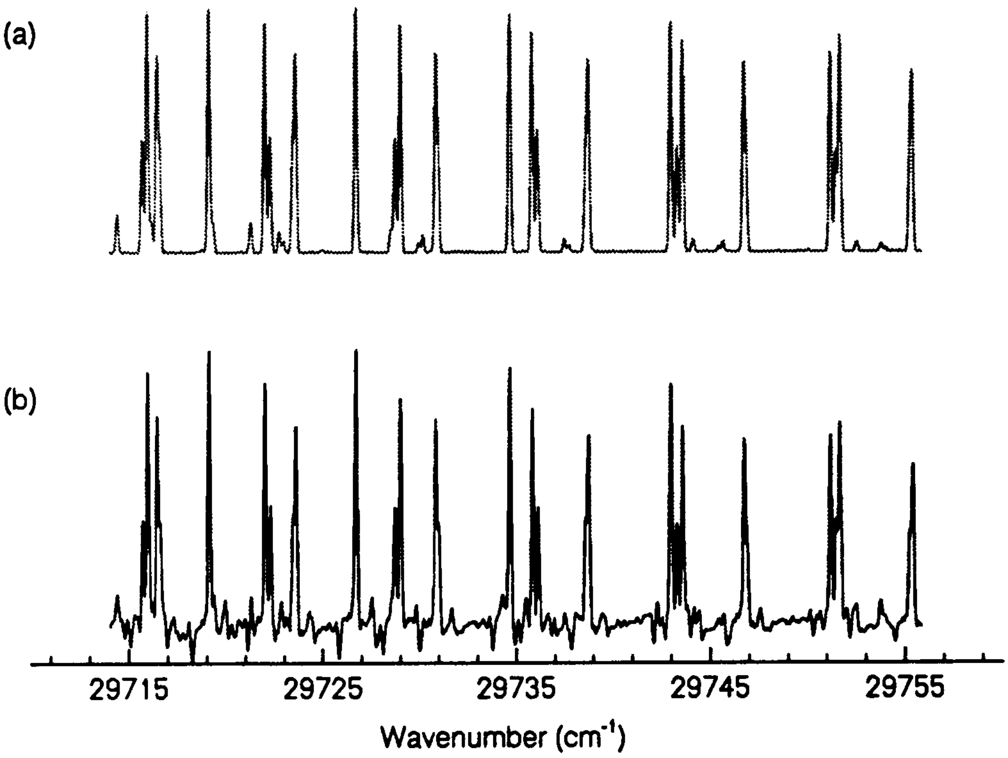

Figure 2.2: (a) High resolution (0.1 cm^{-1} FWHM) theoretical spectrum of a portion of the N_2 second positive system with $T_r = T_v = 450$ K. (b) Experimental spectrum of Roux *et al.* The alternation of intensities produced by nuclear spin statistics can be observed for a Λ-doubled spectrum only when the Λ-doublets are resolved. A factor of 2 intensity alternation (i.e., a nuclear spin of 1) is seen in both Roux's experimental spectrum and the synthetic spectrum.

measurements, in which the spatial temperature variation across the focal volume of the breakdown laser pulse is resolved, are reported. Finally, the results of a multispecies fit to an experimental spectrum in which the vibrational and rotational temperatures are clearly not in equilibrium are presented. First, a brief description of the line strength files used to calculate the theoretical spectra is provided.

2.2 The Line Strength Files

The line strengths are obtained by fitting a model Hamiltonian to reported experimental line positions. This gives the set of molecular parameters, appropriate to the model Hamiltonians for the upper and lower states, that is used to compute the line strengths. The many differences, large and small, between various model Hamiltonians that have been reported in the literature make the use of reported molecular parameters very difficult. For example, Rensberger *et al.* [13] reported large differences, on the order of 1 to 2 Å, between their calculated NH line positions and experimentally measured line positions, even though the molecular parameters and experimental line positions came from the same paper by Brazier *et al.* [14]. Our method produces molecular parameters which are in poor agreement with those reported by Brazier *et al.* but reproduces their reported NH experimental line positions with a standard deviation of 0.003 cm^{-1}. The line positions in our fits to the N_2 second positive system data of Roux *et al.* [12, 15] typically had a standard deviation of 0.001 to 0.01 cm^{-1}.

2.3 Laser-Induced Breakdown Spectra

2.3.1 Experiment

A pulsed Nd:YAG (Continuum YG680S) laser was used to generate optical breakdown in research grade anhydrous ammonia. The Nd:YAG laser is Q-switched and emits 1.064 μm pulses with a pulse width of 6 ns full width at half maximum (FWHM). This laser operates in many longitudinal modes, which gives mode beating and hence temporal substructure to the 6 ns pulse. The output pulses were beam expanded, using a 4× antireflection coated beam expander. The expanded pulses were focused, using a antireflection coated, plano-convex, 10 cm focal length lens, into a vacuum cell which contained the ammonia gas at 100 torr. The beam diameter of the expanded laser pulses was approximately 2 cm, resulting in a f/# of approximately 5. The gas cell is equipped with 1.5 inch, uncoated, fused silica windows on four sides and the cell was positioned so that these windows were in the horizontal plane. The plasma emission was imaged, perpendicular to the laser pulse propagation, with one-to-one magnification, onto an 800 μm diameter fiber-optic cable, which was optically coupled to a spectrometer. The spectrometer used to disperse the spectrum was a Jobin-Yvon crossed Czerny-Turner 0.64 meter spectrometer equipped with a 1200 g/mm grating. The spectrum was recorded with an intensified, gated CCD detector (EG&G PARC OMA4, Model 1530-CUV) equipped with a lens-coupled intensifier. Wavelength calibration was accomplished by comparing the experimental spectrum to a theoretical spectrum.

The experimental spectra were recorded 0.5 μs after the laser pulse and consist of an average of 1000 events. The average energy per pulse was 60 mJ.

2.3.2 Description of Combined NH and N_2 Spectra

Figure 2.3 shows an experimental NH $A^3\Pi_i$ - $X^3\Sigma^-$ spectrum and poorly fitted synthetic spectrum obtained by using only the NH line strength file and assumed vibrational-rotational equilibrium. The largest disparities between experiment and theory are in the region of the strongest bands of the $\Delta v = 0$ sequence of the N_2 $C^3\Pi_u$ - $B^3\Pi_g$ second positive system. An appropriately scaled N_2 second positive theoretical spectrum is also shown in Fig. 2.3. The theoretical NH spectrum shown in Fig. 2.3 was fitted only to the spectral region outside the influence of the N_2 second positive system ($\lambda \geq 338$ nm). The shorter wavelength portion of the NH spectrum was calculated from the resulting best fit temperature (4670 K). The N_2 spectrum was calculated for a temperature of 5000 K.

Attempts to fit the entire experimental spectrum with only NH resulted in significant increases in temperature ($\Delta T \simeq 700$ K). In fitting the spectrum, the program attempts to duplicate the intensity ratio between the strong 0-0 and 1-1 Q-branches and at the same time reproduce the R- and P-branch rotational structure. The superposition of the N_2 0-0 band and the NH 1-1 band at 337 nm is the primary cause of the increase in fitted temperature. A typical fit is shown in Fig. 2.4. The largest disparities are in the region of the N_2 system and the NH 2-2 vibrational band.

To decrease the disparities between theory and experiment, the fitting of the synthetic spectrum was repeated using line strengths for both NH and N_2. In the fitting procedure, the rotational and vibrational temperatures were again assumed to

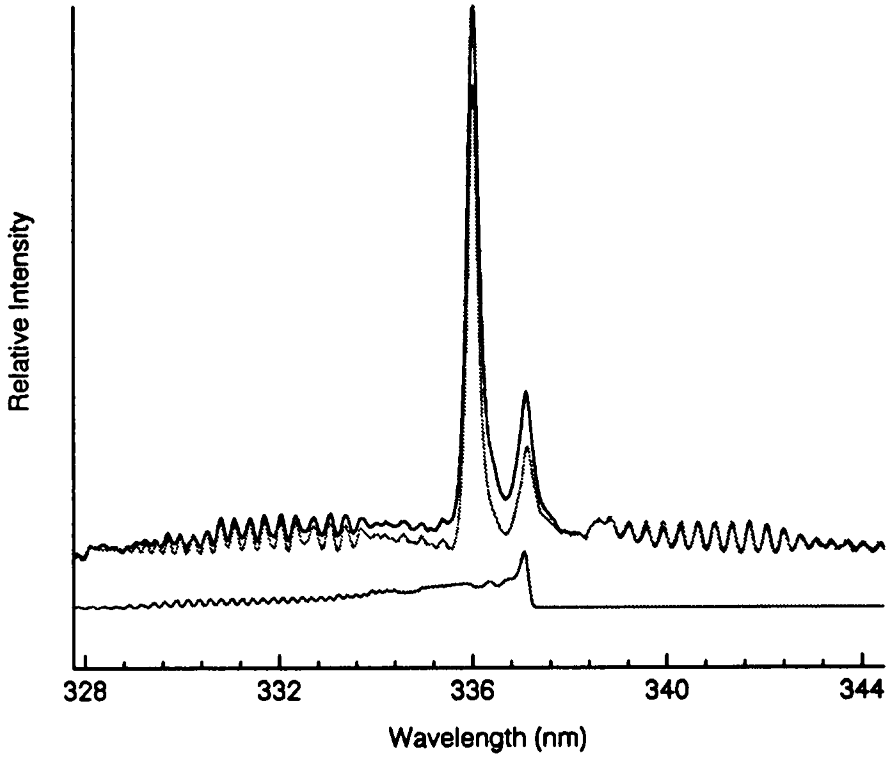

Figure 2.3: Experimental spectrum and a theoretical spectrum calculated from the parameters resulting from a spectral fit to $\lambda \geq 338$ nm. The theoretical spectrum underpredicts the experiment in the region of the N_2 second positive system. The expected N_2 contribution is shown along the bottom of the figure. The Gaussian line width of the theoretical spectrum is 15.5 cm^{-1}.

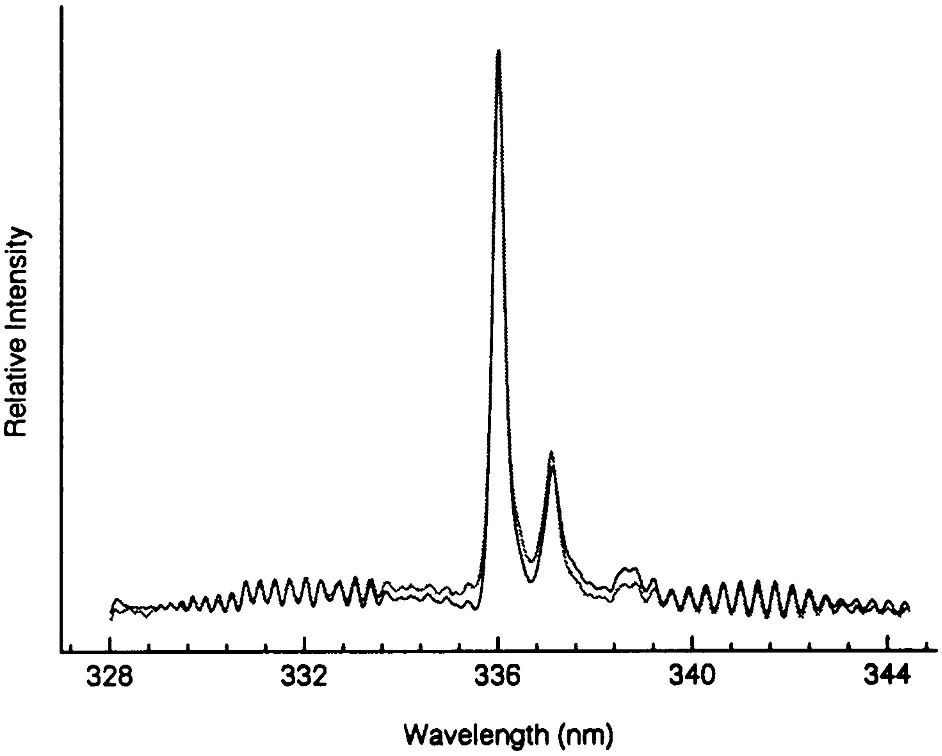

Figure 2.4: Fitting only NH to the experimental spectrum causes the theory to underpredict the intensity in the middle of the spectrum, which contains the N_2 contribution, and overpredict the intensity in the spectral region, which contains no N_2 contribution. The Gaussian line width of the theoretical spectrum is 15.5 cm^{-1}.

be the same. This common temperature and the intensity contribution of each species were allowed to vary until the sum of the squared residuals between the experimental and synthetic spectra was minimized. The addition of N_2 into the model gives the fit shown in Fig. 2.5, in which the standard deviation in the sum of the squared residuals is reduced by a factor of 2 compared to that of Fig. 2.4. The best fit temperature of 4950 K is 280 K (or 6%) larger than the rotational fit of Fig. 2.3. In a previous paper [9], a confidence interval of ±5% for the fitted temperature was inferred from parameter studies. The results above are consistent with this evaluation.

The NH-N_2 spectrum is consistent with the assumption of thermal equilibrium between the rotational and vibrational states. We have previously reported temperatures inferred from CN violet [8] and C_2 Swan [9] spectra emitted from laser produced plasmas in which equilibrium between the rotational and vibrational states was also observed.

Further analysis on the degree of equilibrium that exists in the optical plasma can be accomplished through the relative emission intensities of the NH-N_2 spectra. The following analysis shows that the observed spectra are either not in chemical or not in thermodynamic equilibrium, or both.

The emission intensities calculated from the line strength files are in the form of absolute intensity per excited state molecule. The total intensity for two excited state molecules is

$$I_{total} = I_1 + RI_2,$$

where R is a scaling factor for relative intensities between two molecular species and

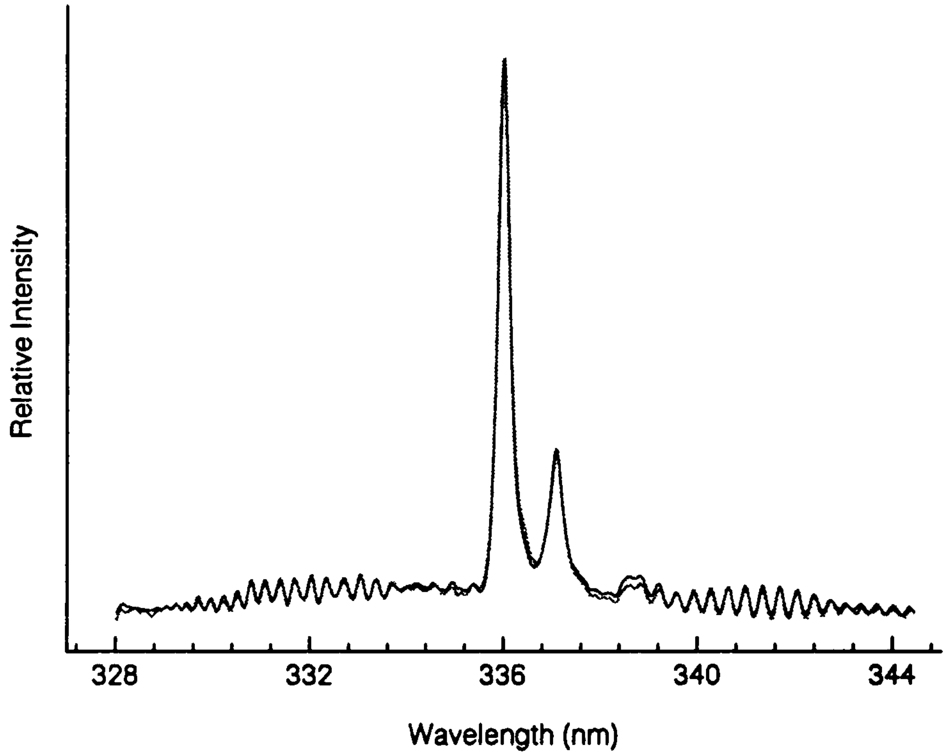

Figure 2.5: Experimental spectrum and a theoretical NH-N_2 fit. The theory slightly over predicts the intensity in the region of the NH 2-2 band ($\lambda \simeq 339.3$ nm). The Gaussian line width of the theoretical spectrum is 15.5 cm^{-1}.

can be equated to the relative excited state number density. If the molecules are in thermodynamic equilibrium, then the excited state number density ratio can be related to the ground state number density ratio by the relation

$$\frac{N_2^0}{N_1^0} = R\frac{Q_2}{Q_1},$$

where N_i^0 is the ground state number density of species i and Q_i is its partition function.

The ratio of partition functions Q_{N_2}/Q_{NH} at 5000 K is approximately 1.8. For the fitted spectrum in Fig. 2.5, $R = 1.6 \times 10^5$. This implies that $N_{N_2}^0/N_{NH}^0 \simeq 3 \times 10^5$.

The Gordon-McBride chemical equilibrium code [16] at 100 torr and 5000 K predicts that $N_{N_2}^0/N_{NH}^0 \simeq 2 \times 10^3$. Electronic partition functions tell us that at 5000 K the ground electronic state of N_2 will be practically 100% occupied while that of NH will be 98% occupied. These results imply that (a) the molecules are not in chemical equilibrium and/or (b) the assumption of thermodynamic equilibrium cannot be justified.

Spectra recorded at earlier times in the plasma contain lines of atomic hydrogen, atomic nitrogen, and its ions. The NH-N_2 spectra observed in the plasma decay are the result of recombination fluorescence, and therefore, chemical and thermodynamic equilibrium should not necessarily be expected at early time delays in the plasma decay. However, for long enough time delays after the laser-induced plasma initiation (on the order of 10's of microseconds depending on the laser pulse energy), diatomic spectra have been observed in thermodynamic and chemical equilibrium [17, 18]. Thus, one can only infer from the NH-N_2 spectra that the intensity contribution of each excited state molecule inferred from the best fit above is the population density ratio of excited state molecules that radiatively decay to the lower electronic state.

2.4 Laser Pulse Energy Variation Study

2.4.1 Experiment

In this experiment, the laser pulse energies were varied to investigate the effects of absorbed energy on the NH-N_2 signal level and the vibrational-rotational temperature. Pulse energies were varied from sub-threshold values, in which breakdown did not occur and a signal was not observed, up to 60 mJ.

The experimental setup was the same as that in the previous section with the following additions. In order to achieve the desired degree of energy attenuation without changing the temporal or spatial characteristics of the laser pulses, optical flats were placed in the beam path. The optical flats were inserted as matched pairs to prevent beam walk. An energy meter (Scientech, Model P50, calibrated for 1.06 μm) was placed after the vacuum cell to monitor the average pulse energy of the optical breakdown pulses.

Spectra were recorded with a detector gate-width of 1 μs and time delays of 0.5 μs and 1 μs. Emission signals were averaged over 1000 laser shots for each pulse energy studied.

2.4.2 Results

Temperatures were inferred from spectral fits to the combined NH-N_2 profiles as discussed in Section 2.3. The experimental and theoretical profiles are essentially the same as those shown in Fig. 2.5. NH-N_2 signal levels were determined from the difference in intensities at 336.01 nm (the peak of the 0-0 band) and 327.82 nm (which served as the background).

Average incident energies for each data point were determined by evacuating the vacuum cell, so that optical breakdown would not occur. Reflective losses of the rear window of the cell were measured and corrected for in all energy measurements. During the acquisition of the spectra, average transmitted energies were measured so that the average energy per pulse absorbed by the optical breakdown plasma could be determined.

Figure 2.6 shows the resulting temperature as a function of the absorbed energy. The temperature appears to very quickly approach an asymptotic value relative to the considered abscissa values. It is likely that a saturation occurs in the optical plasma. Yalçin *et al.* [19] found that as more energy is added to the optical breakdown pulse both the electron number density and temperature quickly saturate. That is, as the pulse energy is increased above some critical value the plasma becomes larger – rather than hotter and more dense.

Figure 2.7 shows the NH-N_2 emission signal level (detector counts) of the combined spectra as a function of the absorbed energy. The signal level was measured at the peak of the NH 0-0 band (336 nm). The emission signal shown in Fig. 2.7 also appear to approach an asymptotic value as the absorbed energy increases. This behavior implies that there is a maximum number density of NH molecules which are created by the optical breakdown. This behavior is consistent with the saturation discussed

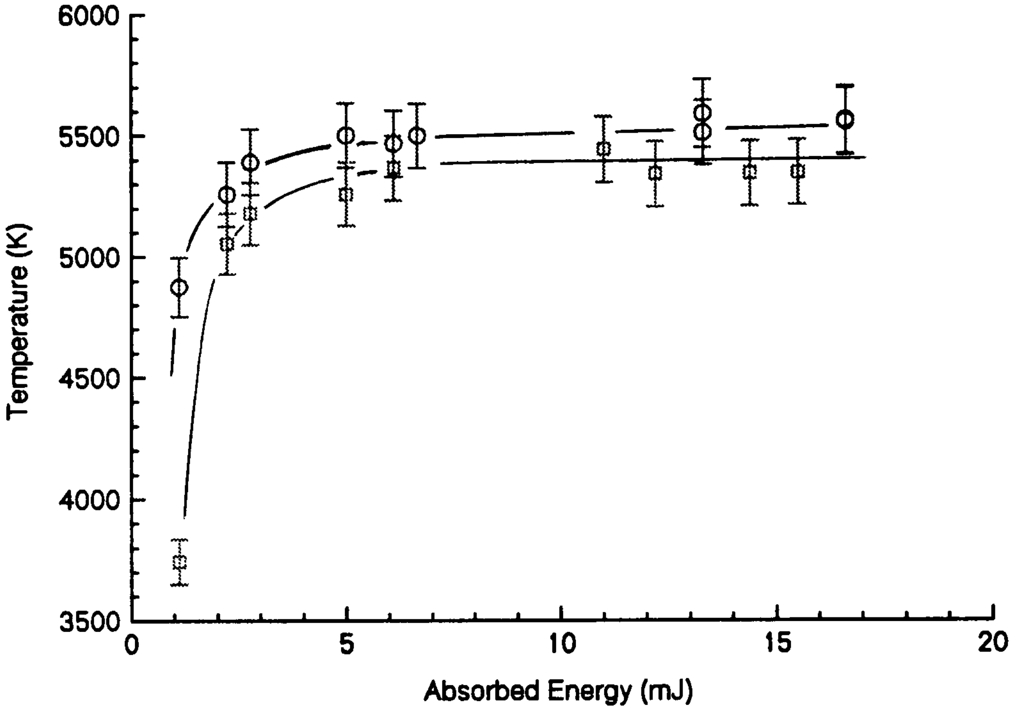

Figure 2.6: Inferred temperatures versus laser pulse energy absorbed by the optical breakdown plasma: ○ - 0.5 to 1.5 μs delay, □ - 1.0 to 2.0 μs delay.

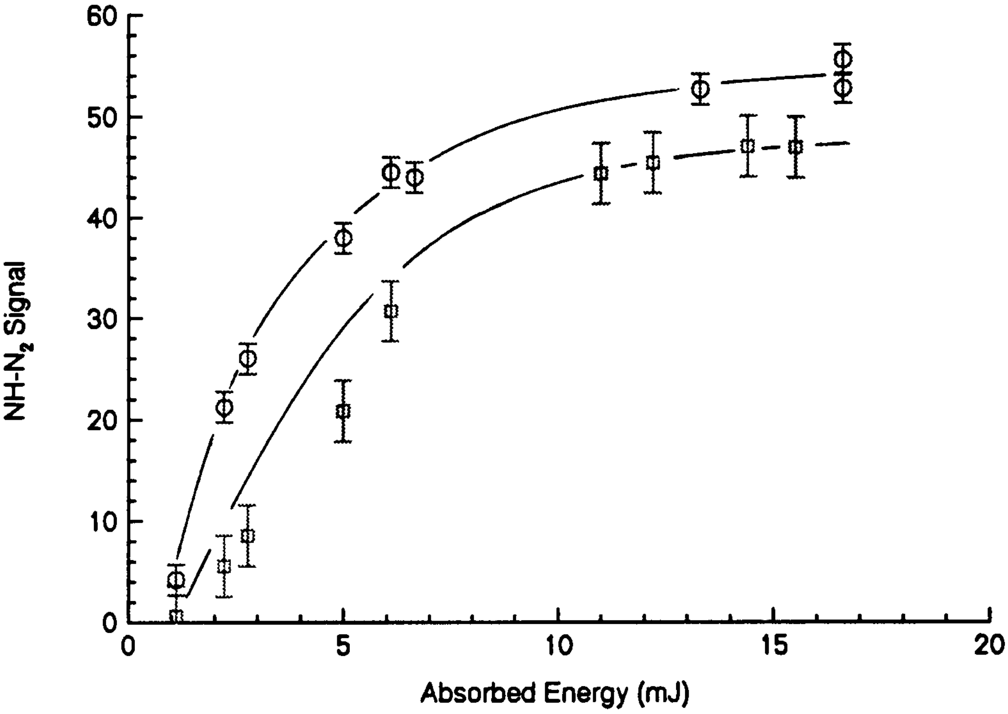

Figure 2.7: NH-N_2 signal versus laser pulse energy absorbed by the optical plasma: ○ - 0.5 to 1.5 μs delay, □ - 1.0 to 2.0 μs delay.

above.

2.5 Spatially Resolved Spectra

In this experiment, optical breakdown in pure ammonia gas at atmospheric pressure was generated by flowing the gas through a flat flame burner. The burner was positioned in front of the entrance slit of the spectrometer and the breakdown was imaged onto the entrance slit. The orientation of the slit was perpendicular to the optical axis of the focused laser beam. A CCD detector was used to record the spectra. The horizontal dimension of the CCD array records the spectral signature of the dispersed radiation and the vertical dimension of the CCD array resolves variations along the spectrometer entrance slit and hence at right angles to the optical axis of the laser beam. The laser used in this experiment was a Coherent Infinity 40-100 Nd:YAG Laser System. The average incident energy was 47 mJ and the average absorbed energy was 42 mJ. The laser pulse width was 3.5 ns FWHM.

Figure 2.8 is a pseudocolor image of the spatially resolved NH-N_2 spectra. The ordinate represents the spatial dimension of the spectrometer slit and the abscissa represents the spectral dispersion of the spectrometer. This image was acquired at a time delay of 4.8 μs after the breakdown pulse with a 1 μs gate width and represents an average of 1000 laser shots.

The same fitting procedure as described in Sections 2.1 and 2.3 was applied to these spectra. The resulting temperatures across the plasma are shown in Fig. 2.9. The uncertainties shown in Fig. 2.9 represent ± 5%. These two figures show that the spatial extent of the NH emission from the plasma is about 2 mm. Although there

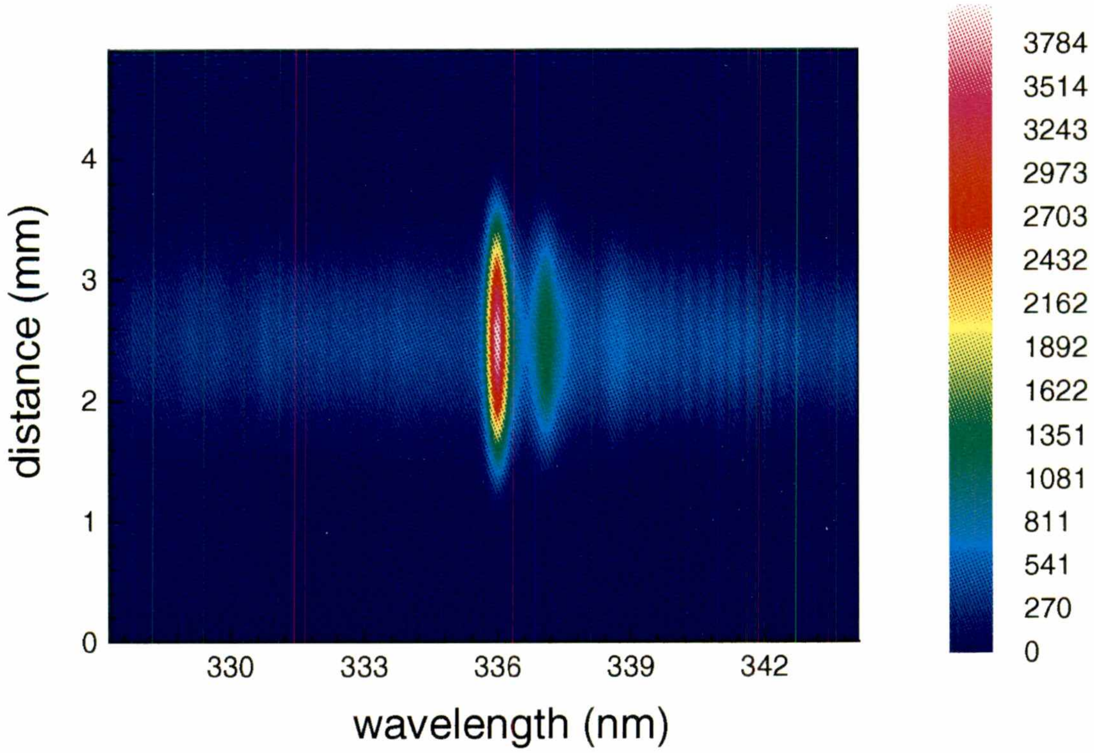

Figure 2.8: Spatially resolved NH-N_2 spectra.

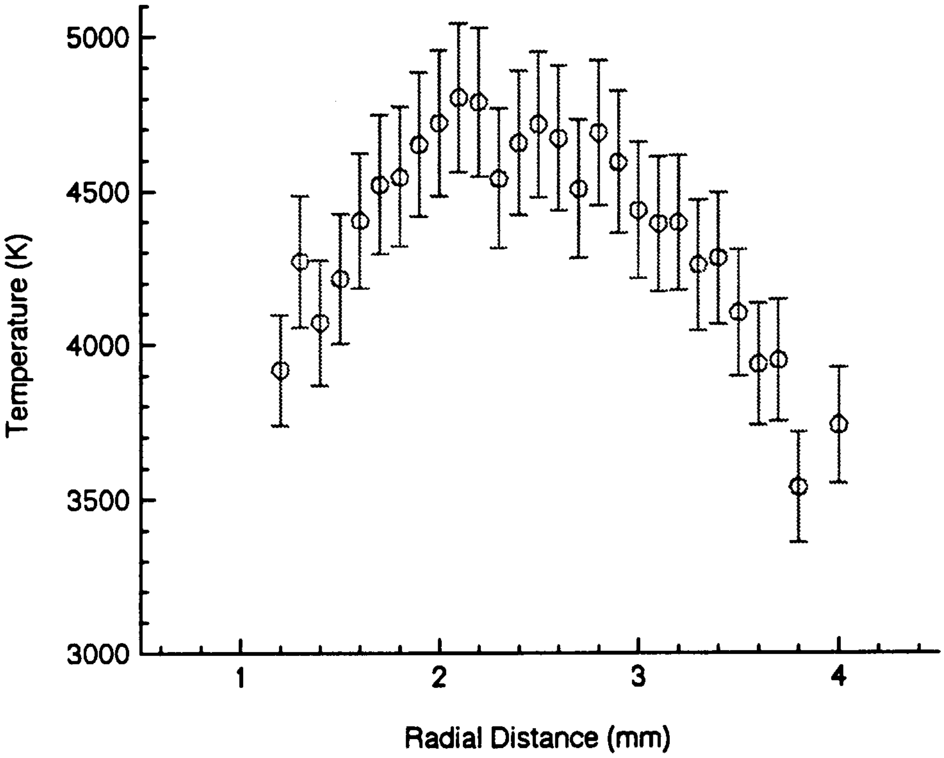

Figure 2.9: Inferred temperatures across the optical breakdown plasma.

appears to be some structure in the temperature profile, especially near the peak, the variation is fairly smooth over the NH emission region.

2.6 A Glow Discharge Spectrum

The spectrum of Fig. 2.10 shows a low resolution $\Delta v = 0$ sequence of the N_2 second positive spectrum corrupted by the 0-0 band of NH. The spectrum was dispersed and recorded using the same Jobin-Yvon spectrometer and CCD detector described above. The emission source was a commercially available low-pressure discharge tube filled with high purity nitrogen. Also shown in the figure is a nonequilibrium synthetic spectrum fitted to the data again using the NH and N_2 line strength files. This time the rotational temperature T_r, the vibrational temperature T_v, and the ratio of excited state population densities were allowed to vary. However, the vibrational and rotational temperature were assumed to be the same for the two species. From the resulting fit (T_r = 570 K, T_v = 4200 K), one can conclude that the N_2 molecules are clearly not in vibrational-rotational equilibrium, as the fitted vibrational temperature is an order of magnitude larger than the rotational temperature.

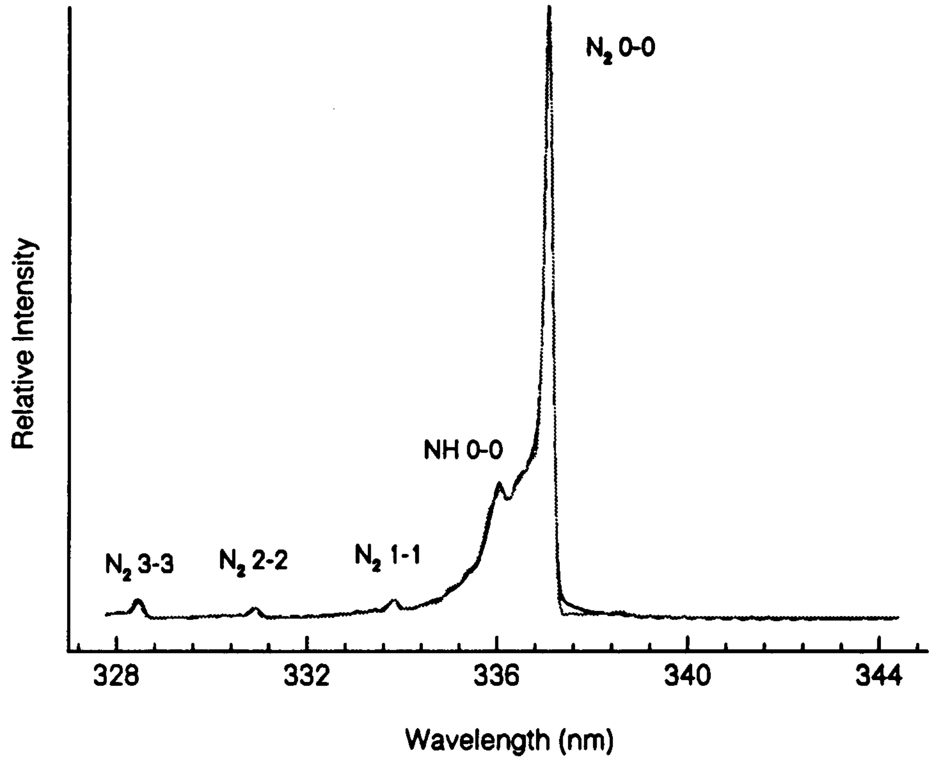

Figure 2.10: Nonequilibrium NH-N_2 experimental and theoretical spectra with T_r = 570 K, T_v = 4200 K and $[N_2]/[NH]$ = 4.7.

Chapter 3

Laser-Spark Ignition Thresholds of Ammonia-Oxygen Gaseous Mixtures

3.1 Background

Several years after the first reported observation of optical breakdown [20] researchers began to use laser sparks to study spark ignition of combustible gases [21, 22]. Following the initial pulsed ruby studies, laser ignition was extended into the ultraviolet and infrared and, as a result, new laser ignition mechanisms were discovered. These mechanisms can, in general, be grouped into four categories [23, 24]: (1) thermal ignition, where the combustible gas is heated by the presence of the laser beam to the autoignition temperature. This type of ignition usually involves infrared wavelengths and c/w lasers; (2) photochemical ignition, in which the absorption of photons initiates chemical reactions that lead to the formation of free radicals, which drive the combustion processes; (3) nonresonant spark ignition, in which a laser beam (or pulse) is focused to sufficient intensity to cause dielectric breakdown of the gas, and (4) resonant spark ignition, in which single- or multi-photon resonances are exploited to aid in the initial processes of optical breakdown. A thorough review of these four mechanisms is given in the article by Ronney [24]. Further discussion in this chapter is limited to nonresonant spark ignition generated by pulsed lasers.

Historically, spark ignition models have been developed in terms of experimentally determined parameters, such as minimum ignition energies, quenching distances and burning velocities [25]. With the increased availability of powerful computers, ignition models based on solutions of the conservation equations have begun to appear.

Modeling of spark ignition is complex. The phenomena that occur from spark formation to global combustion include aspects of nonlinear electrodynamics, plasma physics, fluid dynamics and combustion kinetics. Construction of such a model requires numerous approximations. It is therefore essential to have experimental results for different time sequence events in the ignition process to guide and to check the model. Early time behavior ($t \leq 6\mu s$) of the laser spark development and subsequent relaxation in ammonia gas were discussed in Chapter 2. Studies of early time behavior of laser sparks in hydrogen gas have previously been reported [26, 27]. In combustible gases, an important experimental parameter is the minimum ignition energy.

Spark ignition of a combustible gas is achieved by creating a plasma within the gas. The principle factors that determine whether a particular spark will develop from an ignition kernel into a sustained combustion wave are the energy deposited into the spark and the physical size of the spark channel.

A spark that results from a focused laser pulse deposits its energy into a very small spatial region. Compared to the dimensions of most practical combustion devices, the laser-spark can be approximately considered as a point source in space, and, for picosecond/nanosecond laser pulses, in time. This "instantaneous" point source deposition of energy causes very rapid heating and expansion of the gas in the focal volume. In this case, the size of the ignition kernel is determined by the energy absorbed by the spark and the physical properties of the gas.

Laser sparks are closely related, phenomenalogically, to electrical sparks. However, there are some important differences. Electrical spark time durations are usually several orders of magnitude longer than laser sparks. Typical electrical spark durations vary from hundreds of nanoseconds to hundreds of microseconds. Laser pulses used in nonresonant laser-spark ignition studies typically vary from tens of picoseconds to tens of nanoseconds. Therefore, the shock or pressure wave associated with electrical sparks is much weaker. In most cases the electrical spark duration is of the same order as the ignition delay time. Laser sparks generated using short laser pulses can be considered instantaneous on combustion kinetic time scales.

Systematic studies of minimum ignition energies using electrical sparks have been reported for most flammable gases [28]. However, only a couple of papers have been found that study spark ignition of ammonia in which the ammonia was used as the primary fuel [29, 30]. To our knowledge, there are no published laser ignition studies that use ammonia as the primary fuel.

3.2 Experimental Details

It was discovered during the course of the experiment that the minimum ignition energy threshold was less that the optical breakdown threshold for fuel equivalence ratios between ~ 0.2 and ~ 1.2. Therefore, this experiment was conducted using two separate experimental configurations. Figure 3.1 show a schematic of the experimental arrangement used to measure the minimum ignition energy for fuel/air ratios in which the ignition energies were greater than the optical breakdown thresholds. The excitation source for the optical breakdown was a Coherent Infinity 40-100 Nd:YAG Laser System operated at the fundamental wavelength of 1.064 μm. The 3.5 ns, linearly polarized, output pulses can be varied in energy from 0 to 500 mJ. However, at low energy settings the shot-to-shot repeatability was insufficient for ignition threshold studies. Therefore, the pulse energy was attenuated by placing a 45° mirror and a 0.5° quartz wedge in the optical path. The wedge also allowed us to monitor the incident pulse energy by directing the reflection from the back surface onto an energy meter (Laser Precision Corporation, Model Number RJP-734). The reflection from the front surface was used as the optical breakdown source.

The laser sparks were created by focusing the attenuated laser pulses with a 1" diameter, 4" focal length, antireflection coated, plano-convex lens into ammonia-oxygen mixtures. A second energy meter (Scientech, Model Number P50, calibrated for 1.06 μm) was placed after the optical breakdown to monitor the energy transmitted by the spark.

The relative magnitudes of the reflections from the front and rear surfaces were calibrated by comparing the two energies in instances where optical breakdown did not occur. Actually, this scenario was not difficult to achieve because, as discussed in Section 3.3.2, the breakdown threshold of ammonia is considerably less than room

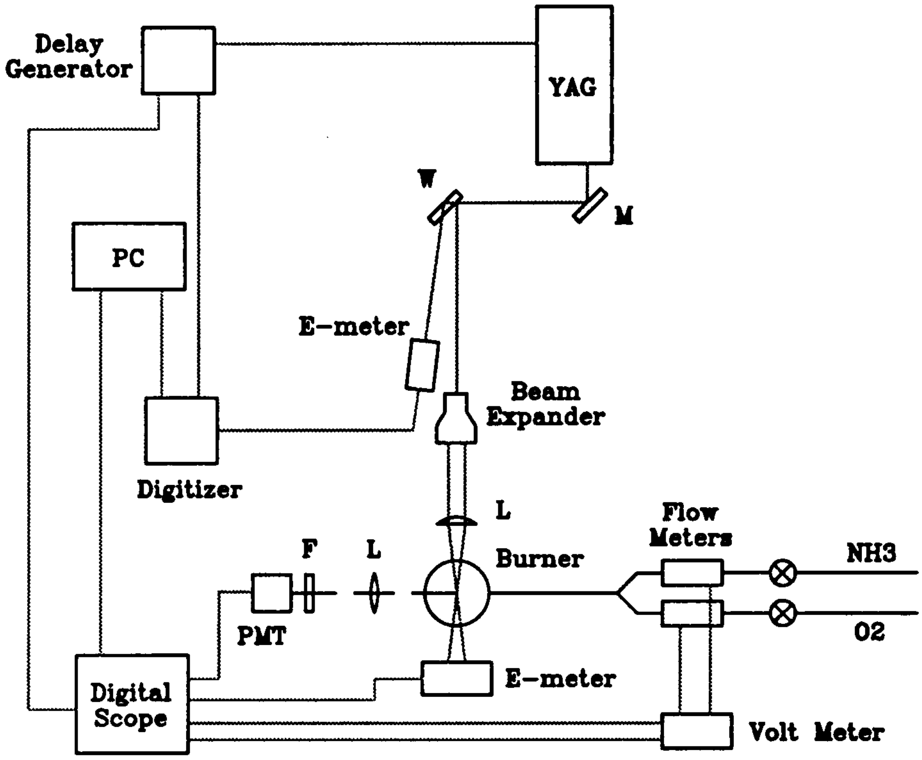

Figure 3.1: Schematic of experimental arrangement. W = 0.5° quartz wedge; M = mirror; L = lens; F = 308 nm, 10 nm FWHM laser line filter; PMT = photomultiplier tube.

air. In this way, the relationship between the measured incident energy and the true incident energy could be established. This method was preferred since the optical breakdown absorbs only a portion of the laser pulse, making it difficult to infer the incident energy from the transmitted energy measurement. It was desirable to measure the laser pulse incident and transmitted energies for each event since shot-to-shot energy variations introduced large errors into average energy measurements. In addition, each time an ignition occurred the flame had to be extinguished, thereby interrupting the gas flow and further complicating average measurements.

Photodiode traces of the transmitted laser pulses typically show that 100% of the laser pulse is removed from the pulse once breakdown occurs. Conversely, the front part of the pulse, which traverses the breakdown region before the threshold is realized, is not absorbed or scattered by the plasma and continues along the unperturbed optical path. Figure 3.2 contains schematic representations of temporal profiles in which optical breakdown does and does not occur. After the breakdown threshold is realized the photodiode trace drops to zero within a time limited, in this experiment, by the bandwidth of the measuring system (photodiode fall time < 350 ps, oscilloscope bandwidth $= 2$ ns). In Fig. 3.2(b) the optical breakdown threshold is reached at the peak of the laser pulse. If the threshold is reached at some point below the peak, then a larger fraction of the pulse energy is absorbed by the optical plasma.

Guilietti *et al.* [31] have shown that for high energy (6 J & 13 J) 20 ns FWHM pulses that 40 % or more of the incident laser pulse can be diffracted by the plasma outside the unperturbed beam cone into a forward angle not exceeding 14° for f/8 focusing optics. However, this scattering occurred for the latter portion of the laser

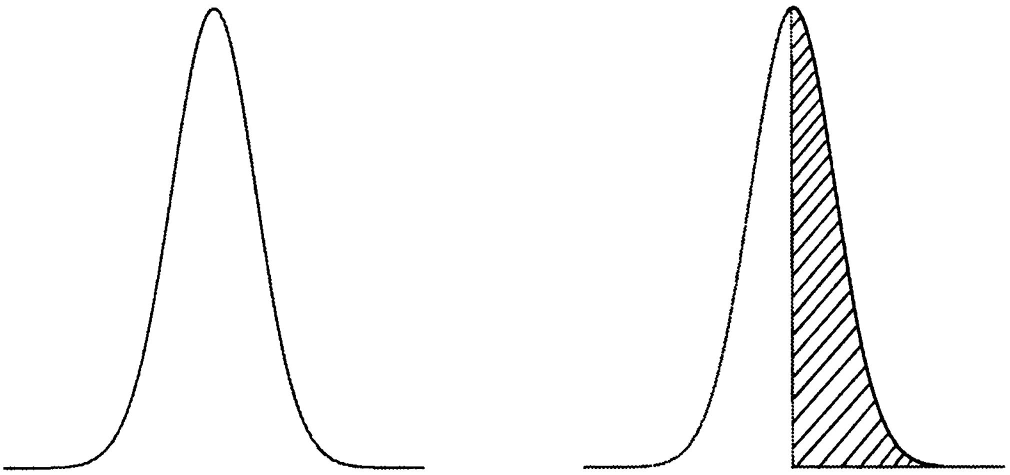

Figure 3.2: Schematic representations of temporal laser pulse profiles (a) where optical breakdown does not occur and (b) where optical breakdown does occur. The shaded region in (b) represents the pulse energy absorbed by the plasma.

pulse. Syage *et al.* [32] have verified that scattering at larger angles is negligible compared to the unperturbed portion of the transmitted pulse.

The laser pulse energies of 6 and 13 J studied by Guilietti *et al.* combined with the f/8 focusing optics resulted in power densities that greatly exceeded (by orders of magnitude) the breakdown threshold of the sample gas. For the near-threshold values in this experiment forward scattering effects were not observed. Nevertheless, as a precaution the second energy meter was positioned so forward scattering with an angle of up to approximately 20°, if present, would be included in the energy measurements.

The combustible gas mixtures were provided by flowing premixed ammonia and oxygen through a McKenna Products flat flame burner. The diameter of the burner is 6 cm and is made of sintered stainless steel. The laser pulses were focused into the center of the annulus formed by the flowing gases at a height of approximately 0.5" above the burner surface.

The flow rates of the two gases were individually monitored using calibrated flow meters. A total flow rate of 7.6 l/min was chosen for ignition studies since this flow rate produced a stationary flame on the burner for a wide range of fuel/air ratios.

For each fuel/air ratio studied, the laser pulse energy was adjusted to near the ignition threshold. The desired pulse energy was achieved when approximately one-half of the laser pulses did not result in ignition. Then, 20 to 30 measurements were made. For each laser shot, the flow rates of the ammonia and oxygen, the incident energy, the energy transmitted by the plasma, and whether or not ignition occurred were recorded.

Figure 3.3 shows a schematic of the experimental arrangement used to measure the minimum ignition energy thresholds for fuel/air ratios in which the ignition energies were less than the optical breakdown thresholds. The gas delivery and monitoring system used was the same as in the previous experiment. The excitation source was a Continuum YG680S Nd:YAG laser. The Q-switch was adjusted to yield 4.5 ns pulses at the fundamental wavelength of 1.064 was variably attenuated by directing the front surface reflections from a quartz wedge and a 5% beamsplitter through two prism beamsplitters/polarizers. The pulse energy incident on the ammonia-oxygen mixtures was controlled by adjusting the orientation of the second polarizer relative to the first. The optical breakdown threshold of the gas was reduced approximately two orders of magnitude by inserting a 0.125 inch diameter tungsten rod into the focal volume of the lens. The minimum ignition energies were obtained by measuring the average of 80 laser pulses at a setting just above and just below the ignition threshold and assuming that all but 10% of the pulse energy is absorbed by the plasma. The 10% correction factor was inferred from measured, reflected energies from a flat tungsten surface placed at a 45° angle to the incident laser pulse.

3.3 Results and Discussion

3.3.1 Minimum Ignition Energies

In initial experiments a 10 nm band-width laser line filter centered at 308 nm and a photomultiplier tube were used to monitor OH emission from ignited flames. The

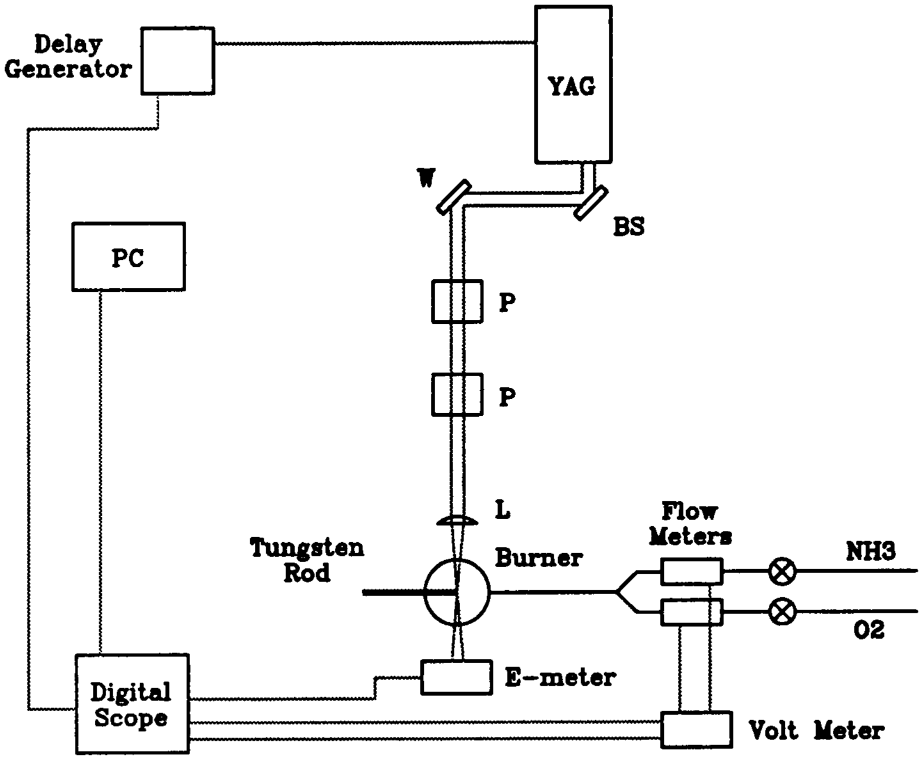

Figure 3.3: Schematic of experimental arrangement. W = 0.5° quartz wedge; BS = 5% beam splitter; L = lens; P = polarizer.

presence of OH emission was used to indicate if ignition had occurred. It was noted that the OH emission was directly correlated with visual observation of a flame. As a result, in subsequent experiments, an ignition event was said to occur when a steady flame was established on the burner when the fuel equivalence ratio (ϕ) and flow rates were in the range where the burner would support a steady flame. For very lean mixtures ($\phi \leq 0.2$), ignition was said to occur when a flame was visible to the eye under low light conditions.

Figure 3.4 gives the resulting minimum absorbed ignition energies as a function of the fuel equivalence ratio. Figure 3.5 shows these same energies but with the percentage of fuel by volume plotted as the abscissa. In these plots the maximum non-igniting and the minimum igniting pulses are used to determine the minimum ignition curve. The shaded region between 200 and 300 μJ absorbed energy indicates the optical breakdown threshold limit. The points below this region were acquired with the tungsten rod inserted into the optical path of the laser pulses. The larger relative errors observed in Figs. 3.4 and 3.5 are due to uncertainties introduced in the average energy measurements and uncertainties in the amount of total pulse energy absorbed by the optical plasma.

Also shown in Figs. 3.4 and 3.5 are the electrical spark results obtained by Verkamp *et al.* [29] for ammonia-air mixtures. The curve drawn through the laser ignition points predicts a minimum of 50 to 60 μJ at $\phi \simeq 0.6$ (or % ammonia $\simeq 45$), whereas the electrical spark ignited ammonia-air minimum energy is 7 to 8 mJ and lies at $\phi \simeq 0.85$. A shift to lower equivalence ratio (or higher % fuel) with increased oxygen concentration is observed with spark-ignited hydrocarbon fuels. For gaseous hydro-

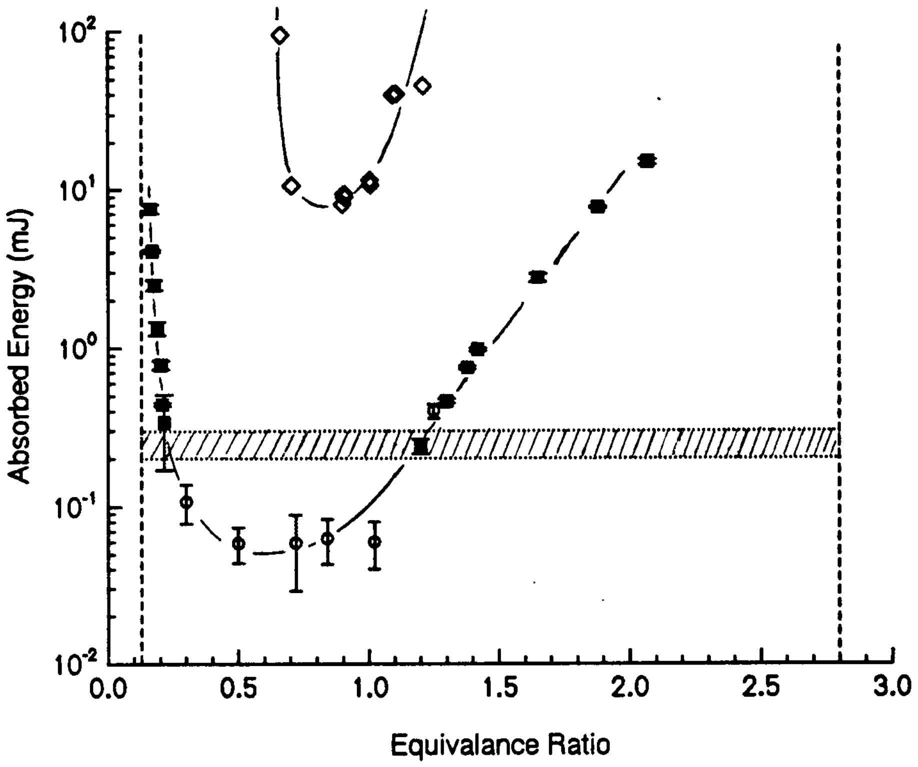

Figure 3.4: Minimum ignition energy versus fuel equivalence ratio. □ = ignition energies that lie above the optical breakdown threshold, o = ignition energies that lie below the optical breakdown threshold, ◇ = ammonia-air electrical spark result of Verkamp *et al.*

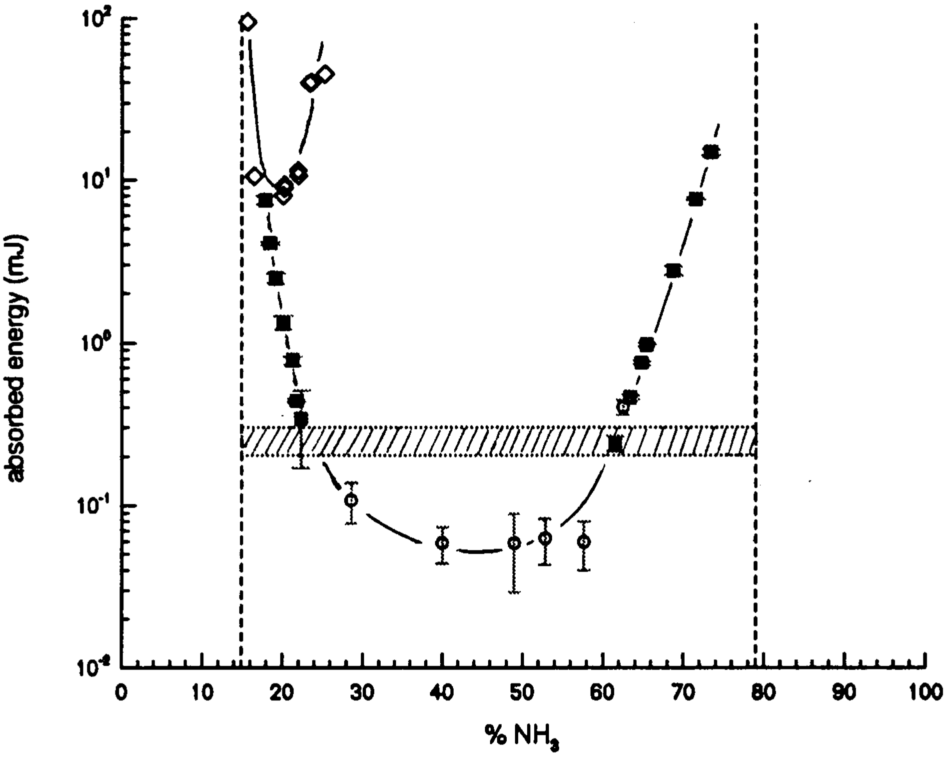

Figure 3.5: Minimum ignition energy versus percent ammonia. □ = ignition energies that lie above the optical breakdown threshold, o = ignition energies that lie below the optical breakdown threshold, ◇ = ammonia-air electrical spark result of Verkamp *et al.*

carbon fuels such as methane, ethane, and propane the minimum spark energies of fuel-air mixtures at atmospheric pressure are approximately two orders of magnitude higher than those of fuel-oxygen mixtures at the same pressure [25]. This ratio and the shift to lower fuel equivalence ratio are observed in the ammonia-oxygen results as well.

3.3.2 Optical Breakdown Threshold

In order to establish the minimum laser requirements for laser-spark ignition and the limitations in minimum ignition studies the optical breakdown threshold of (1) air, ammonia and oxygen using the Coherent Infinity laser and (2) ammonia using the Continuum YG680S Nd:YAG laser were measured. The minimum laser requirements are determined by the ability to focus a laser pulse to sufficient intensity to create optical breakdown in the gas sample. The ability to focus depends primarily on the beam divergence and on the longitudinal mode quality of the laser. These parameters vary from laser to laser. The limitation to minimum ignition studies refers to the fact that the laser pulse will not ignite the gas mixture unless optical breakdown is achieved. If the optical breakdown threshold is too high, as in the case of the 3.5 ns, 1.064 μm pulses, then more energy than is required to light the gas mixture will be absorbed from the pulse.

In the first experiment, the threshold energies were measured using the calibrated energy meter in air, pure ammonia, and pure oxygen. Focused intensities were inferred by recording the beam profile at the focusing lens plane and calculating the focused beam waist. The beam waist calculation is described in Appendix A. The resulting intensities are 170±15 GW/cm^2 for ammonia, 290±10 GW/cm^2 for oxygen and 280± 15 GW/cm^2 for room air. The uncertainties are inferred from energy measurement uncertainties.

Ideally, the Infinity laser has a diffraction limited circular top-hat output beam. Our threshold measurements were made in the far field. Therefore, with perfect alignment of the laser components, one would expect the beam intensity profile to be the Fraunhofer diffraction pattern from a circular aperture. However, the measured profile differed from the ideal diffraction pattern. In Fig. 3.6 the recorded laser pulse is shown. Note the asymmetry in the wings of the pulse and the indication of the Airy disk first minimum near the top of the image. Figure 3.7 shows a trace of the normalized intensity versus distance, extracted from bottom to top across the peak of the two dimensional profile shown in Fig. 3.6, together with an Airy function and Gaussian intensity profile. The Airy function is scaled so that the peak and first minumum coincide with the laser pulse intensity trace. The Gaussian was calculated from least squares best fit width parameter. For Gaussian input beams, the nonaberrated, focused beam waist (ω_0) can be calculated using

$$\omega_0 = \frac{\lambda f}{\pi \omega_1}$$

where λ is the laser wavelength, f is the focal length of the lens, and ω_1 is the beam waist of the input beam. Using the best fit Gaussian as the input beam ($\omega_1 =$ 2.14mm), this expression yields $\omega_0 = 15.8\mu$m, with $\lambda = 1.064\mu$m and f =10 cm. The computer code discussed in Appendix A also yields 15.8 μm for the focused beam

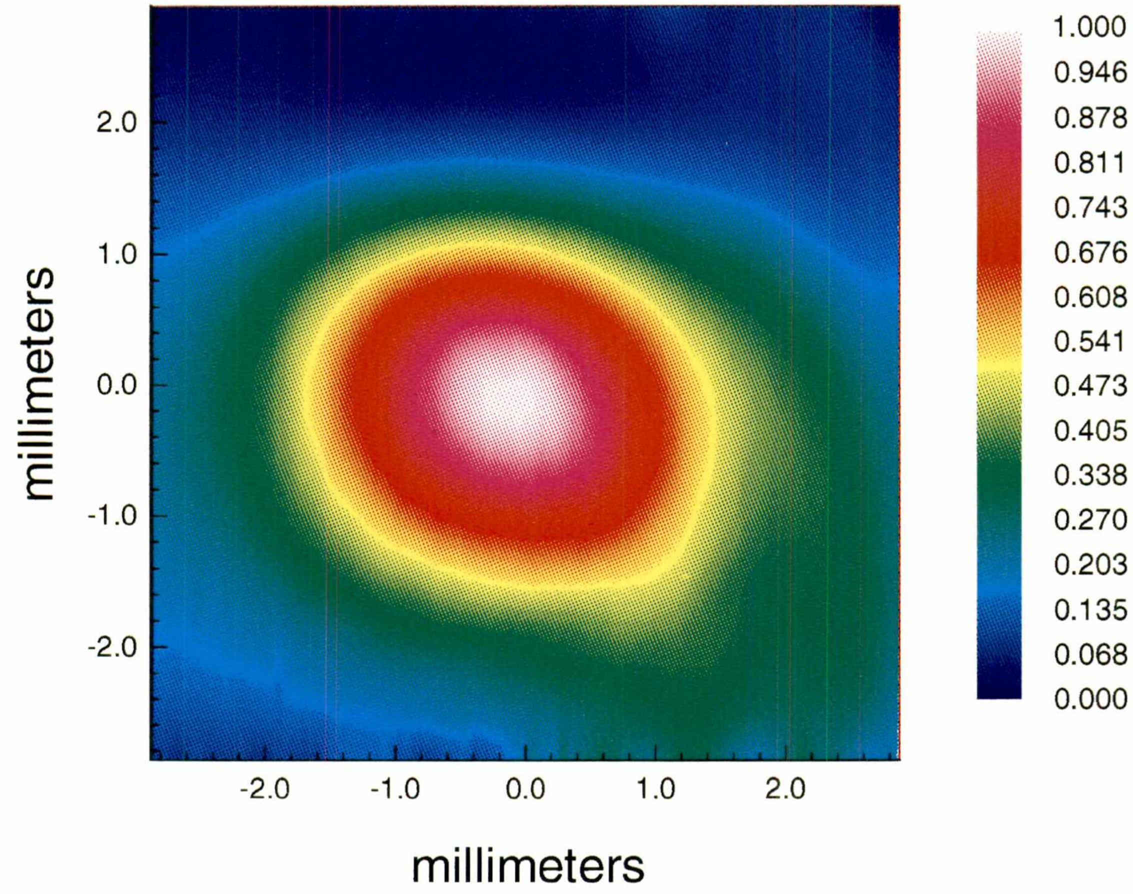

Figure 3.6: The measured intensity distribution of an Infinity laser pulse.

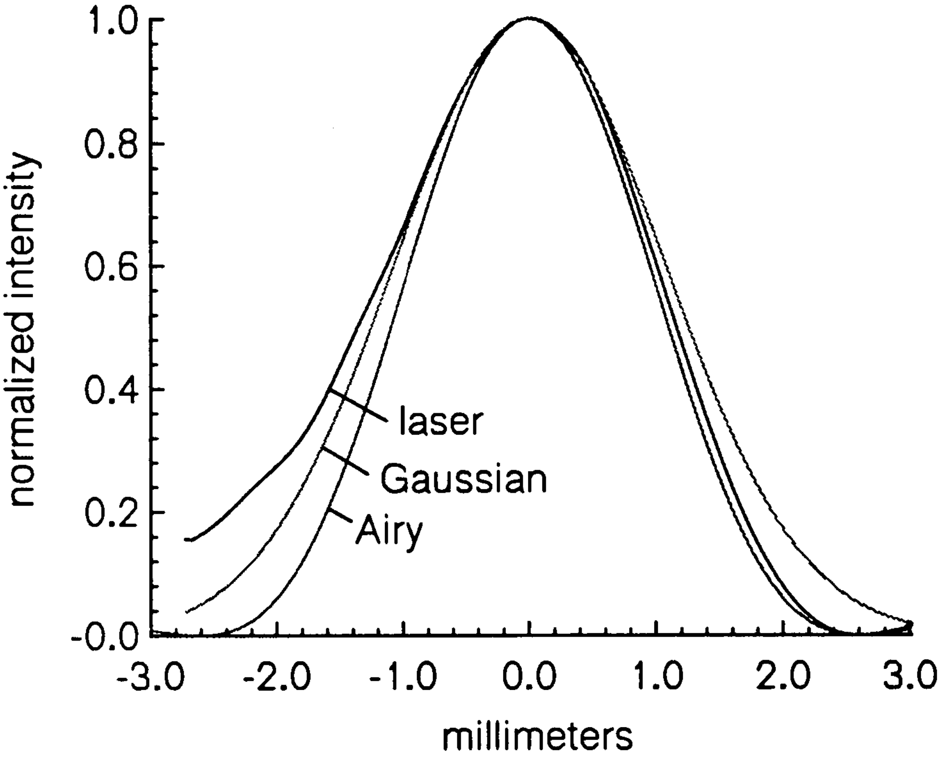

Figure 3.7: Typical laser pulse intensity profile, a best fit Gaussian, and a scaled Airy function profile.

waist. For the Airy function input profile, the computer code gives $\omega_0 = 27.4\mu$m. Calculated focal plane radial intensity distributions for the Gaussian and Airy function input beams are shown in Fig. 3.8. Figure 3.9 shows a cross-section of the calculated beam focus for the measured, two dimension, intensity profile. The beam waist inferred from this figure is 14.7 μm. The 'squareness' of the beam for low intensities near the edges is an artifact of the square geometry of the CCD chip used to record the spatial cross-section pulse profile. However, near the center of the image the edge effects are negligible.

In the second measurement a gas cell was filled with high-purity ammonia to one atmosphere. The breakdown threshold energy was established with 30 ns laser pulses. The intensity at threshold was determined by measuring the focused beam waist of attenuated laser pulses in a fluorescent dye solution. The inferred breakdown threshold in this experiment is 35 ± 8 GW/cm^2, where the error is primarily due to uncertainty in the beam waist ($\omega_0 = 44 \pm 5\mu$m).

For the intensity profiles discussed in this section, the beam waist (ω) is taken as the average radial position where the intensity has decreased from its peak value by a factor of $1/e^2$. The focused intensities are determined by averaging the measured pulse energy over an area $\pi\omega_0^2$.

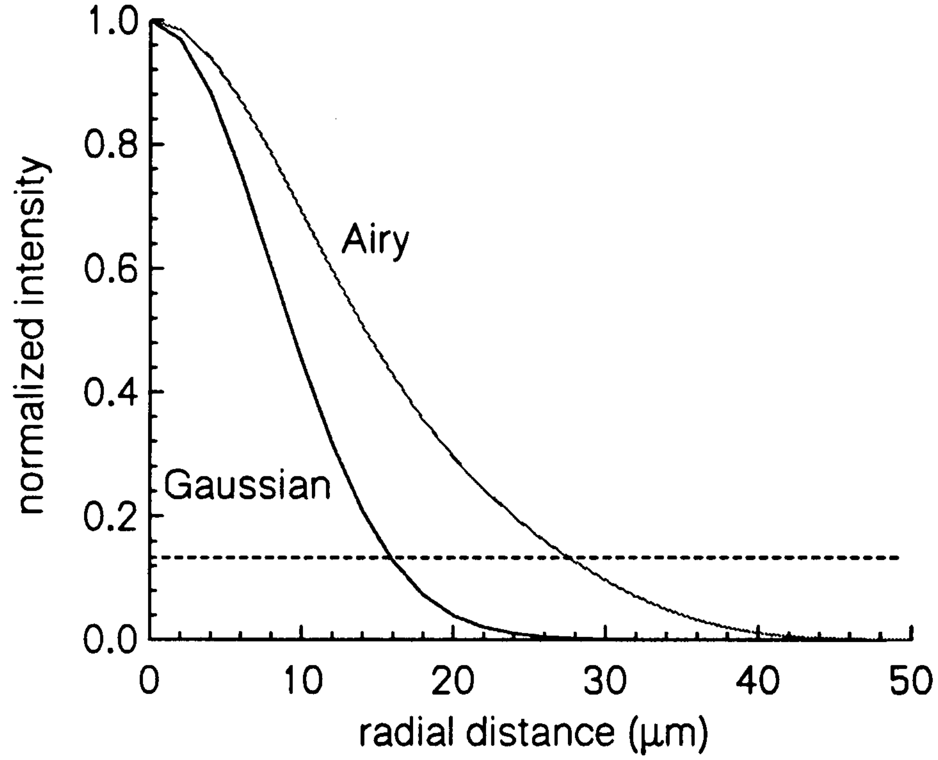

Figure 3.8: Computer code calculated focused radial profiles of a Gaussian and Airy function input beam.

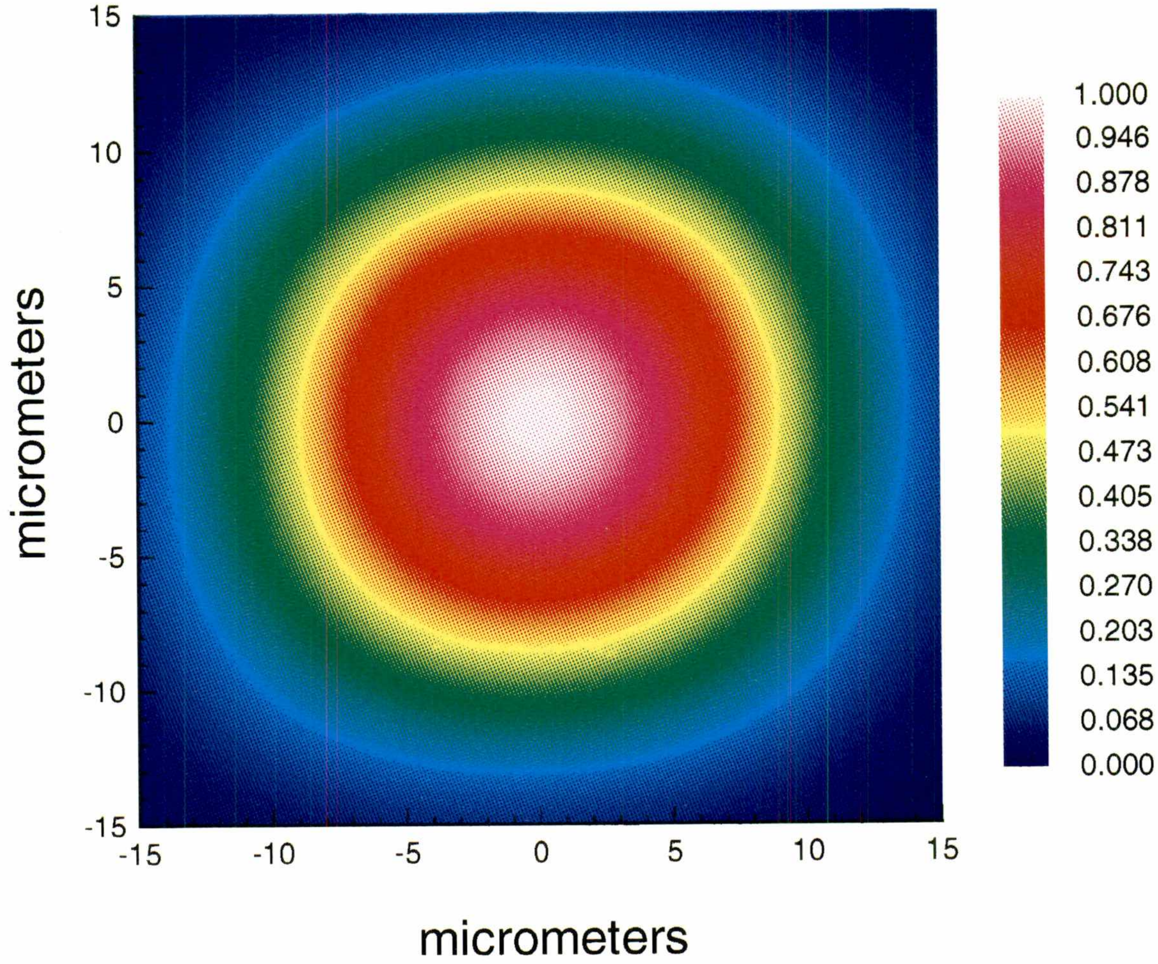

Figure 3.9: Intensity distribution of the calculated beam focus.

Chapter 4

Flame Speeds of Laser Ignited Premixed Ammonia-Oxygen Gas

4.1 Background

Optical plasmas resulting from focused laser beams or pulses have been shown in previous studies to be effective ignition sources in combustible gas mixtures [21, 22, 32, 33, 34, 35, 36, 37]. For short pulsed lasers (on the order of 10's of nanoseconds or less) focused to less than 50 microns in diameter, the resulting optical breakdown (laser spark) in the gas mixture can be approximately considered as an instantaneous, point ignition source. The actual breakdown region can be roughly visualized as the volume that results from the product of the focal spot area and the Rayleigh range – a cylindrically symmetric volume whose length along the optical axis is larger than its width by a factor equal to twice the f/# of the focusing lens. With a f/# of 5 and a beam waist of 25 μm, the initial laser spark will have a width of 50 μm and a length of 500 μm. On distance scales of several centimeters or larger, the submillimeter differences in the dimensions of the initial spark will be negligible. Thus, laser spark ignition results in a nearly spherical, outwardly diverging flame.

A freely propagating flame consist of a very well defined deflagration wave – or reaction front – where the fuel and oxidizer are rapidly heated and the chemical reactions that involve numerous free radicals and reaction intermediates occur. The deflagration wave is preceded by a preheat zone of comparable thickness and succeeded by the combustion products. Also associated with the reaction front is a rapid decrease in the gas density and a rapid increase in particle velocity that naturally follows the temperature rise. The gradients and magnitudes of the preceding events are strongly dependant on the fuel-air ratio. Typical results of a theoretical laminar (i.e. one dimensional) flame calculation [4] are shown in Fig. 4.1 for an ammonia-oxygen flame with a fuel equivalence ratio of 1.0. The results demonstrate that the reaction zone for $\phi = 1$ is clearly less than 0.5 mm.

If the flame front thickness is assumed negligible compared to its distance from the ignition source, then the spherically expanding flame front can be related to a laminar flame velocity by [38, 39]

$$S_L = (\rho_b/\rho_u) dr_f/dt. \tag{4.1}$$

In Eq. 4.1, S_L is the laminar flame speed, ρ_b and ρ_u are the densities of the burned and unburned gases, respectively, and r is the radial distance of the flame front from the ignition source. The negligible flame front thickness approximation requires that the flame front radius measurements be made as far from the ignition source as possible.

Flame stretch associated with expanding deflagration waves can, under certain conditions, induce instabilities in the flame front. No instabilities were noted in the gas mixtures reported here.

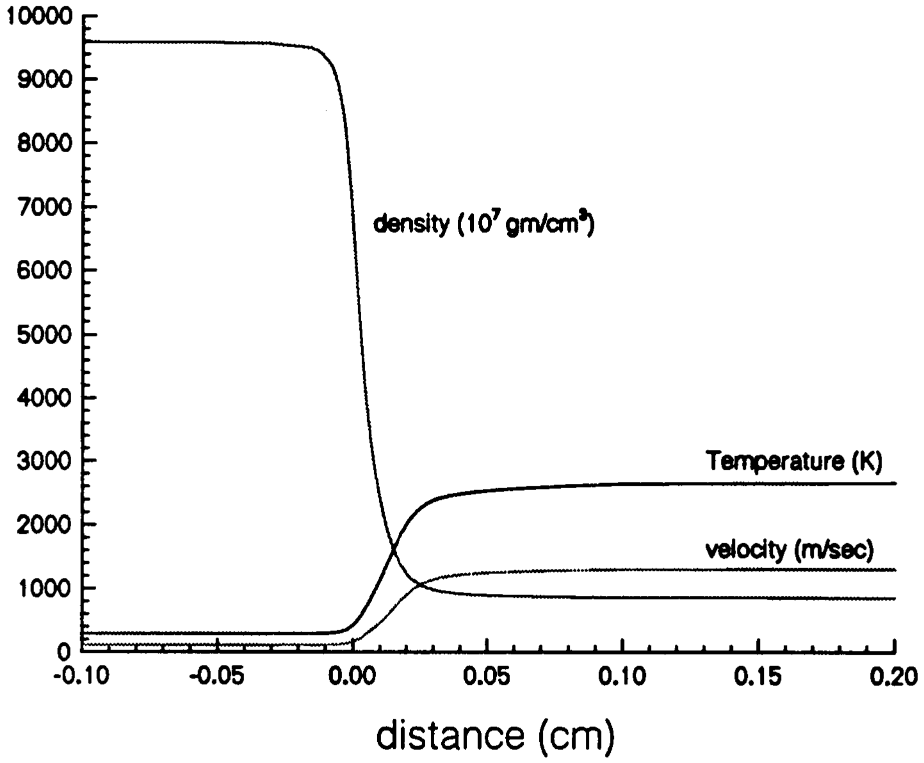

Figure 4.1: Theoretical velocity, temperature, and density profiles for a freely propagating stoichiometric ammonia-oxygen premixed flame.

In Chapter 3, minimum ignition energies for laser ignition of ammonia-oxygen gaseous mixtures were studied. Here flame speed measurements over the same fuel equivalence ratios are reported. The measured flame speeds are compared to theoretical values calculated using the one dimensional premixed flame code of Kee *et al.* [4] and the reaction mechanism as found in Ref. [40].

4.2 Experiment

Premixed ammonia-oxygen gas mixtures of variable fuel/air ratios were flowed through the flat flame burner (McKenna Products) at a constant flow rate of 7.6 l/min. A constant total flow rate was used over the entire range of fuel/air ratios studied to ensure that effects of the bulk gas flow velocity would be consistent between data sets. The flow rates of the individual gases were monitored using calibrated mass flow meters. Use of the flat-flame burner greatly simplified the experiment compared to combustion bomb studies in terms of gas handling, and it eliminated the boundary effects that occur in closed containers. However, the flat flame burner restricted flame propagation measurements to regions far from the edge because of diffusive mixing with atmospheric gases. Although the burner is equipped with a sheath gas ring on is periphery, it had to be removed as it was made of brass, which is corrosive in ammonia.

The gases were ignited using single pulses from the Coherent Infinity Nd:YAG laser. The fundamental wavelength of 1.064 μm was used. The laser pulse width was 3.5 ns FWHM. Large variations in absorbed energy result in fluctuations in the ignition kernel diameter at a given time delay. Therefore, the laser pulse energy was adjusted to several millijoules above threshold ensure repeatable absorbed energies. The incident and absorbed energies were monitored using a 0.5° quartz wedge and two energy meters as shown in the experimental layout in Fig. 4.2.

The shadowgraph images were acquired using 308 nm, 10 ns XeCl excimer laser pulses which were synchronized to the Nd:YAG laser ignition pulses through an external delay generator. The backlight excimer pulses were used to image the developing flame kernel at a preselected time delay with respect to the ignition pulses. A CCD camera was used to record the shadowgraph images directly onto a PC. The camera is equipped with an electronic shutter. The minimum gate attainable with this shutter is 1 ms. A typical sequence of shadowgraphs is shown in Fig. 4.3. In these images the Nd:YAG laser is incident from the left.

After each ignition event, the flame was extinguished by interrupting the gas flow to the burner. Therefore each shadowgraph image was acquired from a separate ignition event. This procedure introduced a small variation in the gas flow rates, which resulted in a maximum standard deviation in the fuel equivalence ratio of 2%, although in most cases the standard deviation was less than 1%.

A particular experimental sequence consisted of the following. The predetermined flow rates of the ammonia and oxygen were individually established through the burner. When the gas flow rates stabilized, the Nd:YAG laser was fired with the external delay generator. The trigger out circuit of the delay generator was used to trigger a digital oscilloscope (LeCroy, Model No. 9314) to record the gas flow rates and the transmitted energies. At the appropriate time, the delay generator was trig-

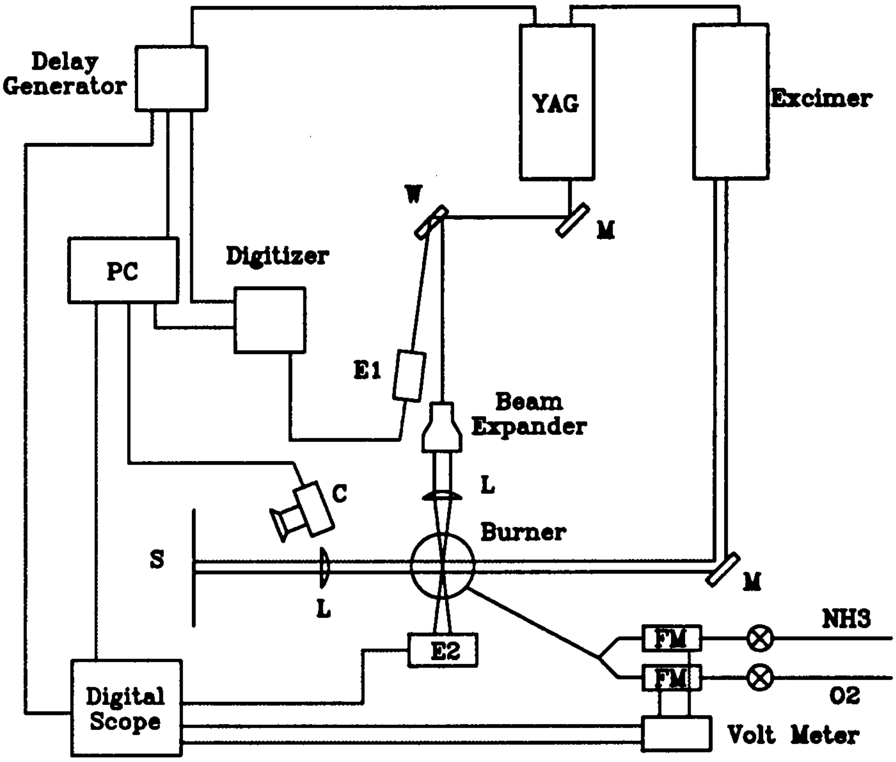

Figure 4.2: Schematic of the experimental arrangement. FM = flow meter, L = lens, M = mirror, E1 = energy meter (Laser Precision, Model Number RJP-734), E2 = energy meter (Scientech, Model Number P50), W = quarts wedge, C = camera.

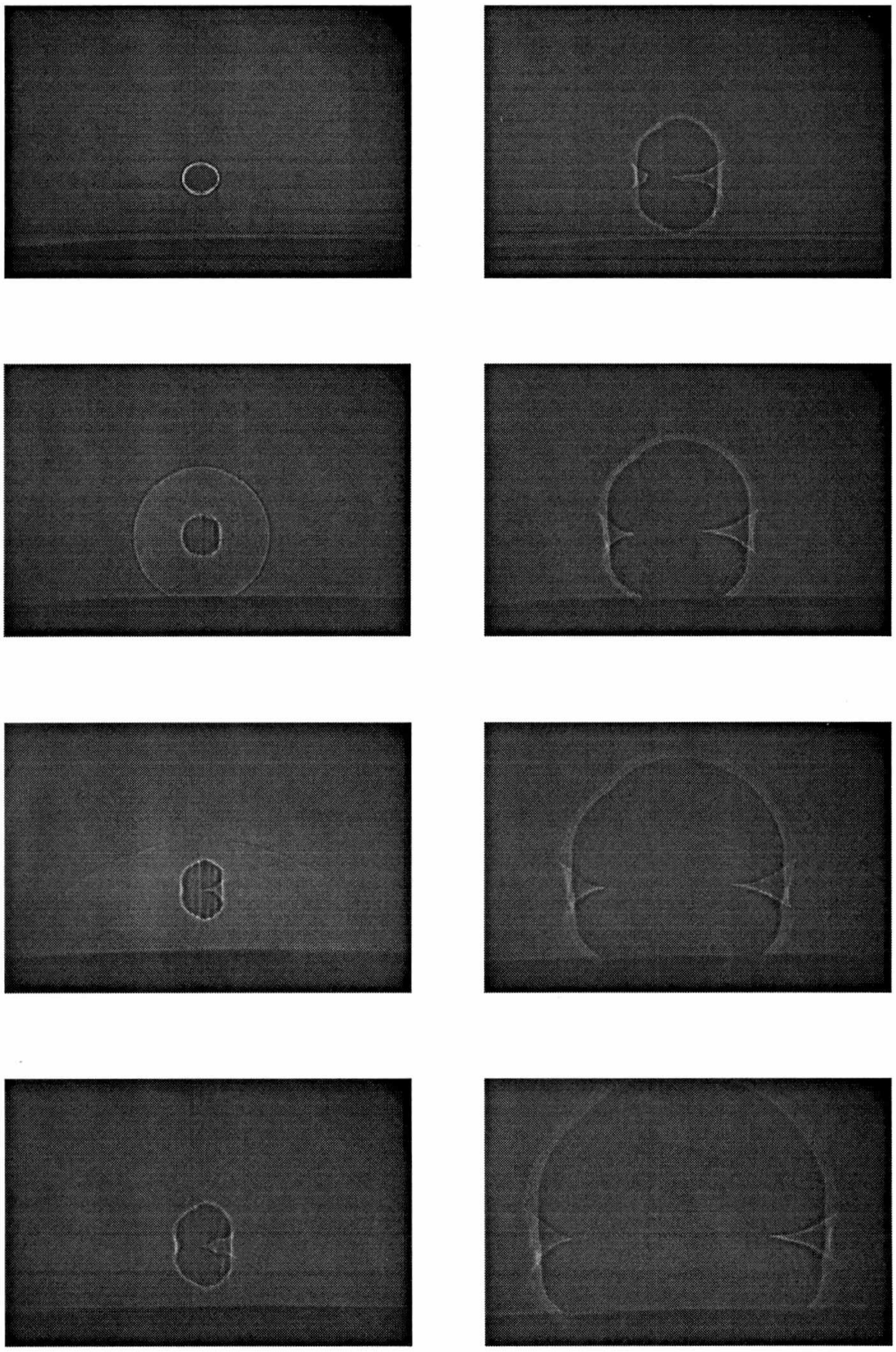

Figure 4.3: Shadowgraph images showing the temporal development of a laser ignited 'spherical' flame. The time delays of the images are 1, 10, 40, and 60 μs in the left column and 200, 400, 600, and 800 μs in the right column.

gered the excimer laser, the CCD camera electronic shutter, and the incident energy meter digitizer. A personal computer then stored the gas flow rates, energy meter readings, and the camera image. After the ignition event, the gas flow was interrupted, thereby extinguishing the flame. The backlight laser and CCD camera delays were incremented and the process repeated until the flame front propagated beyond the field of view of the camera.

4.3 Analysis and Results

The magnification of the optical system used to acquire the shadowgraph images was determined from an image of a calibration grid. The resulting magnification was approximately 5× with a field of view of approximately 4 cm horizontal by 3 cm vertical.

The expanding flame front was measured on the left and right border, and when possible, on the top and bottom border. These points were used to determine the radius of the flame front at the different time delays. Representative radius versus time plots for various fuel equivalence ratios are shown in Fig. 4.4. Flame speeds were determined through linear fits to the radius versus time curves as shown in Fig. 4.5. It can be seen from the these two figures that the flame speed deviates from linearity over the measured distances. The linear fits were applied to the larger radius points to ensure, as well as possible, a negligible flame front thickness. The nonlinearity of the curves was used to assign uncertainties to the resulting velocities. The flame speeds were measured both along the optical path of the breakdown pulse and perpendicular to it – no significant differences were found.

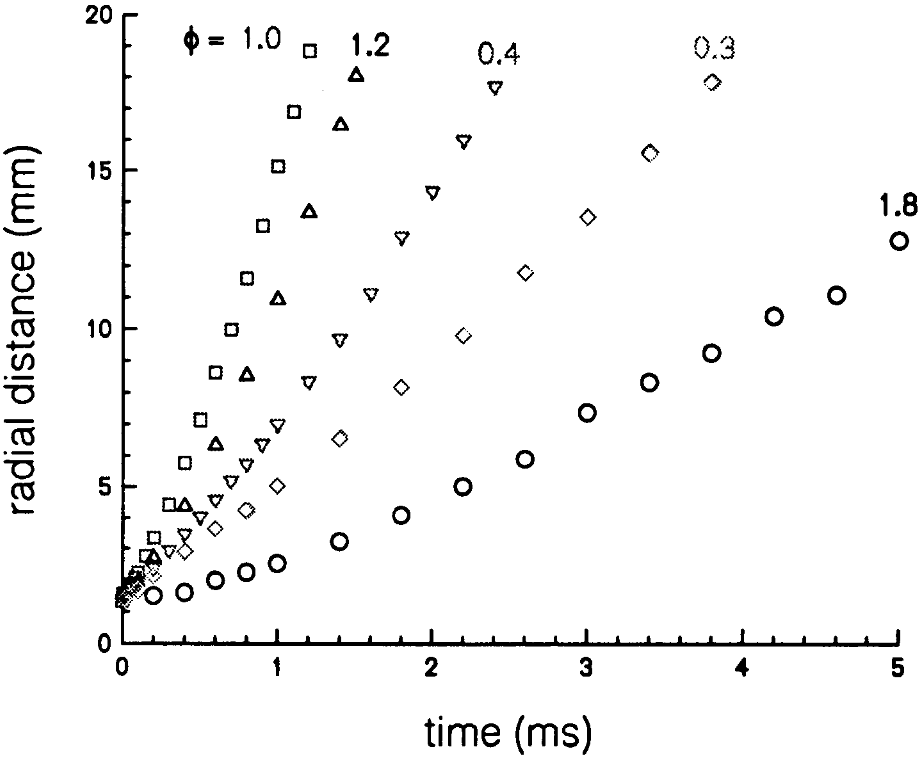

Figure 4.4: Typical flame front radius versus time results.

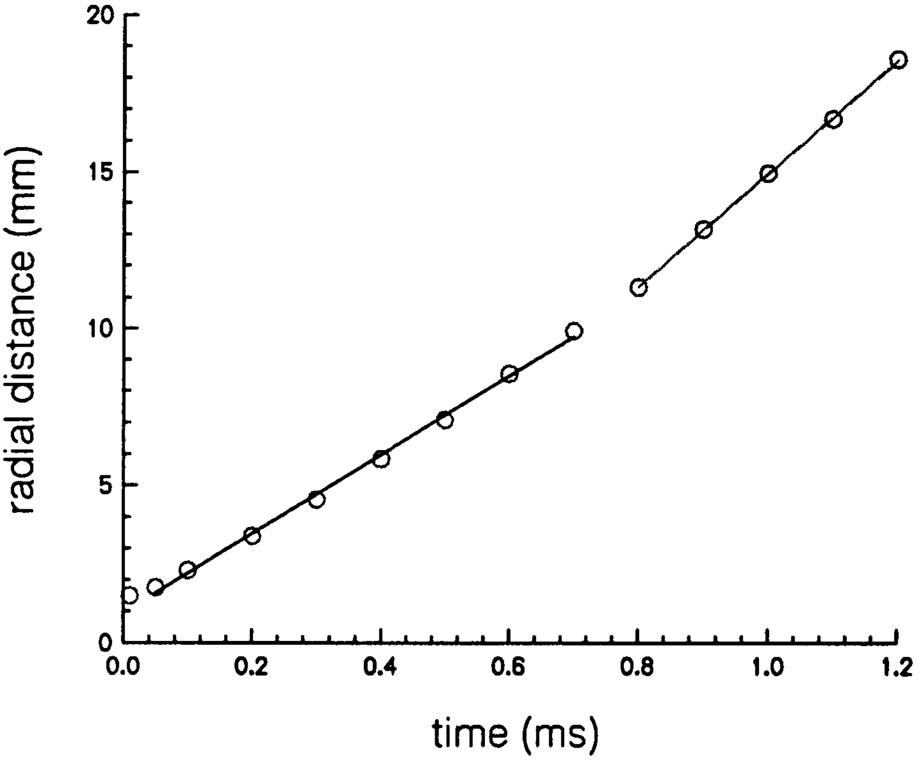

Figure 4.5: Linear fits to the $\phi \simeq 0.8$ flame front radius versus time plot.

The burned gas densities used in Eq. 4.1 were determined using the Gordon-McBride code [16], which calculates the burned gas properties based on the assumption of chemical equilibrium. The measured flame speeds were converted to laminar flame speeds by multiplying them by the density ratio of burned to unburned gas as prescribed in Eq. 4.1.

Theoretical flame speeds were calculated using the CHEMKIN chemical kinetics code by considering reactions between the following molecules: H_2, O_2, H, O, OH, HO_2, H_2O_2, H_2O, N_2, N, NO, NO_2, HNO, NH_3, NH_2, NH, N_2H_4 and N_2H_3. The rate constants used in the calculation, taken from Ref. [40], are listed in Appendix B. The theoretical flame speeds were calculated over the range of experimental fuel equivalence ratios. The calculated and experimental results are shown together in Fig. 4.6. As can be seen, the agreement between experiment and theory is quite good except for the fuel rich region where the theory overpredicts the experimental values. The equivalence ratio for the maximum measured flame speed occurs at $\phi \simeq 1.0$ which is in good agreement with the calculated values.

For fuel equivalence ratios greater than or equal to 1.6, the combustion wave was observed to stream back toward the laser at a higher rate than was observed for the other directions. This effect has also been observed by Spiglanin *et al.* [33] in Nd:YAG laser-spark ignited H_2-O_2-Ar mixtures and by Seitzman *et al.* [41] in excimer laser ignition of hydrocarbon-air mixtures. A time sequence of shadowgraphs obtained for $\phi = 1.6$ ammonia-oxygen mixtures is shown in Fig. 4.7. In such cases, the near spherical symmetry of the ignition kernel is destroyed. However, note that an axial

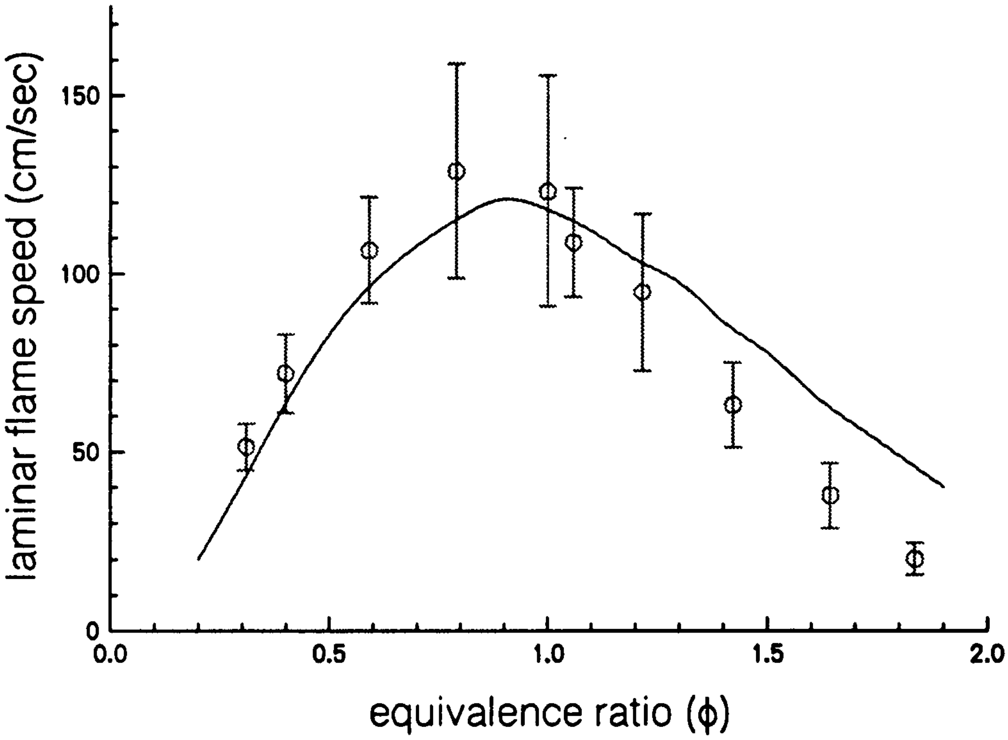

Figure 4.6: Experimental and theoretical laminar flame speeds.

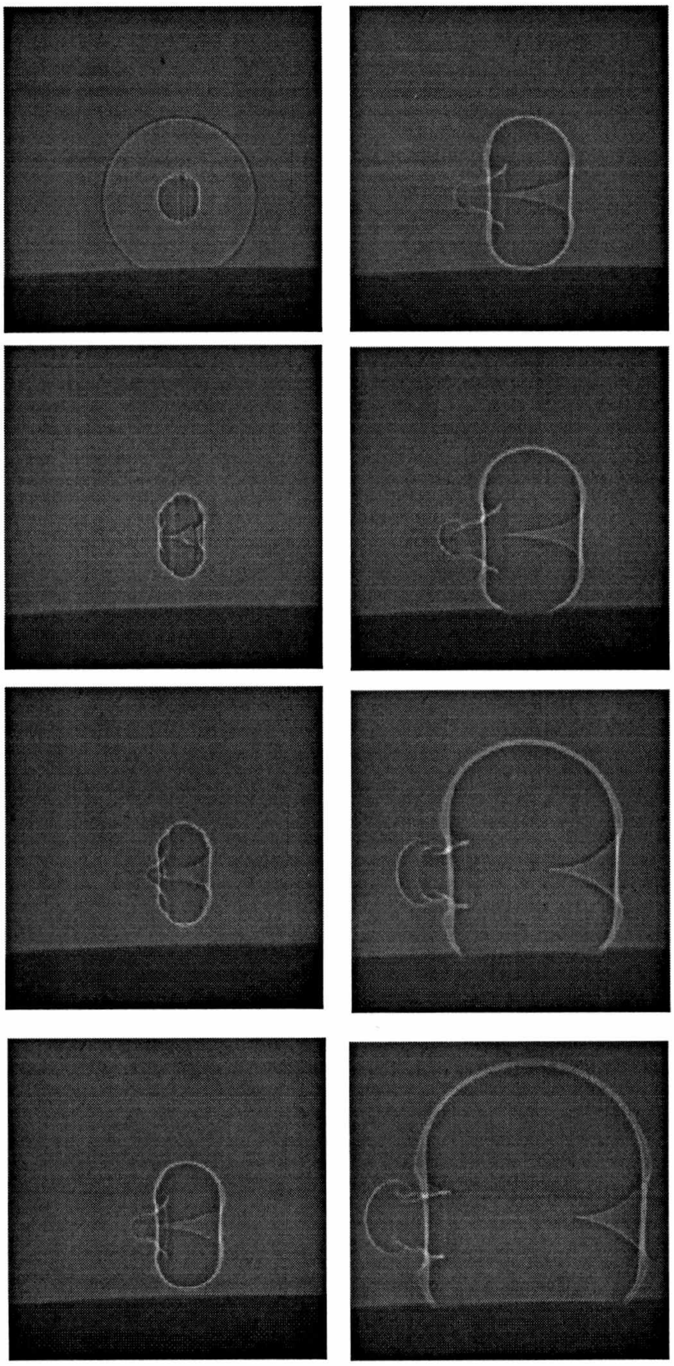

Figure 4.7: Shadowgraph image of the developing laser-ignited flame, which shows the backward propagation of the flame kernel. The time delays of the images are 10, 100, 200, and 400 μs in the left column and 600, 800, 1400, and 1800 μs in the right column.

symmetry, with respect to the optical axis, is preserved. It is possible that the destruction of the spherical symmetry could account for the observed differences between the experiment and theory observed in Fig. 4.6 on the fuel rich side of the plot. It is also possible that the increased flamefront thickness at the higher fuel equivalence ratios introduces errors through Eq. 4.1 although such differences between theory and experiment are not observed on the fuel lean side of the curve, where flamefront thickness is also increased.

Chapter 5

Planar Laser-Induced Fluorescence Imaging of Laser-Spark Ignition

5.1 Overview

Laser-induced fluorescence (LIF) is a species specific diagnostic technique that can be used to nonintrusively measure such quantities as temperature, number density, and velocity. LIF can be also be used to image both atomic and molecular species and has a wide range of applications. Since this chapter deals with gas phase phenomena, further discussion is limited to LIF imaging of gas phase phenomena, particularly ignition and combustion processes.

LIF imaging can be used to measure the spatial distribution of many of the atoms and molecules that participate in the complex sequence of chemical reactions that occur during ignition and combustion of reactive gases. For steady state conditions, such as those that occur in burner stabilized premixed flames LIF images may be acquired over long integration times without regard to time resolution [42, 43, 44, 45, 46]. Two dimensional images may be acquired with two dimensional detectors or may be built up from a series of one dimensional measurements.

Under transient conditions, such as in turbulent diffusion flames [47, 48, 49] or ignition events [33, 50], the images must be acquired with a time-differentiating detection system. Using a sheet or planar probe laser pulse and a two dimensional detector, single event images can be acquired at a selected time delay. Thus, by employing planar laser-induced fluorescence (PLIF) techniques, one can acquire spatially and temporally resolved "snapshots" of the atomic or molecular species under consideration. The goal of this experiment was primarily to image the formation of the free radicals that lead to combustion after an optical plasma has been created in a combustible ammonia-oxygen mixture.

The history of events leading to nonresonant laser-spark ignition of combustible gases includes the creation of a laser-induced plasma, the formation and propagation of an expanding shock/detonation wave, the generation of free radicals, the initiation of chemical reactions, and ultimately the initiation and propagation of global combustion. In this chapter, the ignition kernel spatial and temporal development is studied in Stoichiometric ammonia-oxygen gas mixtures by imaging the formation and propagation of the NH free radical.

It is known from previous studies and from the literature [21, 22, 24, 32, 33, 36] that there is a strong shockwave associated with the optical breakdown. This study probes the effects of this shockwave on the gas the breakdown region. The ignition kernel development and its transition into a propagating flame was tracked using shadowgraphs, as discussed in Chapter 4. In this chapter, PLIF imaging of free radicals is used to study the same events, and a correlation is established between the PLIF and shadowgraph images.

There are several choices as to which free radical to probe. Previous investigators have used primarily the OH radical [33, 41, 50], as it is a good indicator of combustion. The OH radical is also a reaction intermediate in the ammonia-oxygen flame. However, OH is a relatively long lived molecule with respect to the flame front whereas NH is a transient radical in the combustion process. Figure 5.1 illustrates this graphically with spatially resolved chemiluminescent OH and NH spectra from an ammonia-oxygen flame recorded above a slit burner. Notice that the NH emission intensity is confined to a region very near the flame front, whereas the OH emission intensity is significant well past the flame front. Use of the NH radical in the PLIF imaging therefore minimizes ambiguities about the location and thickness of the flame front.

5.2 Experiment

Excitation and imaging of fluorescence from NH in the flamefront requires the use of a secondary pulsed laser source with high pulse energy at an appropriate wavelength and an intensified, gated, two dimensional detector. Considering the spectral region to be probed, one obvious choice for the PLIF probe laser is a dye laser. As can be seen in Figs. 2.3 – 2.5, the NH band that is to be pumped lies in the spectral region around 336 nm. There are two main options that allow generation of 336 nm laser pulses. The first option is to use a red dye laser and a frequency doubler, and the second option is to use a less efficient dye laser that directly produces the 336 nm

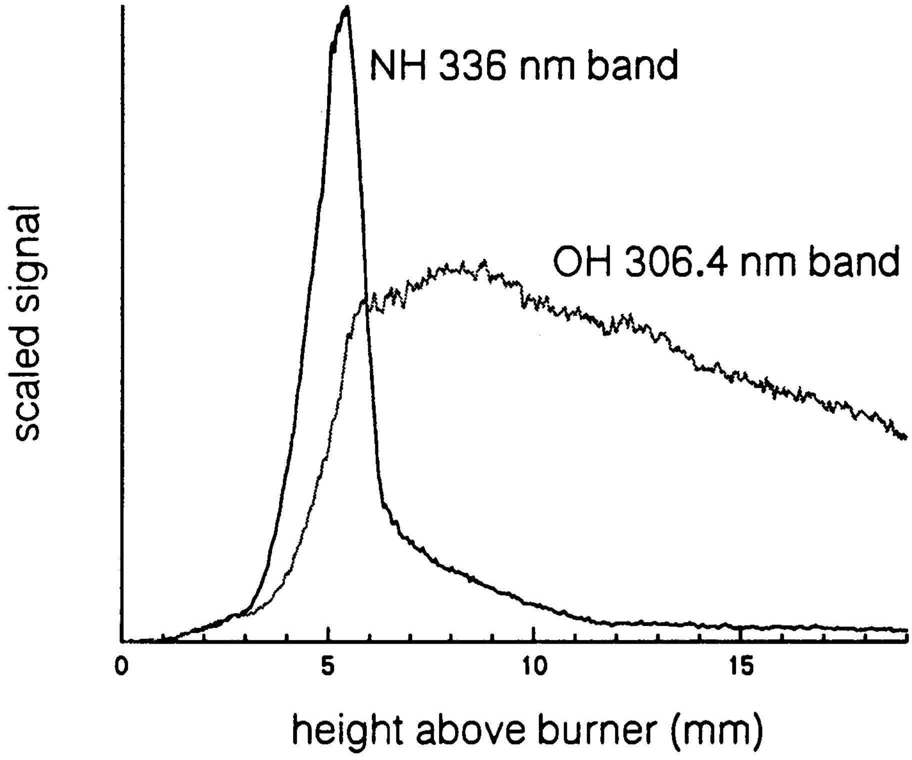

Figure 5.1: Experimentally measured NH and OH spontaneous emission signals above a slit burner.

output UV. Since the frequency doubled red dye laser pulse energies are comparable to the UV dye laser's direct output, the second option is more desirable experimentally, since a frequency doubling crystal is not required. The experimental layout is shown schematically in Fig. 5.2. The Coherent YG680S Nd:YAG laser used to generate the optical breakdown plasma is described in Chapter 2. The arrangement is the same as in the flame speed measurements discussed in Chapter 4 with the following additions. An additional laser is employed to induce the NH fluorescence and a two dimensional detection scheme is added to image the NH PLIF.

The PLIF probe laser is an excimer-pumped dye laser system consisting of a Lambda Physik EMG 150 MSC excimer laser, which has been filled with XeCl and produces 308 nm, 10 ns pulses with approximately 60 mJ per pulse, and a Lambda Physik FL3002E tunable dye laser. The oscillator and amplifier of the dye laser were filled with p-terphenyl dioxane solutions. The spectral line width of the dye laser is approximately 0.15 cm^{-1}. The maximum specified dye efficiency is given [51] as 8% at $\lambda \simeq 343$ nm for a 308 nm, 400 mJ per pulse pump laser. A LIF spectrum showing the NH 336 nm band in the spectral region around 340 nm is shown in Fig. 5.3, together with a measured dye laser tuning curve. The maximum LIF signal was obtained by pumping the strong Q-branch lines around 336 nm, even though the dye laser pulse energy was much lower in this spectral region. However, it was undesirable to pump in this region due to the proximity of the N_2 second positive system whose band head lies at 337 nm and is shaded toward the violet. As can be seen from Fig. 5.3, there is a trade-off between the strengths of the rotational lines and the dye laser pulse

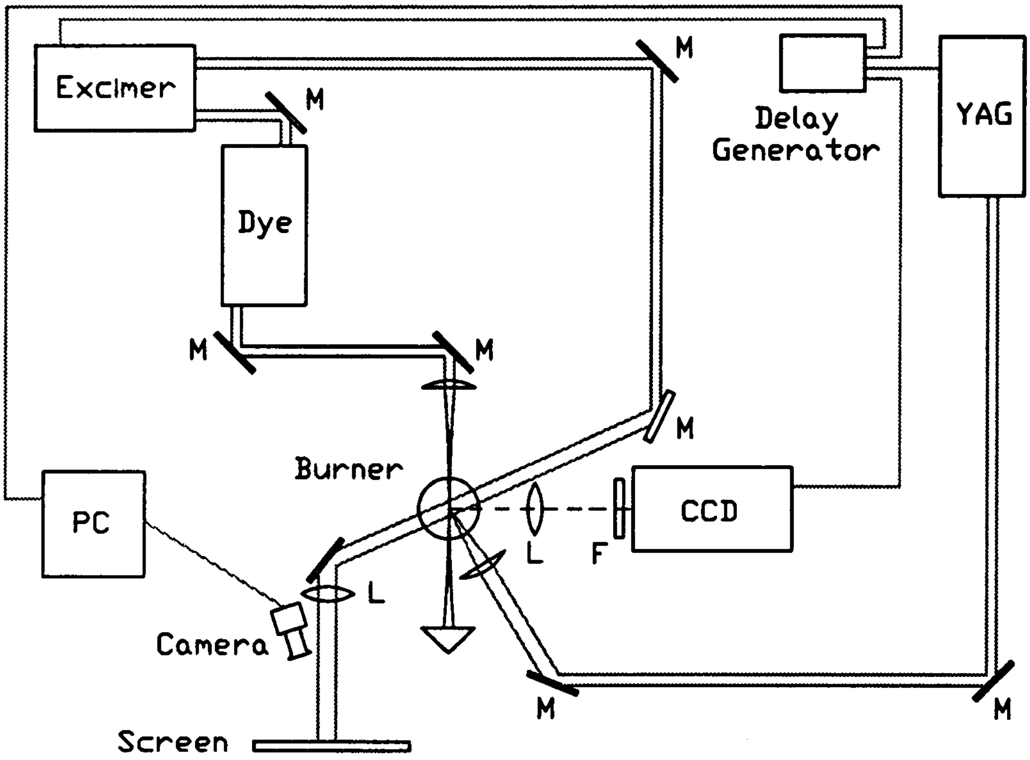

Figure 5.2: Schematic representation of the experimental layout. F = 337 ± 5.5 nm bandpass interference filter.

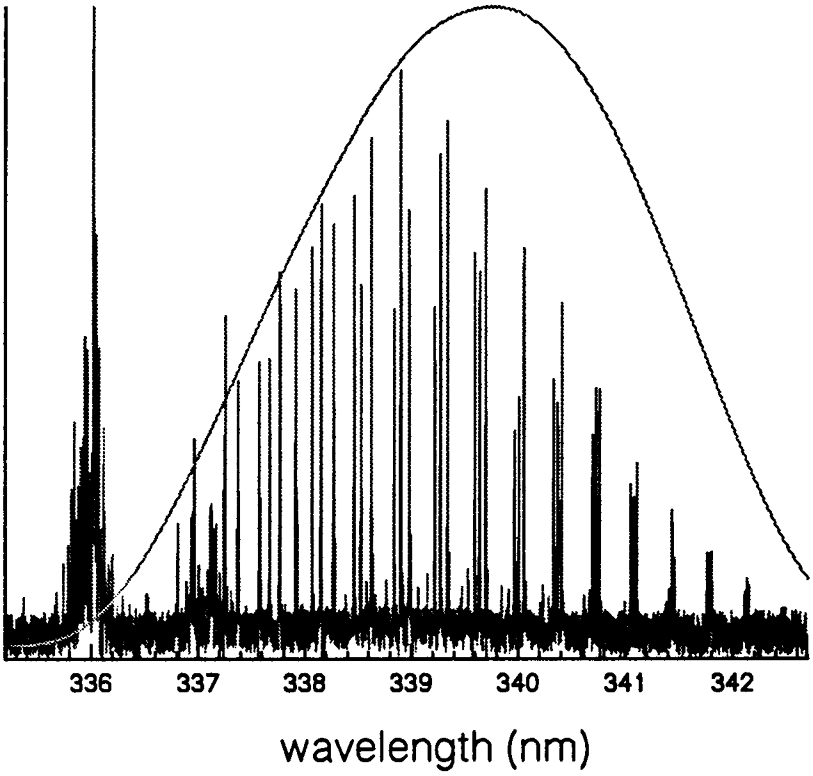

Figure 5.3: Experimental NH LIF spectrum and a scaled dye laser tuning curve.

energy. The rotational line that was chosen for subsequent measurements gave a compromise between maximum LIF signal and maximum pulse energy.

The excimer has two laser cavities or barrels, which may be operated in an oscillator-amplifier mode or as two independent oscillators. When in the two-oscillator mode the second cavity lases with a fixed time delay of 35 ns with respect to the first. In the experimental setup shown in Fig. 5.2, the first pulse (oscillator barrel) is used as the shadowgraph backlight and the second pulse (amplifier barrel) is used to pump the dye laser.

The dye laser output is shaped into a "sheet beam" by first directing it through a beam expander and subsequently through a cylindrical lens with a focal length of 30 cm. The f/# of the 30 cm cylindrical lens is approximately 30 and sufficiently large so that the thickness of the probe beam does not vary significantly over the small sample volume.

The detector used to image the PLIF is a CCD detector (EG&G, Model No. 1530) which is cryogenically cooled to reduce dark current and equipped with an intensifier (EG&G, Model No. LCI-7) to enhance the detection sensitivity. The detector is comprised of a 512 × 512 array of "pixels" with individual dimensions of 19 μm × 19 μm. The active area of the detector chip is therefore 9.7 mm × 9.7 mm. The lens-coupled intensifier also allows for gated detection with a minimum gate width of 5 ns.

The optical plasma is imaged onto the CCD array with a single lens. The position of the lens results in a image magnification of approximately 1.4. bandpass filter was placed in front of the detector to reject unwanted spectral regions. The filter is a nitrogen laser line filter (Oriel, Model No. 59930) centered at 337 nm with a 11 nm bandwidth (FWHM) and a peak transmittance of 24%. A transmission curve superimposed on a ammonia-oxygen flame emission spectrum is shown in Fig. 5.4. The flame emission spectrum was recorded over a slit-type flat-flame burner using an optical multichannel analyzer (EG&G PARC, Model No. 1460) and a linear diode array detector (EG&G, Model No. 1423). A rich fuel/air ratio was selected to make the NH and OH chemiluminescent signals in the reaction front comparable in magnitude. The laser line filter transmission curve was obtained from the manufacturer. Figure 5.4 shows that any contribution of OH spontaneous emission from the $\Delta\nu = 0$ sequence of the $A^2\Sigma^+ \rightarrow X^2\Pi_i$ UV system is almost totally eliminated.

The time delay of the dye laser relative to the optical breakdown pulse was controlled with the delay generator. A 1 μs pretrigger TTL pulse is output from the Nd:YAG laser each time it Q-switches. This TTL pulse was used to drive the other experimental equipment. The earliest attainable time delay of the dye laser relative to the YAG pulse using this synchronization scheme was approximately 300 ns. This delay was acceptable since the primary interests are events that happen at longer time delays.

The Nd:YAG laser, which drives the entire experimental sequence of events, was operated in single shot mode. When the fire button on the laser control panel is pressed the laser emits a single 4.5 ns pulse. The 1 μs pretrigger pulse triggers the delay generator, which sends out appropriately delayed trigger pulses to the excimer

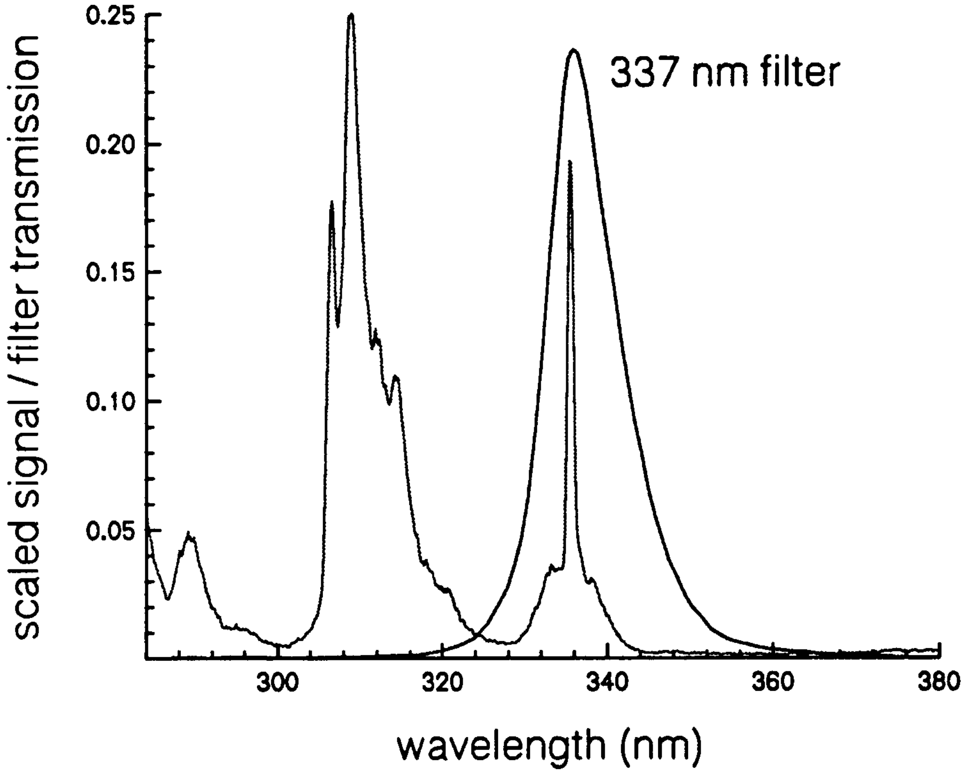

Figure 5.4: Spontaneous emission spectra measured in a ammonia-oxygen flame with the transmission curve of the 337 nm laser line filter superimposed.

laser, camera and CCD detector. The oscillator barrel output pulse from the excimer laser is directed as shown in Fig. 5.2 and passes through the optical breakdown plasma at an angle of 94° with respect to the optical axis of the Nd:YAG pulse. The resulting shadowgraph is imaged on the fluorescent screen and recorded onto the PC hard drive using the camera. The pulse from the excimer laser amplifier pumps the dye laser. The dye laser output traverses the beam shaping optics and is directed through the center of the optical breakdown plasma at an angle of 20° with respect to the Nd:YAG optical axis. The CCD captures PLIF images with a 100 ns gate, which overlaps the dye laser pulse. The 35 ns delay between the shadowgraph and PLIF pulses is insignificant for all time delays beyond the initial time delay of 300 ns when the signals are dominated by the plasma emission.

Data were acquired under two separate conditions. First in ammonia flowing through the burner at a rate of 4.4 l/min and second with a premixed stoichiometric ammonia-oxygen mixture flowing at a total rate of 7.6 l/min. In the first series of experiments, the relationships between NH spontaneous emission, shadowgraph and PLIF images are investigated. The optical breakdown in pure ammonia was very stable, i.e., repeatable from shot to shot. As a result, many laser shots could be averaged to increase the signal to noise ratio. Images were acquired from the earliest time delay of 300 ns out to a delay of 100 μs, for which the NH PLIF signals were no longer detectable. In the second series of experiments, the ammonia-oxygen mixture was ignited with each optical breakdown event. The data that were acquired in this case were single-shot images, and, since single shot plasma emission is only attainable for very short time delays, no plasma emission images were recorded. Shadowgraph and PLIF images were recorded from the earliest time delay until the resulting flame propagated beyond the edge of the CCD chip.

5.3 Data Analysis and Results

5.3.1 Pure Ammonia

Figures 5.5 through 5.8 show results of the shot averaged shadowgraph, PLIF and spontaneous emission images in pure ammonia. Figures 5.5 and 5.6 contain, from top to bottom, 10-shot-averaged shadowgraph images, 100-shot-averaged PLIF images and 100-shot-averaged spontaneous emission images at each indicated time delay. Figures 5.7 and 5.8 show only shadowgraph images (on the top) and PLIF (on the bottom) at each time delay as the spontaneous emission signals were either very weak or undetectable (for time delays greater than 10 μs) using our detection scheme. Only the first 50 μs is shown here. Shadowgraph and PLIF images were recorded out to 100 μs. The NH PLIF spatial profiles from 50 to 100 μs were essentially the same as the 50 μs profile but the intensities were greatly diminished. NH PLIF was not detectable for time delays greater than 100 μs.

From these images one can see that

1. The spontaneous emission that results from N + H recombination is confined to a small region about the focal volume of the Nd:YAG optical breakdown pulses for all time delays, and decays after $\sim$ 10 μs.

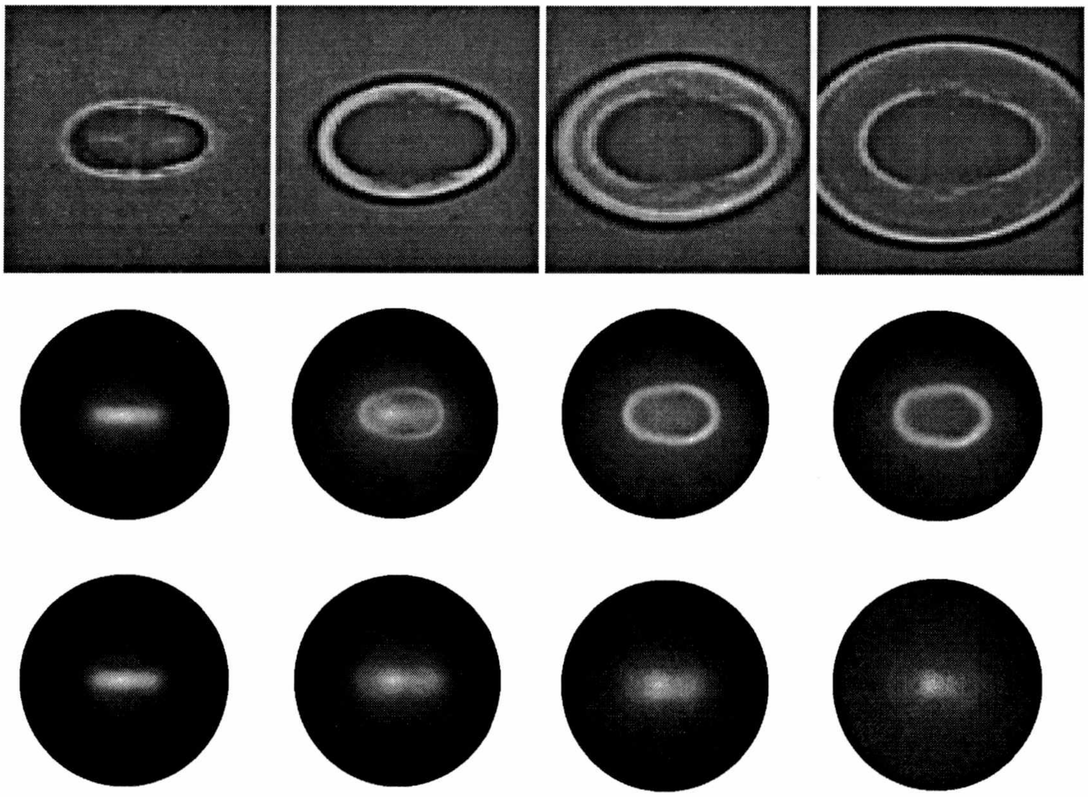

Figure 5.5: Shadowgraph (top) PLIF (middle) and spontaneous (bottom) images of LIB plasmas in pure ammonia. The columns represent time delays of .3, 1.3, 2.3 and 3.3 μs from left to right.

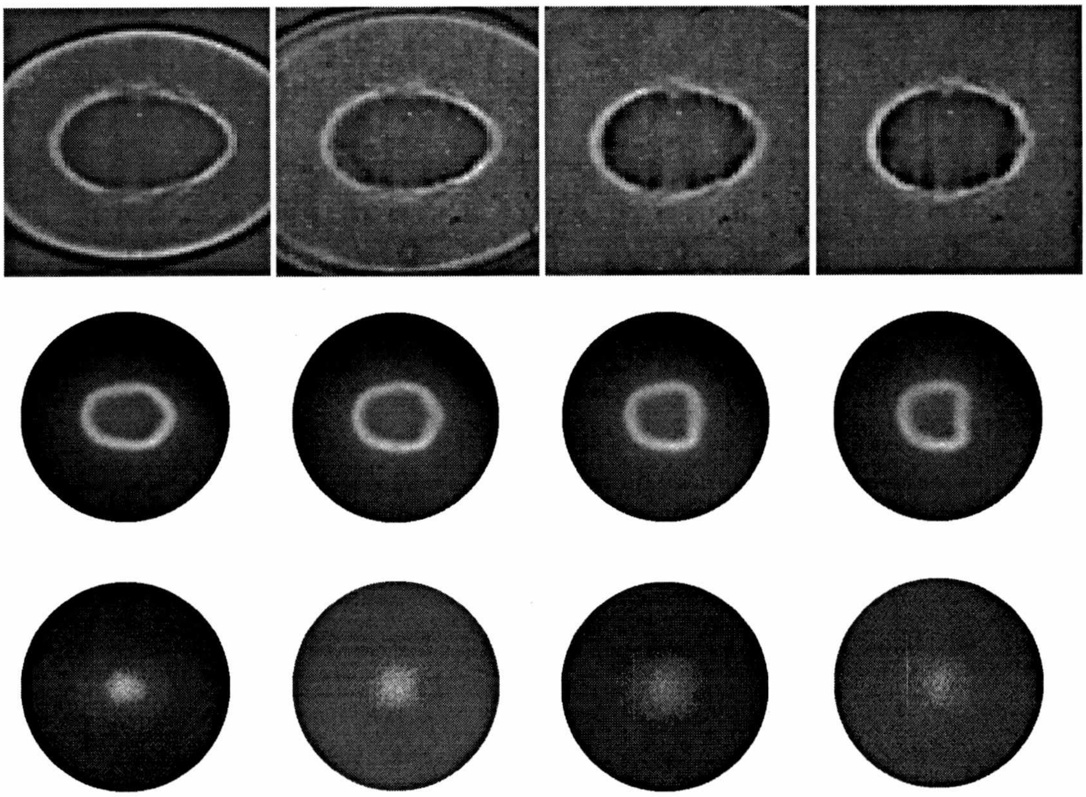

Figure 5.6: Shadowgraph (top) PLIF (middle) and spontaneous (bottom) images of LIB plasmas in pure ammonia. The columns represent time delays of 4.3, 5.3, 6.3 and 7.3 μs from left to right.

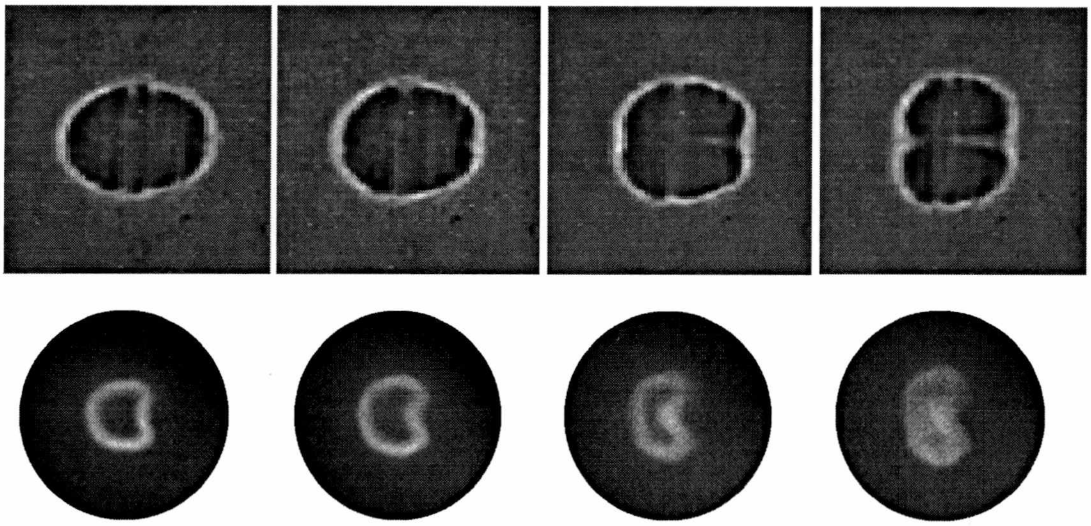

Figure 5.7: Shadowgraph (top) PLIF (bottom) images of LIB plasmas in pure ammonia. The columns represent time delays of 8.3, 10.3, 15.3 and 20.3 μs from left to right.

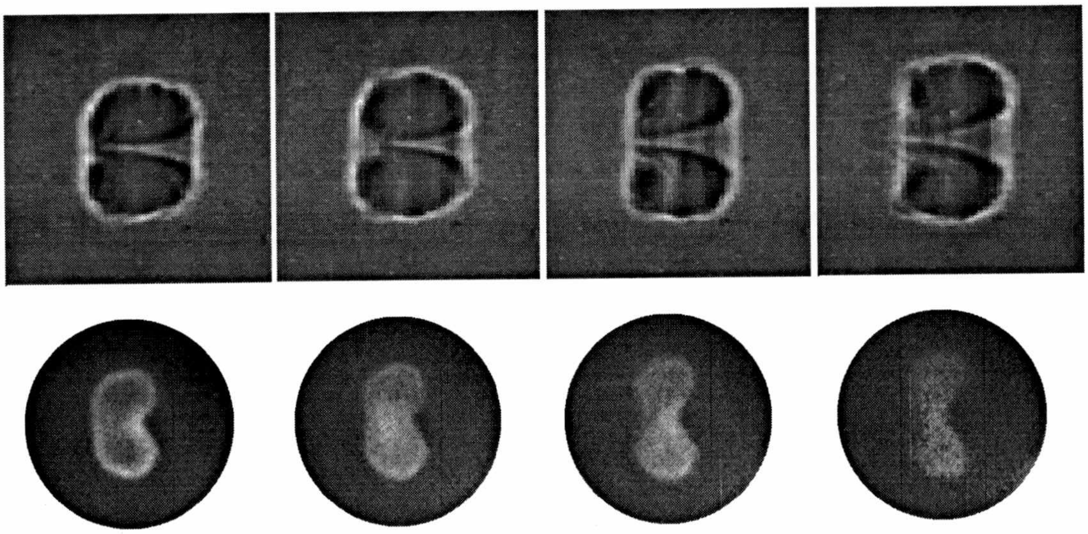

Figure 5.8: Shadowgraph (top) PLIF (bottom) images of LIB plasmas in pure ammonia. The columns represent time delays of 25.3, 30.3, 40.3 and 50.3 μs from left to right.

2. A ring of ground state NH is seen to form around the spontaneous emission region at approximately 1 μs delay and then propagate outward. At first this ring closely follows the shockwave and is always confined to the higher temperature region, which appears dark in the shadowgraphs.

3. As the hot region relaxes, the NH ring tends to separate along the Nd:YAG optical axis and forms a torus whose symmetry axis is the Nd:YAG optical axis. The beginning stages of this gas dynamic effect is apparent earlier in the PLIF images than in the shadowgraph images, but is clearly present in both at the longer time delays.

Figure 5.9 shows the results of adding the NH PLIF and spontaneous emission signals over the entire CCD chip at each time delay. Figure 5.9(a) shows the integrated signals over all measured time delays, and Fig. 5.9(b) is scaled to bring out details for time delays greater than 1 μs. As can be seen in this figure the spontaneous emission signal decays steadily to zero in ~ 10 μs. The PLIF signals indicate the presence of at least two minima as the signal approaches zero at 100 μs. One might explain these minima in terms of the mechanisms that produce ground state NH molecules. There are three primary processes that may produce ground state NH in the optical discharge. For early times in the plasma formation and decay, the gas near the focal volume of the breakdown pulse is highly dissociated and ionized. Therefore, one sees very bright spontaneous emission as excited state recombination NH molecules decay to the ground state. It can be seen from the shadowgraphs that there is a shockwave produced by the optical discharge. This shockwave is strong enough to significantly

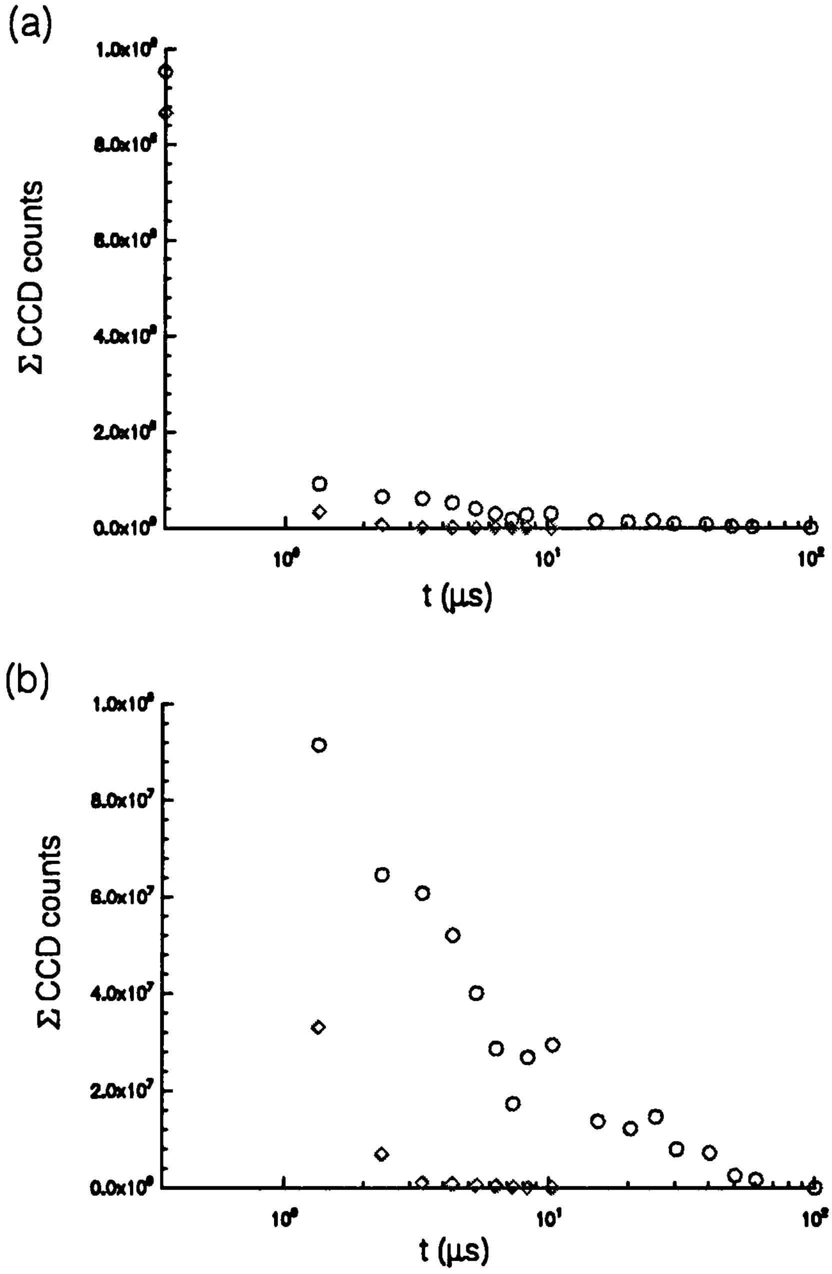

Figure 5.9: Total NH spontaneous emission (◇) and LIF (○) signals obtained in pure ammonia.

heat the air in the gas region near the focal volume of the breakdown pulse and adjacent to the spontaneous emission region. This shockwave heating is possibly sufficient to cause dissociation of the ammonia and yield ground state NH molecules. At later time delays the signal increase is possibly due to an increase in NH production due to ammonia chemical reactions with other molecules as the hot gas relaxes to chemical equilibrium.

5.3.2 Single Shot Comparisons between Pure Ammonia and Stoichiometric Ammonia-Oxygen

Figures 5.10 through 5.13 show the single-shot shadowgraph and PLIF images obtained in pure ammonia and stoichiometric ammonia-oxygen. The top two rows of images in each of these figures were obtained in pure ammonia and the bottom two rows were obtained in the ammonia-oxygen mixture. Figure 5.14 shows shadowgraph and PLIF images obtained in ammonia-oxygen only.

The PLIF and shadowgraph images are essentially the same for both gases out to time delays of approximately 5 μs. At this point the combustible ammonia-oxygen mixture clearly shows signs of kernel growth, first in the PLIF images and then in the shadowgraph images, whereas the images for the pure ammonia begin to indicate relaxation. By 30 μs the NH torus is barely detectable in pure ammonia while the kernel in the ammonia-oxygen mixture continues to grow. Figure 5.14 shows the development of the ignition kernel into a propagating flame. Note how the toroidal shape of the ignition kernel is preserved as the flame propagates in time. The gaseous region near the optical path of the Nd:YAG laser pulse does not appear to burn

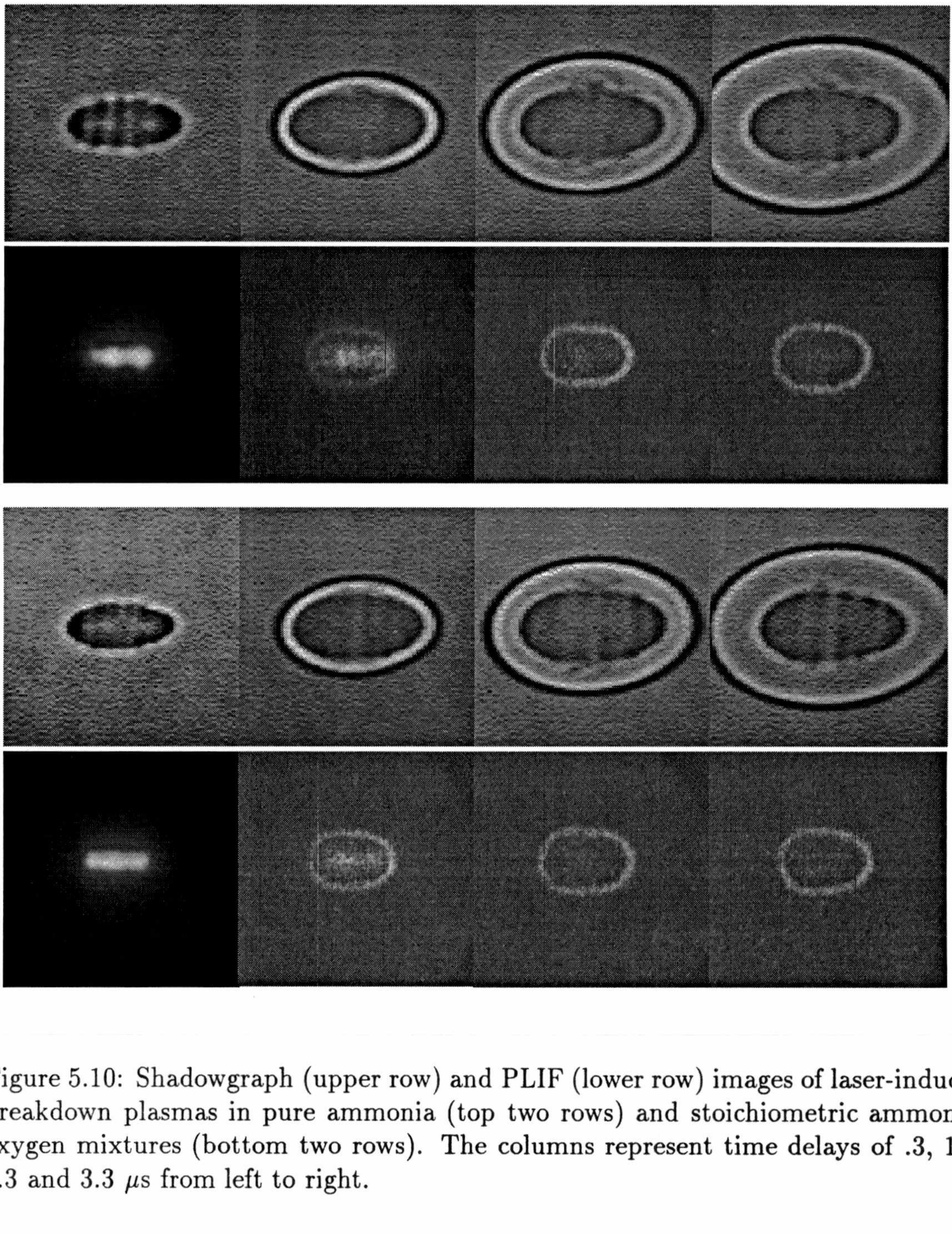

Figure 5.10: Shadowgraph (upper row) and PLIF (lower row) images of laser-induced breakdown plasmas in pure ammonia (top two rows) and stoichiometric ammonia-oxygen mixtures (bottom two rows). The columns represent time delays of .3, 1.3, 2.3 and 3.3 μs from left to right.

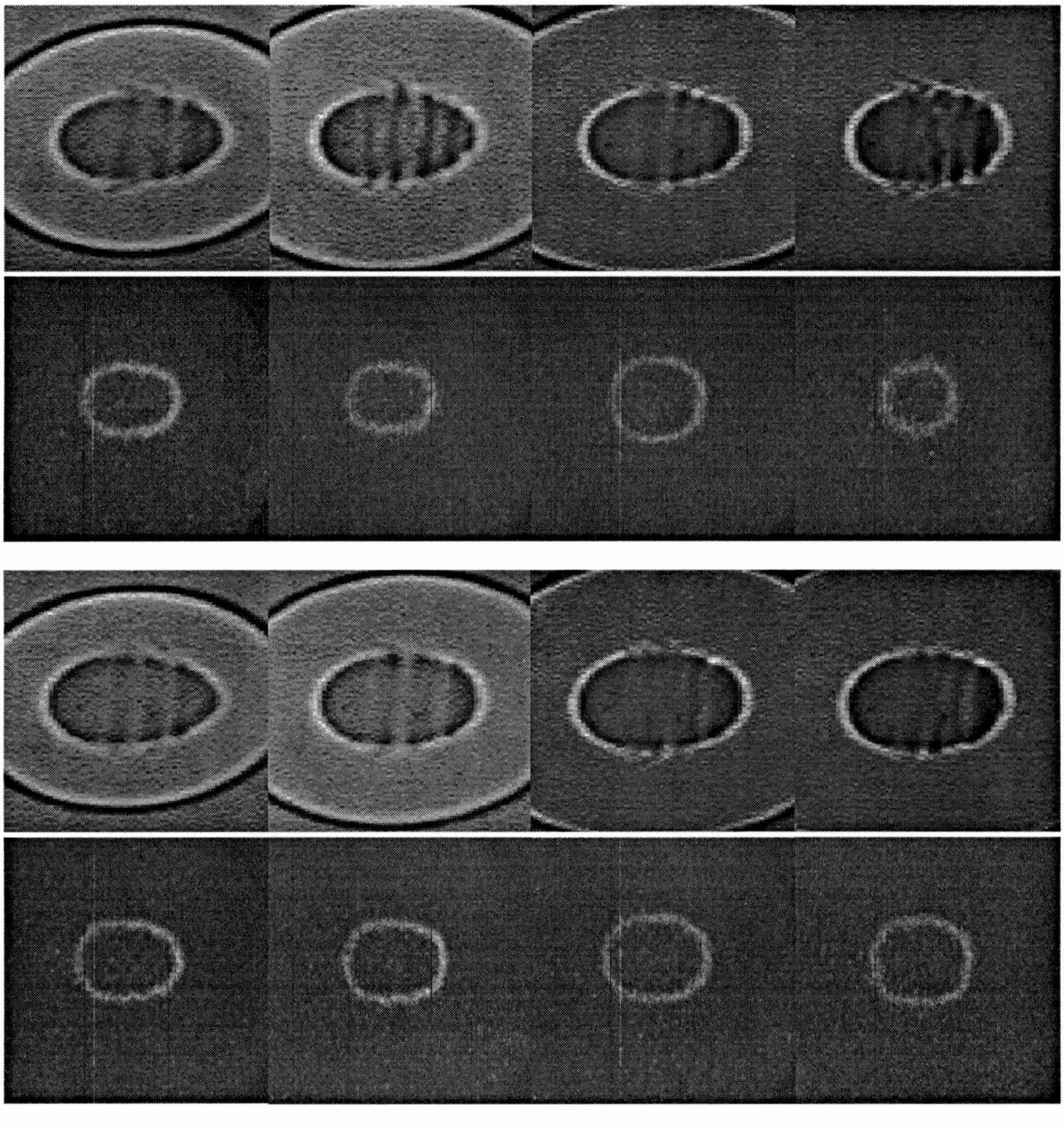

Figure 5.11: Shadowgraph (upper row) and PLIF (lower row) images of laser-induced breakdown plasmas in pure ammonia (top two rows) and stoichiometric ammonia-oxygen mixtures (bottom two rows). The columns represent time delays of 4.3, 5.3, 6.3 and 7.3 μs from left to right.

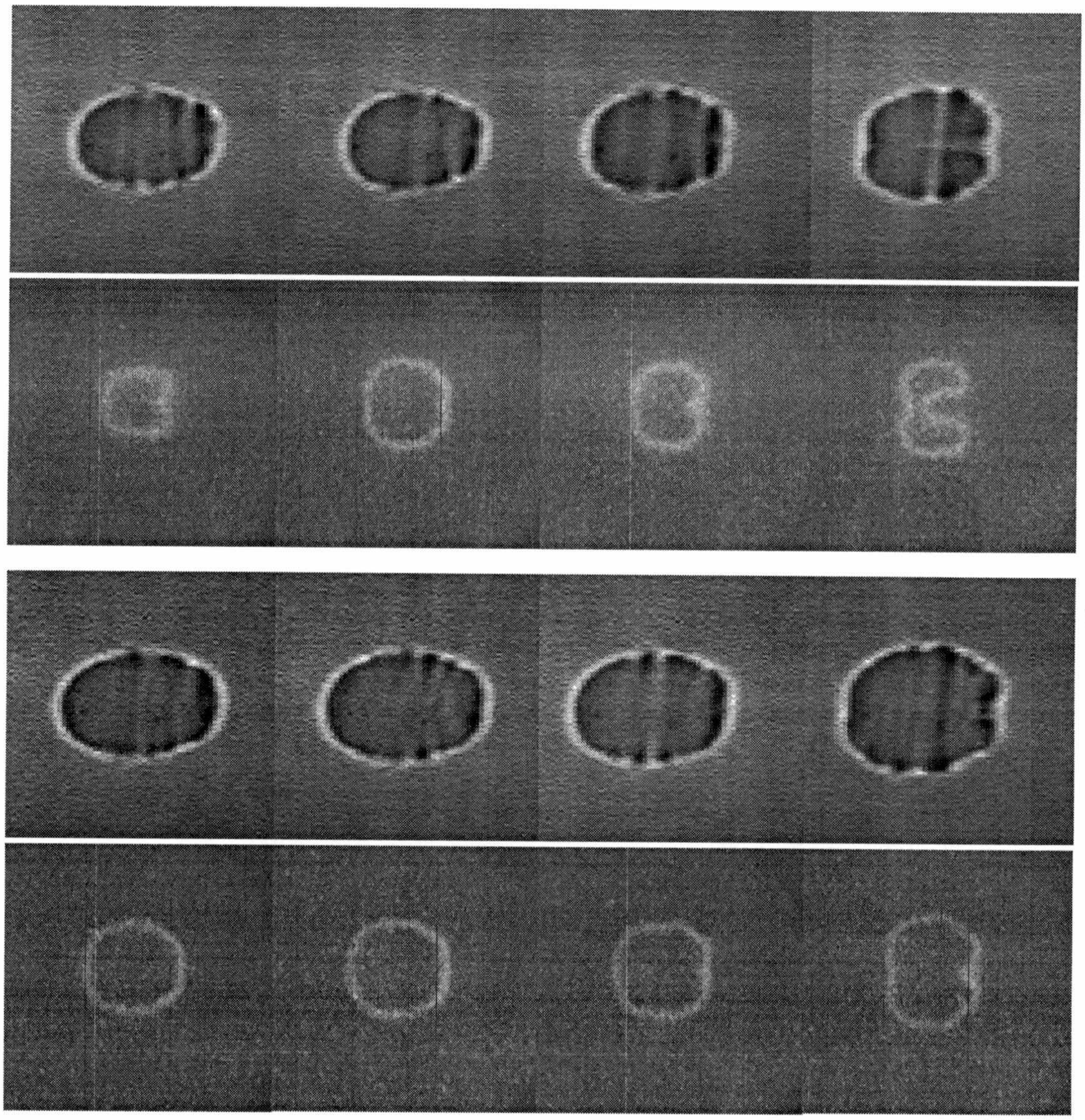

Figure 5.12: Shadowgraph (upper row) and PLIF (lower row) images of laser-induced breakdown plasmas in pure ammonia (top two rows) and stoichiometric ammonia-oxygen mixtures (bottom two rows). The columns represent time delays of 8.3, 9.3, 10.3 and 15.3 μs from left to right.

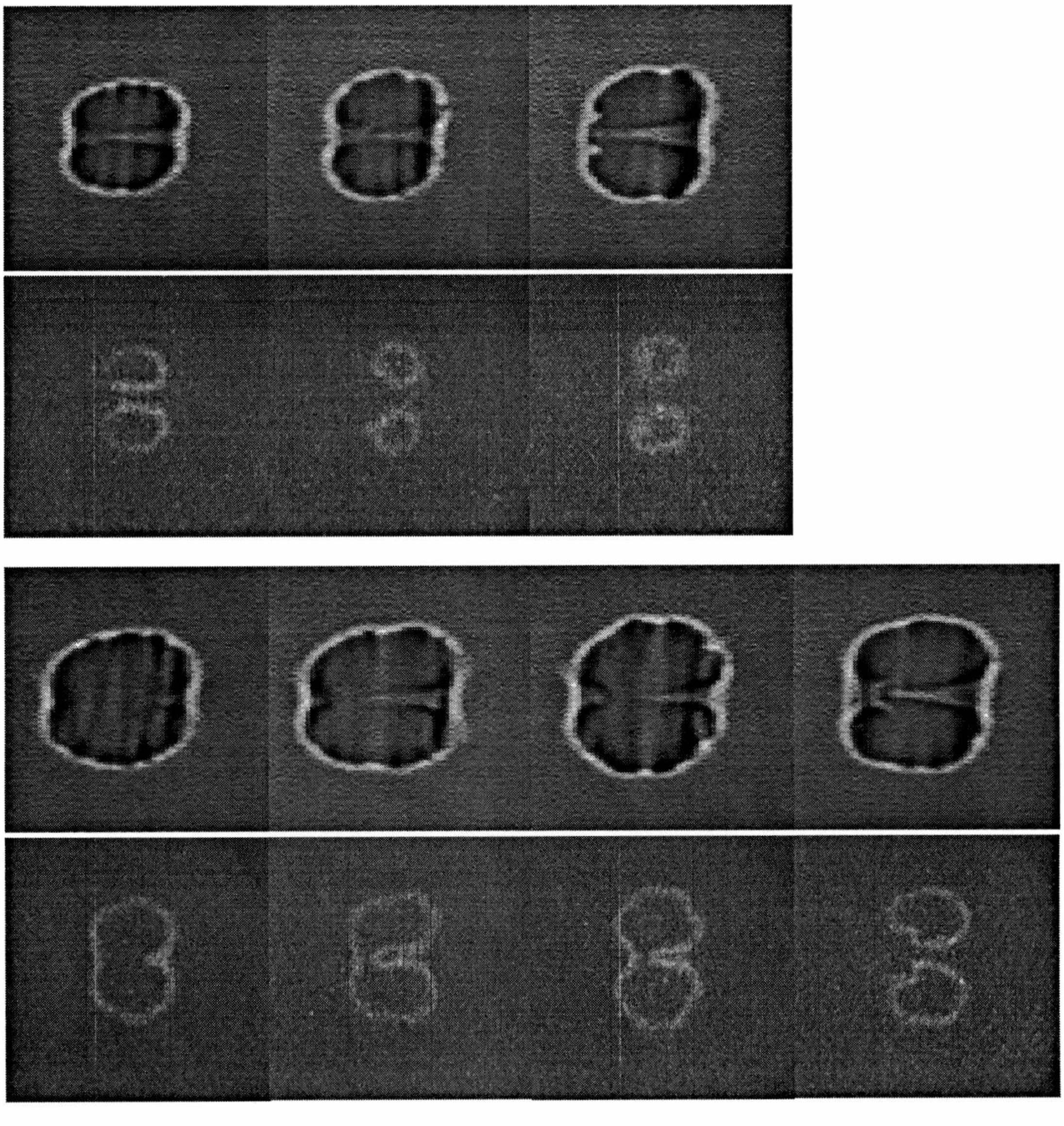

Figure 5.13: Shadowgraph (upper row) and PLIF (lower row) images of laser-induced breakdown plasmas in pure ammonia (top two rows) and stoichiometric ammonia-oxygen mixtures (bottom two rows). The columns represent time delays of 20.3, 25.3, 30.3 and 40.3 μs from left to right.

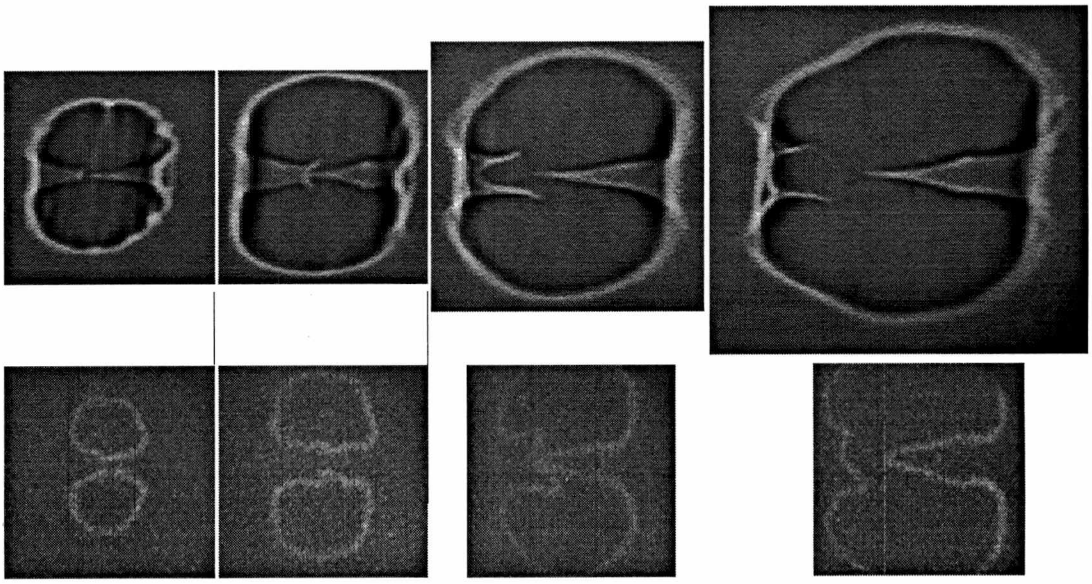

Figure 5.14: Shadowgraph (upper row) and PLIF (lower row) images of laser-induced breakdown plasmas in stoichiometric ammonia-oxygen mixtures. The columns represent time delays of 50.3, 100.3, 150.3 and 200.3 μs from left to right.

until relatively late in the flame development. This is most likely due to ambient gas flowing into the kernel along the optical axis and will be discussed in more detail in Section 5.3.4.

The propagating ring of NH observed in the ammonia-oxygen PLIF images is easily understood in terms of a propagating flame front. Figure 5.15 shows theoretical results for a freely propagating flame in stoichiometric ammonia-oxygen at atmospheric pressure. The calculation was performed using a one dimensional flame code written by Kee *et al.* [4]. Shown in this figure are the mass density and NH mole fraction profiles across the flame front. One can easily see from this result, considering the symmetry of the measured flame kernels, that a thin region of NH molecules near the flame front is expected. Comparison of Fig. 5.15 with the shadowgraph and PLIF images also elucidates the observed distance between the flame kernel boundary measured in the shadowgraphs and the NH PLIF ring. The shadowgraph is a measure of the density gradient in the gas. Figure 5.15 clearly shows that the density gradient occurs well in front of NH production in the freely propagating one dimensional flame.

5.3.3 Ignition Delay

Figure 5.16 shows the total measured NH LIF and spontaneous emission signals at each time delay for both the pure ammonia and the combustible ammonia-oxygen mixtures. Figure 5.16(a) shows the integrated signals over all measured time delays, and Fig. 5.16(b) is scaled to bring out details for time delays greater than 1 μs. As in the shot averaged total signals, early time delays ($t < 1\mu$s) are dominated by spontaneous emission. At a delay of about 10 μs, the ammonia-oxygen mixture total

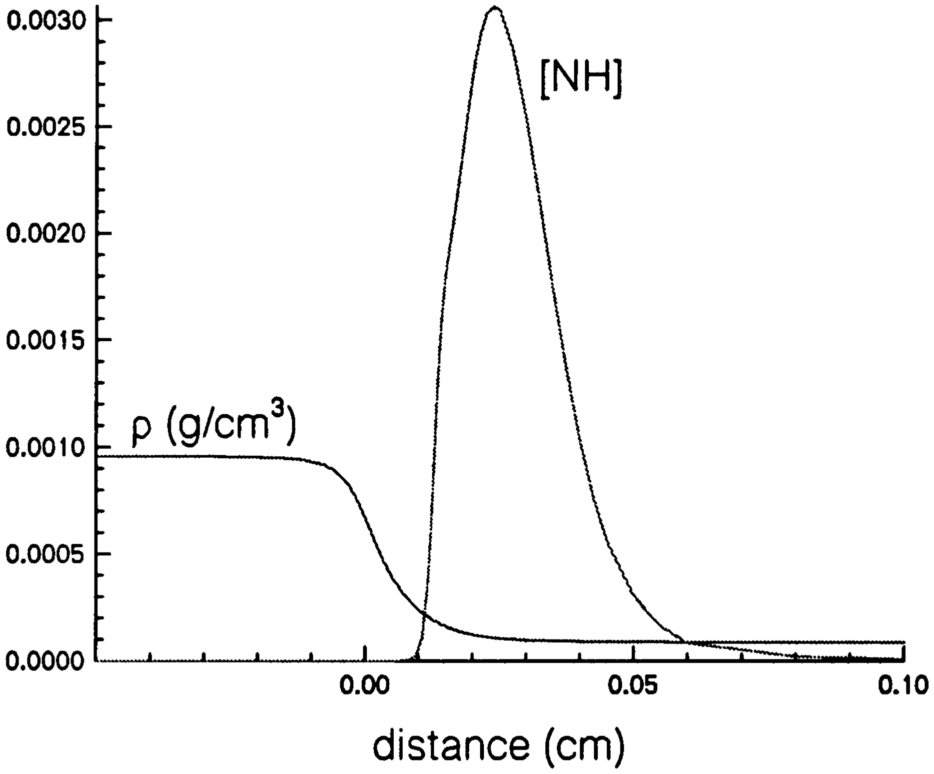

Figure 5.15: Theoretical mass density and NH mole fraction for a freely propagating stoichiometric ammonia-oxygen flame.

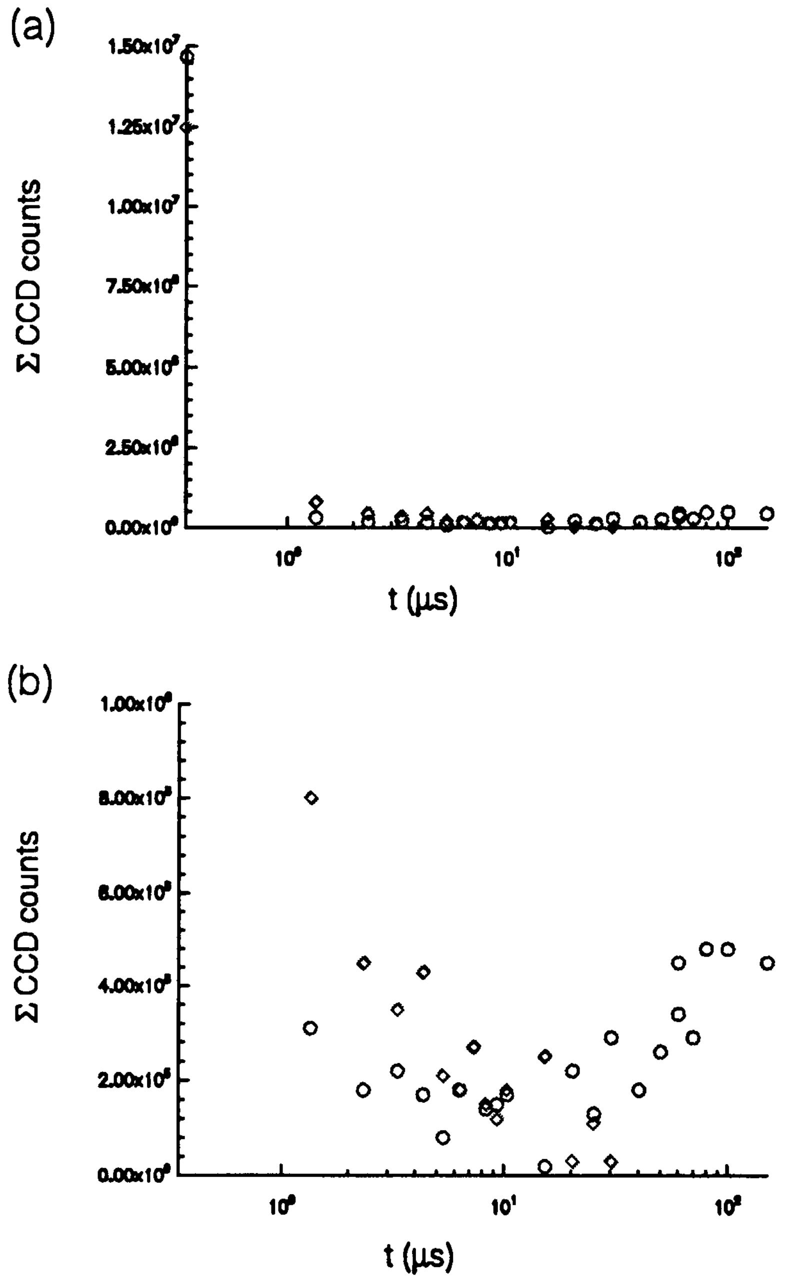

Figure 5.16: Total single-shot LIF signals in pure ammonia (◇) and stoichiometric (○) ammonia-oxygen mixtures.

LIF signal reaches a minimum and begins to increase, whereas the total signal in pure ammonia continues to monotonically decay. The point where the ammonia-oxygen mixture total NH signal begins to increase, or certainly where this signal crosses the pure ammonia signal, can be interpreted as an ignition delay. Close inspection of the pure ammonia and ammonia-oxygen PLIF and shadowgraph images reveals differences in the size and shape of the ignition kernel as early as 4 to 5 μs. This too appears to indicate the beginning stages of combustion.

The thin ring of ground state NH that is produced near the flame front in ammonia-oxygen flames makes the inference of ignition delay using total NH signal difficult. More appropriate species for this measurement would be, for example, OH, NO or even N_2, as diatomic nitrogen is a combustion product of the ammonia-oxygen reaction. This reasoning is graphically illustrated in Fig. 5.17. This figure shows the mole fractions of the combustion products of several reaction intermediates for a stoichiometric freely propagating flame, calculated using the one dimensional flame code of Kee *el al.)* [4]. As can be seen from the figure, there are several species which are both longer lived and present in higher quantities that would result in a stronger LIF signal over larger areas. It is recommended to use an alternate species, such as OH, NO, or N_2, to infer ignition delays.

5.3.4 Kernel Dynamics

Formation of the toroidal shaped ignition kernel is characteristic of both electrical-spark [52, 53, 54, 55, 56] and laser-spark [33, 41] ignition and appears to be a direct consequence of the spatial distribution of the nascent plasma. Kono *et al.* [52]

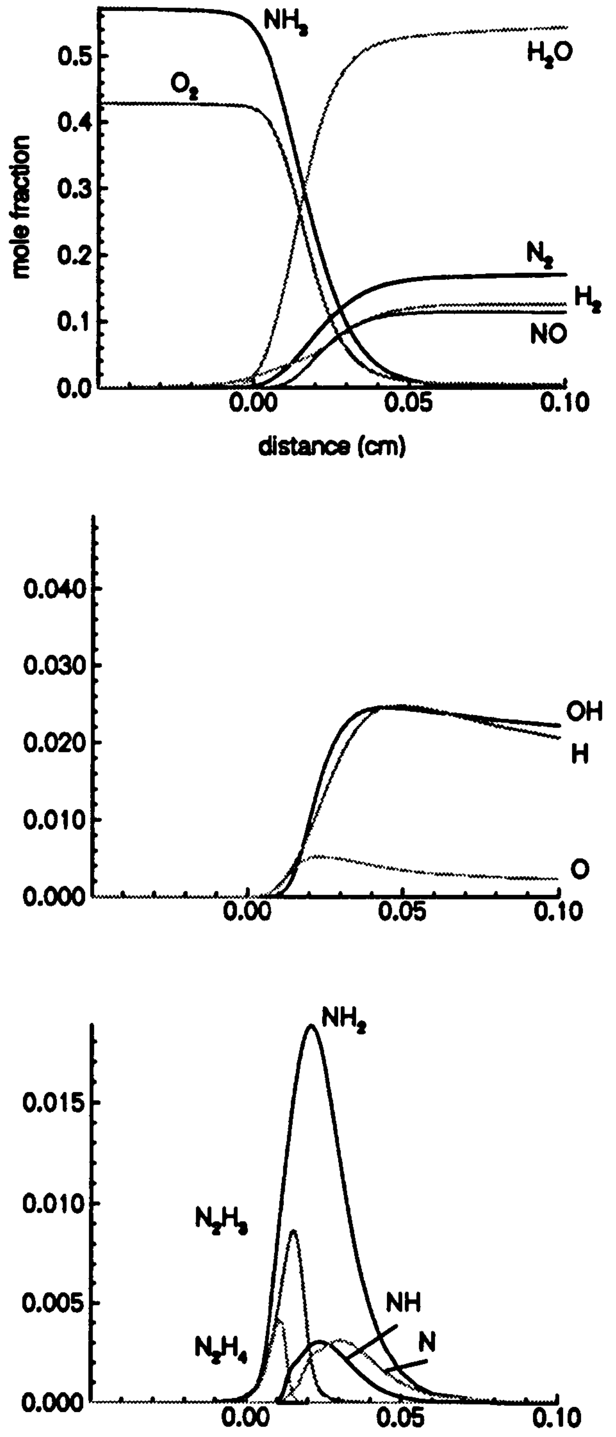

Figure 5.17: Theoretical flame front mole fractions for selected species in a freely propagating stoichiometric ammonia-oxygen flame.

have shown in a computer simulation, which models instantaneous electrical-spark ignition, that the shockwave which propagates outward from the initial plasma causes an overexpansion of the gas along the spark channel. This overexpansion causes ambient gas to flow into the kernel along the electrode axis creating the toroidal shape of the kernel. The shadowgraph and PLIF images of laser-spark ignition agree with this scenario. The time sequence images clearly show the influx of gas. The delay of the ignition and combustion of the gas along the optical axis supports the hypothesis that the gas is indeed drawn in from the surrounding area, as opposed to being chemically altered by the laser pulse. Note, however, that the gas influx is asymmetric. That is, the inward flow is more prominent on the back side (away form the Nd:YAG laser) of the kernel. It is this asymmetrical gas influx that results in the backstreaming observed in the results of Chapter 4.

A likely cause of asymmetrical gas flow into the kernel is laser pulse heating of the gas immediately in front (on the Nd:YAG side) of the optical breakdown region. In this region, the laser pulse intensity is only slightly below the breakdown threshold of the gas and the laser pulse very probably heats the gas within the converging optical cone. As the pulse propagates nearer to the focal spot and optical breakdown is achieved, the laser pulse energy is very efficiently absorbed by the plasma. A significant portion of the laser pulse energy is thus removed from the pulse before it can propagate through the region of gas immediately behind the plasma region. For the pulse energies and pulse widths studied here, only the portion of the laser pulse that traverses the focal spot before the breakdown threshold is achieved is transmitted by the plasma, while the rest of the pulse is absorbed by the plasma. Preheated gas would be less dense and therefore inward flow would carry less momentum from the forward side of the kernel than from the rear side of the kernel. Preheated gas would also be easier to ignite.

It has been suggested [33] that there may be a residual velocity component in the kernel from the initial formation of the optical plasma, which may contribute to the observed backstreaming. This velocity component develops as a result of the directionality of the laser pulse. As the laser propagates into a focal region where the intensity is sufficient to cause ionization of the gas molecules, an optical plasma is created and it begins to expand very rapidly through the process of inverse bremsstrahlung. The optically thick plasma is exposed to the strong optical field on its forward side and absorbs the radiation before it can propagate to the back side of the plasma. As a result, the plasma expands very rapidly back toward the laser [57, 58] at a velocity of approximately 10^7 cm/s. It is doubtful, however, whether a significant effect remains at the comparatively long time delays for which backstreaming is observed. The shadowgraph and PLIF images do not reveal any evidence of a sustained axial velocity component caused by the initial formation of the optical plasma other than the asymmetrical gas influx and backstreaming. Previous spatially resolved studies of laser-induced breakdown in hydrogen gas [27] show that this so called plasma wave is very rapidly damped. In this case, movement of the plasma was not observed for time delays after a few hundred nanoseconds.

Spiglanin *et al.* [33] noted that in hydrogen-oxygen-argon mixtures the backstreaming of the ignition kernel was only observed for laser shots for which ignition was achieved. We have observed this effect in fuel rich ammonia-oxygen mixtures, propane-air mixtures and in nonflammable gases such as pure ammonia and air. This backstreaming effect appears in our experiments to be dependant on the laser pulse energy absorbed by the plasma and, in flammable gases, on the ignition delay and flame speed.

In nonflammable gases one sees the development of the torus in shadowgraph sequences and the backward propagation in the relaxation of the laser-spark heated gas. The beginning stages of the backstreaming can be seen in the later shadowgraph images in pure ammonia in Fig. 5.8. For larger absorbed energies the backstreaming is more pronounced.

The reason backstreaming was not observed in the ammonia-oxygen images in this chapter and in Chapter 4 for $\phi < 1.6$ is probably due to the ignition delays and flame speeds of the various ammonia-oxygen mixtures. Figure 5.14 shows indications of the backstreaming in both the PLIF and shadowgraph images. However, the flame speed is fast enough so that the backstreaming velocity does not overtake the boundary of the kernel. From Fig. 4.4, it can be seen that the ignition delay for the $\phi = 1.8$ mixture is several hundred microseconds longer than the $\phi = 0.3$ mixture, based on the size of the ignition kernels. This longer ignition delay allows the kernel dynamics to develop the backstreaming component before the flame front is established. Once the combustion begins to occur, the kernel retains its initial shape, as can be seen in Fig. 4.7.

Thus, one can conclude that the backstreaming kernel results from a combination of laser-induced gas dynamic effects. Asymmetric laser heating of the gas outside the kernel and shockwave induced ambient gas influx combine to cause the ignition kernel to stream back toward the laser. The fact that backstreaming is more pronounced for higher pulse energies suggests that preheating is a major factor in inducing this phenomena.

The shadowgraph images in Figs. 5.5–5.8 and Figs. 5.10–5.13 consistently exhibit a vertical interference pattern. If this interference pattern is attributed to a grating, then one can infer from these images that there is a grating spacing on the order of 2 μm along the optical axis in the ignition kernel for time delays less than 20 μs, using the relation $m\lambda = a \sin \theta$. It is possible that this grating is attributable to the gas dynamics that occur during the initial stages of the LIB plasma.

When the laser pulse is focused into the gas, there are actually several cites along the optical axis within the focal volume where breakdown is initiated. A violent shockwave is generated at each of the breakdown cites. These shockwave collide and coalesce to form the elliptical shockwave that is observed in the first few microseconds of the kernel formation. A very marked vertical structure, resulting from the collisions of the shock waves, has been observed in early time delay ($t \leq 300$ ns) shadowgraph studies [3]. The shockwaves at very early time delays ($t \leq 100$ ns) propagate at speeds that are several times the speed of sound and it is expected that the collisions of these shockwaves result in significant density variations within the optical breakdown plasma. Thus, it is reasonable to attribute the interference structure observed in the shadowgraph images to density variations on the order of 2 μm within the optical plasma.

Chapter 6

Summary

This dissertation has dealt with several different aspects of 1.064 μm pulsed laser-induced plasmas in ammonia and ammonia-oxygen gaseous mixtures. We have primarily used the experimental techniques of spontaneous emission spectroscopy, shadowgraph imaging, and planar laser-induced fluorescence (PLIF) imaging to probe optical plasmas, laser-spark ignition, ignition kernel temporal and spatial development, and flame propagation speeds.

As mentioned in Chapter 1, one approach to laser-spark ignition modeling is to use experimentally determined initial conditions acquired at some point in the kernel development [23]. Such an approach could be used to circumvent difficulties with modeling the radiation transport and blastwave dynamics in the early stages of ignition kernel development. However, in light of the non-one-dimensional nature of the kernel dynamics, this approach would require large quantities of experimental data to establish the initial conditions for each calculation.

In Chapter 2, it was demonstrated that multispecies spontaneous emission spectroscopy can be used to measure and spatially resolve temperatures within a laser-spark ignition kernel. Multispecies fits to spontaneous emission spectra can be used to infer relative number densities only if we can ensure that the excited molecules are in thermodynamic equilibrium with their ground states. These techniques can readily be used to verify theoretical predictions in model development of laser spark ignition.

In Chapter 3, minimum ignition energies were measured over the flammability limits of atmospheric pressure ammonia-oxygen mixtures. We found that the ignition threshold lies below the breakdown threshold for fuel equivalence ratios around $\phi = 1$. Further investigations in this region with 1.064 μm radiation will require laser pulse widths in the picosecond range, since the energy absorbed by the plasma from the nanosecond laser pulses is larger than the minimum ignition energy. The minimum ignition energy values obtained in this chapter can be compared to theoretical predictions and to other ignition modes when data becomes available.

In Chapter 4, it was shown that the laminar burning velocity calculated using the CHEMKIN code together with the reaction mechanism in Appendix B agrees reasonably well with the experimentally determined flame speeds from the quasi-spherical diverging flame kernels. It was observed that the approximately spherical structure of the flame kernel is destroyed for fuel equivalence ratios of 1.6 or higher for the laser parameters in this study. For such fuel equivalence ratios, the gas dynamic effects in the kernel caused the flame front to propagate back toward the laser.

Existing models of laser-spark ignition have been consistently one dimensional and are usually based on the Taylor blast-wave solution [21, 32, 33, 36]. While such models can be used to elucidate real gas and chemical kinetic effects on the kernel development, they ignore the important two dimensional gas dynamic effects discussed in Chapter 5.

Two dimensional axially symmetric ignition models based on numerical solutions of the conservations equations have been developed for electrical sparks [52, 59]. A recent effort by Kravchik and Sher [59] is a two dimensional model of electrical spark ignition which includes radiation transport, chemical kinetic and gas dynamic effects. Such a model could be adapted to laser spark ignition with only minor modifications to the source and loss terms. The discussion on the kernel dynamics in Chapter 5 clearly demonstrates the necessity of a multi-dimensional model.

Experimental investigations that spatially and temporally resolve the gas temperature across the ignition kernel are currently being pursued. The hostile environment of the optical plasma and ignition kernel require remote access methods to quantify physical characteristics. Laser probe methods are well suited for such investigations. There are several laser diagnostic techniques that could be used to spatially resolve gas temperatures and species number densities. Experimentally, the more expeditious methods are the incoherent laser scattering processes, such as saturated laser-induced fluorescence (LIF), spontaneous Raman scattering, and collisionless LIF using picosecond or femtosecond laser pulses. These laser probe methods may be used in conjunction with a sheet probe beam to infer spatially resolved temperatures and number densities. Coherent process such as stimulated Raman scattering and four-wave mixing could also be applied to the optical plasma and ignition kernel, but would make the use of a sheet probe beam much more difficult.

Bibliography

Bibliography

[1] G. M. Weyl. Physics of laser-induced breakdown: an update. In L. J. Radziemski and D. A. Cremers, editors, *Laser-induced plasmas and applications.* Marcel Dekker, Inc., New York, 1989.

[2] G. I. Taylor. "The formation of a blast wave by a very intense explosion. II. The atomic explosion of 1945". *Proc. R. Soc. London Ser. A*, 201:175–186, 1950.

[3] C. Parigger and J. W. L. Lewis. Unpublished Report.

[4] R. J. Kee, J. F. Grcar, M. D. Smooke, and J. A. Miller. "A FORTRAN program for modeling steady one dimensional flames". Technical Report SAND85-8240, Sandia National Laboratories, 1985.

[5] J. O. Hornkohl, C. Parigger, and J. W. L. Lewis. "On the use of line strengths in applied diatomic spectroscopy". Submitted to Optical Society of America for presentation in the 1995 conference on Laser Applications to Chemical and Environmental Analysis, March 1996.

[6] J. O. Hornkohl, C. Parigger, and J. W. L. Lewis. "Computation of synthetic diatomic spectra". In *Laser Applications to Chemical Analysis, 1994 Technical*

Digest Series, volume 5, pages 234–237, Washington, DC, 1994. Optical Society of America.

[7] W. H. Press, S. A. Tenkolsky, W. T. Vetterling, and B. P. Flannery. *"Numerical Recipes in FORTRAN The Art of Scientific Computing"*, pages 402–406. Cambridge University Press, New York, New York, second edition, 1992.

[8] J. O. Hornkohl, C. Parigger, and J. W. L. Lewis. "Temperature measurements from CN spectra in a laser-induced plasma". *J. Quant. Spectrosc. Radiat. Transfer*, 46:405–411, 1991.

[9] C. Parigger, D. H. Plemmons, J. O. Hornkohl, and J. W. L. Lewis. "Spectroscopic temperature measurements in a decaying laser-induced plasma using the C_2 Swan system". *J. Quant. Spectrosc. Radiat. Transfer*, 52:707–711, 1994.

[10] C. Parigger, D. H. Plemmons, J. O. Hornkohl, and J. W. L. Lewis. "Temperature measurements using first-negative N_2^+ spectra produced by laser-induced multiphoton ionization and optical breakdown of nitrogen". *Appl. Opt.*, 34:3331–3335, 1995.

[11] A. P. Thorne. *Spectrophysics*. Chapman and Hall, New York, New York, second edition, 1988. Table 11.1.

[12] F. Roux, F. Michaud, and M. Vervloet. "High-resolution Fourier spectrometry of $^{14}N_2$: analysis of the (0-0), (0-1), (0-2), and (0-3) bands of the $C^3\Pi_u$ - $B^3\Pi_g$ system". *Can. J. Phys.*, 67:143–147, 1989.

[13] K. J. Rensberger, J. B. Jefferies, R. A. Copeland, K. Kohse-Houinghaus, M. L. Wise, and D. R. Crosley. "Laser-induced fluorescence determination of temperatures in low pressure flames". *Appl. Opt.*, 28:3556–3566, 1989.

[14] C. R. Brazier, R. S. Ram, and P. F. Bernath. "Fourier transform spectroscopy of the $A^3\Pi$ - $X^3\Sigma^-$ transition of NH". *J. Molec. Spectrosc.*, 120:381–402, 1986.

[15] F. Roux, F. Michaud, and M. Vervloet. "High-resolution Fourier spectrometry of $^{14}N_2$ violet emission: extensive analysis of the $C^3\Pi_u$ - $B^3\Pi_g$ system". *J. Molec. Spectrosc.*, 158:270–277, 1993.

[16] S. Gordan and B. McBride. "Computer program for calculation of complex equilibrium compositions, rocket performance, incident and reflected shocks, and Chapman-Jouguet detonations". Interim Revision NASA Report SP-273, NASA Lewis Research Center, 1976.

[17] C. Parigger, J. W. L. Lewis, D. H. Plemmons, and J. O. Hornkohl. "Nitric oxide optical breakdown spectra and analysis by the use of the program NEQAIR". Submitted to Optical Society of America for presentation in the 1995 conference on Laser Applications to Chemical and Environmental Analysis, March 1996.

[18] C. Parigger, J. W. L. Lewis, D. H. Plemmons, and J. O. Hornkohl. "Hydroxyl measurements in air-breakdown microplasmas". Submitted to Optical Society of America for presentation in the 1995 conference on Laser Applications to Chemical and Environmental Analysis, March 1996.

[19] S. Yalçin, D. R. Crosley, G. P. Smith, and G. W. Faris. "Spectroscopically determined temperatures and electron densities in laser produced sparks". In *1995 OSA Annual Meeting/ILS-XI Program*, page 147, Portland, Oregon, September 1995. Optical Society of America and Laser Science Topical Group/APS.

[20] P. D. Maker, R. W. Terhune, and C. M. Savage. "Optical Third Harmonic Generation". In *III Int. Conf. on Quant. Electronics*, Paris, 1963.

[21] J. H. Lee and R. Knystautas. "Laser spark ignition of chemically reactive gases". *AIAA Journal*, 7:312–317, 1969.

[22] F. J. Weinberg and J. R. Wilson. "A preliminary investigation of the use of focused laser beams for minimum ignition energy studies". *Proc. Roy. Soc. Lond. A*, 321:41–52, 1971.

[23] N. M. Witriol, B. E. Forch, and A. W. Miziolek. "Modeling laser-ignition of combustible gases". *CPIA Pulbication 557, Volume III*, pages 213–217, 1990.

[24] P. D. Ronney. "Laser versus conventional ignition of flames". *Optical Engineering*, 33:510–521, 1994.

[25] B. Lewis and G. von Elbe. *Combustion, Flames and Explosions of Gases.* Academic Press, Inc., Orlando, Florida, third edition, 1987.

[26] C. Parigger, J. W. L. Lewis, and D. H. Plemmons. "Electron number density and temperature measurement in a laser-induced hydrogen plasma". *J. Quant. Spectros. Radiat. Trans.*, 53:249–255, 1995.

[27] C. Parigger, D. H. Plemmons, and J. W. L. Lewis. "Spatially and temporally resolved electron number density measurements in a decaying laser-induced hydrogen plasma using hydrogen-alpha profiles". *Appl. Opt.*, 34:3325–3330, 1995.

[28] See, for example Ref. [25].

[29] F. J. Verkamp, M. C. Hardin, and J. R. Williams. "Ammonia combustion properties and performance in gas-turbine burners". In *Eleventh Symposium (International) on Combustion*, Pitsburgh, Pennsylvania, 1967. The Combustion Institute.

[30] W. L. Buckley and H. W. Husa. "Combustion properties of ammonia". *Chem. Eng. Prog.*, 58:81–84, 1962.

[31] D. Giulietti, A. Giulietti, M. Lucchesi, and M. Vaselli. "Intense diffraction of a laser beam due to self-focusing in underdense plasma". *J. Appl. Phys.*, 58:2916–2921, 1985.

[32] J. A. Syage, E. W. Fournier, R. Rianda, and R. B. Cohen. "Dynamics of flame propagation using laser-induced spark initiation: ignition energy measurements". *J. Appl. Phys.*, 64:1499–1507, 1988.

[33] T. A. Spiglanin, A. McIlroy, E. W. Fournier, R. B. Cohen, and J. A. Syage. "Time-resolved imaging of flame kernels: laser spark ignition of $H_2/O_2/Ar$ mixtures". *Combust. Flame*, 102:310–328, 1995.

[34] B. E. Forch and A. W. Miziolek. "Laser-based ignition of H_2/O_2 and D_2/O_2 premixed gases through resonant multiphoton excitation of H and D atoms near 243 nm". *Combust. Flame*, 85:254–262, 1991.

[35] R. A. Hill. "Ignition-delay times in laser initiated combustion". *Appl Opt.*, 20:2239–2242, 1981.

[36] R. W. Schmieder. "Laser spark ignition and extinction of a methane-air diffusion flame". *J. Appl. Phys.*, 52:3000–3003, 1981.

[37] R. Hickling and W. R. Smith. "Combustion bomb tests of laser ignition". *SAE Paper 740114*, 1974.

[38] L-K. Tseng, M. A. Ismail, and G. M. Faeth. "Laminar burning velocities and Markstien numbers of hydrocarbon/air flames". *Combust. Flame*, 95:410–426, 1993.

[39] R. A. Strehlow. "The concept of flame stretch". *Combust. Flame*, 31:209–211, 1978.

[40] V. Ya. Basevich and V. I. Vedeneev. "Propagation of a laminar ammonia flame". *Combust. Explos. Shock Waves*, 27:559–564, 1991.

[41] J. M. Seitzman, P. H. Paul, and R. K. Hanson. "Digital Imaging of Laser-Ignited Combustion". In *AIAA Thermophysics, Plasmadynamics and Lasers Conference*, volume AIAA-88-2775, San Antonio, Texas, June 27-29 1988.

[42] R. J. H. Klein-Douwel, J. J. L. Spaanjaars, and J. J. ter Meulen. "Two-dimensional distributions of C_2, CH, and OH in a diamond depositing oxyacetylene flame measured by laser induced fluorescence". *J. Appl. Phys.*, 78:2086–2096, 1995.

[43] M. Versluis, M. Boogaarts, R. Klein-Douwel, B. Thus, W. de Jongh, A. Braam, J. J. ter Meulen, W. L. Meerts, and G. Meier. "Laser-induced fluorescence imaging in a 100 kW natural gas flame". *Appl. Phys. B*, 55:164–170, 1992.

[44] A. D. Sappey, D. R. Crosley, and R. A. Copeland. "Laser-induced fluorescence detection of singlet CH_2 in low-pressure methane/oxygen flames". *Appl. Phys. B*, 50:463–472, 1990.

[45] M. Aldèn, H. Edner, G. Holmstedt, S. Svanberg, and T. Hoeberg. "Single-pulse laser-induced OH fluorescence in an atmospheric flame, spatially resolved with a diode array". *Appl. Opt.*, 21:1236–1240, 1982.

[46] M. J. Dyer and D. R. Crosley. "Two-dimensional imaging of OH laser-induced fluorescence in a flame". *Opt. Lett.*, 7:382–384, 1982.

[47] J. B. Kelnam and A. R. Masri. "Quantitative imaging of temperature and OH in turbulent diffusion flames by using a single laser source". *Appl. Opt.*, 33:3992–3999, 1994.

[48] A. Hirano and M. Tsujishita. "Visualization of CN by the use of planar laser-induced fluorescence in a cross section of an unseeded turbulent CH_4-air flame". *Appl. Opt.*, 33:7777–7780, 1994.

[49] R. W. Dibble, M. B. Long, and A. Masri. "Two-dimensional imaging of C_2 in turbulent nonpremixed jet flames". In *Tenth International Colloquium of Dynamics of Explosions and Reactive Systems*, pages 99–109, Berkeley, California, Aug. 4-9 1985.

[50] T. Berglind and J. Sunner. "The temporal development of OH concentration profiles in ignition kernels studied by single-pulse laser-induced fluorescence". *Combust. Flame*, 63:279–288, 1986.

[51] U. Brackmann. *"Lambdachrome Laser Dyes"*. Lambda Physik GmbH, Goettingen, Germany, second revised edition, 1994.

[52] M. Kono, K. Niu, T. Tsukamoto, and Y. Ujiie. "Mechanism of flame kernel formation produced by short duration sparks". In *Twenty-Second Symposium (International) on Combustion*, pages 1643–1649, Pittsburgh, 1988. The Combustion Institute.

[53] R. Maly. "Ignition model for spark discharges and the early phase of flame growth". In *Eighteenth Symposium (International) on Combustion*, pages 821–831, Pittsburgh, 1981. The Combustion Institute.

[54] A. Borghese, A. D'Alessio, M. Diana, and C. Venitozzi. "Development of hot nitrogen kernel, produced by a very fast spark discharge". In *Twenty-Second Symposium (International) on Combustion*, pages 1651–1659, Pittsburgh, 1988. The Combustion Institute.

[55] R. Maly and M. Vogel. "Initiation and propagation of flame fronts in lean CH_4-air mixtures by the three modes of the ignition spark". In *Seventeenth Symposium (International) on Combustion*, pages 821–831, Pittsburgh, 1978. The Combustion Institute.

[56] T. M. Sloane and J. W. Ratcliff. "Chemistry of Spark Ignition - An Experimental and Computational Study". In *"Chemistry of Combustion Processes"*, pages 205–222. American Chemical Society, New York, New York, 1984.

[57] S. A. Ramsden and W. E. R. Davies. "Radiation scattered from the plasma produced by a focused ruby laser beam". *Phys. Rev. Lett.*, 13:227–229, 1964.

[58] C. DeMichelis. "Laser induced gas breakdown: a bibliographical review". *J. Quantum Electron.*, QE-5:188–202, 1969.

[59] T. Kravchik and E. Sher. "Numerical modeling of spark ignition and flame initiation in a quiescent methane-air mixture". *Combust. Flame*, 99:635–643, 1994.

[60] J. W. Goodman. *Introduction to Fourier Optics.* McGraw-Hill, San Francisco, California, 1968.

[61] L. M. Smith. *"A unified study of the effects of aberrations in focused laser beams".* PhD thesis, The University of Tennessee Space Institute, 1988.

[62] C. Parigger, J. W. L. Lewis, G. G. Guan, and R. Gurney. Unpublished report.

[63] M. Born and E. Wolf. *Principles of Optics.* Pergamon Press, Oxford, England, 1980.

Appendices

Appendix A

Calculation of the Focal Volume of Monochromatic, Coherent Radiation – with Aberrations

The three dimensional intensity distribution of a focused laser beam near the focal point of a converging lens can be calculated from the Rayleigh-Sommerfeld diffraction integral [60]. A good treatment of this problem, which uses a Fourier optics approach, is given in the doctoral dissertation of L. M. Smith [61]. In this Appendix, a method is presented in which the diffraction integral is numerically evaluated - thereby bypassing the polynomial expansion treatment of spherical aberrations. This evaluation was adapted from a computer code developed by C. Parigger *et al.* for calculation of lens axicon doublets [62].

Consider a lens centered on the optical axis with its front surface located at $z = z_1$ and its rear surface at $z = \Delta_0$, where Δ_0 is the maximum thickness of the lens, as shown in Fig. A.1. The complex field amplitude in the x_f-y_f plane located at a distance z_f from the front surface of the lens is

$$U(x_f, y_f, z_f) = \frac{i}{\lambda} \int_{-\infty}^{\infty} \int_{-\infty}^{\infty} dx dy U(x_1, y_1, z_1) \frac{e^{-ikr_{f1}}}{r_{f1}} cos(\vec{n}, \vec{r}_{f1}). \tag{A.1}$$

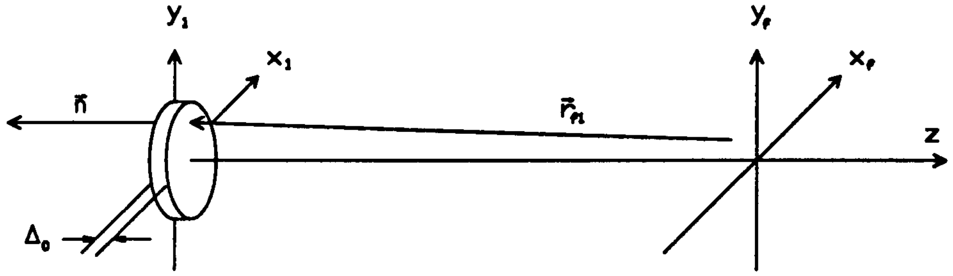

Figure A.1: Coordinate system for lens focus calculation.

Let $U(x, y, 0)$ denote the complex field amplitude incident on the lens. The transmitted field $U(x, y, \Delta_0)$ at the back of the lens is

$$U(x, y, \Delta_0) = U(x, y, 0)P(x, y)e^{-ik\Delta_0}e^{-ik(n-1)\Delta(x,y)}, \tag{A.2}$$

where the slowly varying envelope approximation has been applied as the field traverses the lens. In Eq. A.2, $P(x, y)$ is the pupil function describing the lens aperture and $\Delta(x, y)$ is the thickness of the lens at the location (x, y).

For a spherical surface lens with a front surface radius R_1 and a rear surface radius R_2

$$\begin{aligned} \Delta(x,y) &= \Delta_0 - R_1\left(1 - \sqrt{1 - \frac{x^2+y^2}{R_1^2}}\right) + R_2\left(1 - \sqrt{1 - \frac{x^2+y^2}{R_2^2}}\right) \\ &= \Delta_0 - \bar{R}_1 + \bar{R}_2 \end{aligned}$$

The distance r_{f1} is

$$r_{f1} = \sqrt{(x_f - x)^2 + (y_f - y)^2 + (z_f - \Delta_0)^2}$$

$$= \sqrt{(x_f - x)^2 + (y_f - y)^2 + (z_p)^2}$$

The obliquity factor $cos(\vec{n}, \vec{r}_{f1})$ is

$$cos(\vec{n}, \vec{r}_{f1}) = \frac{z_p}{r_{f1}}$$

$$= \frac{|z_f - \Delta_0|}{\sqrt{(x_f - x)^2 + (y_f - y)^2 + (z_f - \Delta_0)^2}}$$

which is approximately equal to 1 in the far field (for large f/#'s).

From Eq. A.1

$$U(x_f, y_f, z_f) = \frac{i}{\lambda} \int_{-\infty}^{\infty} \int_{-\infty}^{\infty} dxdy e^{ikn\Delta_0} U(x, y, 0) P(x, y) e^{ik(n-1)(-\bar{R}_1 + \bar{R}_2)} \frac{e^{-ikr_{f1}}}{r_{f1}} cos(\vec{n}, \vec{r}_{f1}) \tag{A.3}$$

Approximating $r_{f1} \simeq z_p$ in the denominator and expanding r_{f1} in a Taylor series in the exponential yields

$$\frac{e^{-ikr_{f1}}}{r_{f1}} \simeq \frac{1}{z_p} exp\left\{-ik\left(z_p + \frac{x_f^2 + y_f^2}{2z_p} + \frac{x^2 + y^2}{2z_p} - \frac{xx_f + yy_f}{z_p}\right)\right\}$$

Using these approximations in Eq. A.3 yields

$$U(x_f, y_f, z_f) \simeq \frac{ike^{-ikn\Delta_0}}{2\pi} \int_{-\infty}^{\infty} \int_{-\infty}^{\infty} dxdy P(x, y) U(x, y, 0) cos(\vec{n}, \vec{r}_{f1}) \times$$

$$exp\left\{-ik\left(z_p + \frac{x_f^2 + y_f^2}{2z_p} + \frac{x^2 + y^2}{2z_p} - \frac{xx_f + yy_f}{z_p}\right)\right\} exp\left\{-ik(n-1)(\bar{R}_1 - \bar{R}_2\right\}$$

$$= \frac{ike^{ikn\Delta_0}}{2\pi} exp\left\{ik(z_p + \frac{x_f^2 + y_f^2}{2z_p}\right\} \times \int_{-\infty}^{\infty} \int_{-\infty}^{\infty} dxdy P(x, y) U(x, y, 0) cos(\vec{n}, \vec{r}_{f1})$$

$$exp\left\{-ik\left(\frac{x^2+y^2}{2z_p}-\frac{xx_f+yy_f}{z_p}\right)\right\}\times exp\left\{-ik(n-1)(\bar{R}_1-\bar{R}_2)\right\}. \qquad \text{(A.4)}$$

For cylindrically symmetric input beams the treatment of Born and Wolf [63] can be invoked to reduce this two dimensional integral to a one dimensional integral over the radius of a circular lens aperture. Since the interest here is experimentally determined laser pulse spatial profiles which do not necessarily exhibit such symmetry and which are measured with a square or rectangular two dimensional detector array, this equation is left in its present form and is specialized for the problem at hand.

The lens used to focus the Infinity pulses was a 100 mm focal length, plano-convex lens with the convex surface facing the laser. Therefore, in Eq. A.4, $R_2 = \infty$ and $\bar{R}_2 = 0$. The measured input beam was of the dimensions $a \times a$ which means that the pupil function is a two dimensional step function, which is formally expressed by

$$\int_{-\infty}^{\infty}\int_{-\infty}^{\infty} dxdyP(x,y) \rightarrow \int_{-a/2}^{a/2}\int_{-a/2}^{a/2} dxdy$$

where a = 5.875 mm. For the f/# of approximately 17, $cos(\vec{n},\vec{r}_{f1}) \simeq 1$. Since the interest here is only the intensity distribution at the focal plane ($I = U^*U$), the complex exponentials outside the integral in Eq. A.4 can be ignored. Therefore,

$$U(x_f,y_f,z_f) \sim \frac{k}{2\pi}\int_{-a/2}^{a/2}\int_{-a/2}^{a/2} dxdyU(x,y,0)\times$$

$$exp\left\{-ik\left(\frac{x^2+y^2}{2z_f}-\frac{xx_f+yy_f}{z_f}+(n-1)\bar{R}_1\right)\right\}$$

where U(x,y,0) is the measured input pulse.

This integral was evaluated using the IMSL subroutine QDAG on a Pentium 100 MHz PC. It typically took one second to calculate one point in the focal plane.

Appendix B

Ammonia-Oxygen Reaction Mechanism

The following reaction mechanism was taken from the compilation found in Reference [40]. The coefficient are for an Arrhenius equation of the form

$$k = Ae^{-E/RT}$$

where E is the activation energy and A is the temperature dependant frequency factor. The constants tabulated below are for forward reactions only and are used as input in the CHEMKIN laminar flame computer code [4].

Reaction	A (m^3/mol sec)	E (cal/mole)
$OH + H_2 \rightarrow H_2O + H$	$2.16\times10^{8}T^{1.51}$	3430.
$H + O_2 \rightarrow OH + O$	$5.13\times10^{16}T^{-0.816}$	16,500.
$O + H_2 \rightarrow OH + H$	1.5×10^{13}	8900.
$OH + OH \rightarrow O + H_2O$	$6.0\times10^{8}T^{1.27}$	0.
$H_2 + M \rightarrow H + H + M$	$1.05\times10^{20}T^{-1.31}$	105,000.
$O_2 + M \rightarrow O + O + M$	$1.55\times10^{20}T^{-1.64}$	120,000.
$H + OH + M \rightarrow H_2O + M$	3.6×10^{16}	0.
$O + H + M \rightarrow OH + M$	4.7×10^{15}	0.
$H + HO_2 \rightarrow H_2 + O_2$	6.0×10^{12}	0.
$H + O_2 + M \rightarrow HO_2 + M$	4.14×10^{15}	0.
$H + HO_2 \rightarrow OH + OH$	2.0×10^{13}	0.
$O + HO_2 \rightarrow O_2 + OH$	6.0×10^{13}	0.
$OH + HO_2 \rightarrow H_2O + O_2$	6.0×10^{12}	0.
$H + HO_2 \rightarrow H_2O + O$	6.0×10^{11}	0.
$H_2O_2 + OH \rightarrow H_2O + HO_2$	1.75×10^{12}	320.
$H_2O_2 + H \rightarrow H_2O + OH$	7.05×10^{12}	4200.
$H_2O_2 + M \rightarrow OH + OH + M$	4.07×10^{16}	42,000.
$O + H_2O_2 \rightarrow O_2 + H_2O$	2.8×10^{13}	6400.
$H + H_2O_2 \rightarrow H_2 + HO_2$	7.0×10^{12}	4200.
$HO_2 + HO_2 \rightarrow H_2O_2 + O_2$	2.3×10^{11}	1160.
$O + H_2O_2 \rightarrow HO_2 + OH$	2.8×10^{13}	6400.
$NH_2 + H + M \rightarrow NH_3 + M$	3.2×10^{11}	-15,000.
$NH_2 + HO_2 \rightarrow NH_3 + O_2$	2.5×10^{11}	-1400.
$NH_2 + OH \rightarrow NH_3 + O$	1.26×10^{11}	2900.
$NH_2 + O \rightarrow HNO + H$	6.0×10^{11}	0.
$NH_2 + NO \rightarrow N_2 + H_2O$	$1.25\times10^{21}T^{-3.2}$	0.
$NH_2 + NH_2 \rightarrow NH_3 + NH$	6.0×10^{13}	10,000.
$NH_2 + NH \rightarrow NH_3 + N$	6.0×10^{13}	4000.
$NH_3 + OH \rightarrow NH_2 + H_2O$	3.2×10^{12}	1840.
$NH_3 + H \rightarrow NH_2 + H_2$	3.6×10^{12}	9000.
$HNO + OH \rightarrow NO + H_2O$	6.0×10^{11}	0.
$NH + NO \rightarrow N_2 + OH$	1.0×10^{12}	0.
$HNO + O \rightarrow NO + OH$	6.0×10^{12}	0.
$NH + O_2 \rightarrow NO + OH$	5.1×10^{9}	0.
$NH + OH \rightarrow NO + H_2$	$1.6\times10^{11}T^{0.56}$	1500.
$NH + H \rightarrow N + H_2$	1.2×10^{13}	4200.
$NH + O \rightarrow N + OH$	6.0×10^{13}	5000.
$HNO + H \rightarrow NO + H_2$	6.0×10^{13}	0.
$NH + NH \rightarrow NH_2 + N$	6.0×10^{13}	8000.
$NO + HO_2 \rightarrow NO_2 + OH$	8.7×10^{11}	0.

Reaction	A (mole m^3 sec)	E (cal/mole)
$NO_2 + H \rightarrow NO + OH$	2.9×10^{13}	0.
$NO + O + M \rightarrow NO_2 + M$	$5.8\times10^{10}T^{1.0}$	-8600.
$NO_2 + O \rightarrow NO + O_2$	1.0×10^{13}	600.
$NO + NO + O_2 \rightarrow NO_2 + NO_2$	$4.9\times10^{6}T^{1.0}$	-600.
$NO_2 + O + M \rightarrow NO_3 + M$	$2.8\times10^{13}T^{1.0}$	-7800.
$NO + O_2 + M \rightarrow NO_3 + M$	$7.65\times10^{6}T^{1.0}$	-1700.
$N + NO \rightarrow N_2 + O$	2.75×10^{12}	500.
$N + O_2 \rightarrow NO + O$	1.0×10^{13}	7500.
$NO + NO \rightarrow N_2 + O_2$	1.35×10^{14}	75,600.
$N + OH \rightarrow NO + H$	$1.33\times10^{14}T^{-0.25}$	0.
$O + NH \rightarrow H + NO$	6.0×10^{12}	0.
$NH_2 + NO \rightarrow N_2 + OH + H$	$6.2\times10^{18}T^{-2.2}$	1000.
$H + NH_2 \rightarrow NH + H_2$	6.0×10^{12}	8100.
$NH + NH_3 \rightarrow N_2H_4$	6.0×10^{12}	0.
$NH_2 + N \rightarrow N_2 + H_2$	6.0×10^{12}	0.
$NH_2 + O_2 \rightarrow HNO + OH$	1.6×10^{13}	28,400.
$HO_2 + NO \rightarrow O_2 + HNO$	4.5×10^{11}	0.
$H + NO + M \rightarrow HNO + M$	$3.0\times10^{12}T^{1.0}$	0.
$N + N_2H_3 \rightarrow H + NH_2 + N_2$	6.0×10^{12}	0.
$N + H_2 \rightarrow NH_2$	1.33×10^{13}	11,100.
$N + NH_3 \rightarrow N_2H_3$	4.85×10^{13}	9600.

Vita

David Plemmons was born in Memphis Tennessee on April 26, 1962. He was raised in rural west Tennessee. He graduated from high school in 1980 and spent two years studying engineering at The University of Tennessee at Martin. He moved to middle Tennessee in 1984 and enrolled in Middle Tennessee State University (MTSU). He graduated from MTSU with a B.S. in Aerospace Maintenance Management in 1996. In 1997 he acquired his Airframe and Powerplant certificate from the Federal Aviation Administration. From 1985 to 1988 he worked as an aircraft technician. In 1988 he enrolled in graduate school at The University of Tennessee Space Institute (UTSI) and quickly discovered that his was academically unprepared for a career in scientific research. He withdrew from UTSI after one semester and re-enrolled in MTSU, were he studied undergraduate physics and mathematics. He graduated with a double major in 1990 and re-enrolled at UTSI — deciding to pursue a graduate degree in physics. He earned an M.S. in physics in 1994 and his Ph.D. in physics in 1996.